Czech Technical University in Prague
Faculty of Nuclear Sciences and Physical Engineering
Department of Physics

Field: Experimental Nuclear and Particle Physics

Impact of invisible energy on the energy reconstruction of cosmic-ray shower using fluorescence telescopes at the Pierre Auger Observatory

MASTER'S THESIS

Author: Bc. Šimon Novák
Supervisor: RNDr. Petr Trávníček, Ph.D.
Year: 2018

České Vysoké Učení Technické v Praze

Fakulta Jaderná a Fyzikálně Inženýrská

Katedra Fyziky

Obor: Experimentální jaderná a částicová fyzika

Vliv chybějící energie při rekonstrukci energie spršky kosmického záření z dat fluorescenčních teleskopů na Observatoři Pierra Augera

DIPLOMOVÁ PRÁCE

Autor:	Bc. Šimon Novák
Školitel:	RNDr. Petr Trávníček, Ph.D.
Rok:	2018

Prohlášení

Prohlašuji, že jsem svou diplomovou práci vypracoval samostatně a použil jsem pouze podklady (literaturu, projekty, SW atd.) uvedené v přiloženém seznamu.

Nemám závažný důvod proti použití tohoto školního díla ve smyslu § 60 Zákona č. 121/2000 Sb., o právu autorském, o právech souvisejících s právem autorským a o změně některých zákonů (autorský zákon).

V Praze dne 7.5.2018

Bc. Šimon Novák

Acknowledgements

First and foremost, I want to express my gratitude to my supervisor RNDr. Petr Trávníček, Ph.D., for his patient guidance and revision of my master's thesis. I then want to thank Ing. Jakub Vícha, Ph.D., for his important suggestions and assistance throughout my work and also thank the whole Pierre Auger Group at the Institute of Physics of the Czech Academy of Sciences for the chance to participate in the puzzling cosmic-ray challenges.

Second, my thanks goes to my family, especially to my parents, for their continuous support of my studies.

Last but not least, a warmful thanks belongs to my long-time partner Jessica, who is my support throughout the whole time of my studies in Prague.

Název práce:

Vliv chybějící energie při rekonstrukci energie spršky kosmického záření z dat fluorescenčních teleskopů na Observatoři Pierra Augera

Autor: Bc. Šimon Novák

Obor: Experimentální jaderná a částicová fyzika

Druh práce: Diplomová práce

Vedoucí práce: RNDr. Petr Trávníček, Ph.D.
Fyzikální ústav AV ČR, v.v.i.

Konzultant: Ing. Jakub Vícha, Ph.D.
Fyzikální ústav AV ČR, v.v.i.

Abstrakt: Rozsáhlé spršky kosmického záření vzniklé interakcí vysoce energetických částic se zemskou atmosférou při energiích přesahujících 400 TeV v těžišťové soustavě jsou pozorovány na Observatoři Pierra Augera - největším světovém experimentu pro detekci kosmického záření. Pro určení parametrů kosmického záření je třeba přesně změřit energii spršky, a proto musí být kalorimetrická energie spršky opravena o hodnotu chybějící energie - části energie spršky, která je nesena miony a neutriny a není detekována fluorescenčními detektory. Pro určení této chybějící energie je navrhnuto několik metod za pomoci simulačních programů CONEX a CORSIKA při užití nejnovějších hadronických interakčních modelů EPOS LHC a QGSJET-II-04. Představené metody jsou posléze porovnány mezi sebou jak na simulovaných, tak na reálných datech získaných na Observatoři Pierra Augera.

Klíčová slova: Observatoř Pierra Augera, ultra-energetické kosmické záření, spršky kosmického záření, chybějící energie

Title:

Impact of invisible energy on the energy reconstruction of cosmic-ray shower using fluorescence telescopes at the Pierre Auger Observatory

Author: Bc. Šimon Novák

Abstract: Extensive Air Showers created by interactions of Ultra-High Energy Cosmic Ray particles with the Earth's atmosphere at center of mass energy exceeding 400 TeV are being detected at the Pierre Auger Observatory - the world's biggest experimental site for observation of cosmic rays. For determination of cosmic ray properties a precise measurement of shower energy is required, therefore the shower calorimetric energy measured by the fluorescence detectors at the observatory must be corrected to the invisible energy part - the part of the shower energy is carried away by muons and neutrinos undetected. Several methods of the invisible energy estimation are proposed using shower simulation codes CONEX and CORSIKA with the two newest hadronic interaction models EPOS LHC and QGSJET-II-04 being used. The proposed methods are compared on simulated and real cosmic-ray data measured at the PAO.

Key Words: Pierre Auger Observatory, Ultra High-Energy Cosmic Rays, Extensive Air Showers, Shower Invisible Energy

Contents

Introduction **10**

1 Cosmic rays and Cosmic-ray air showers **12**
- 1.1 Primary cosmic-ray spectrum . . . 12
- 1.2 Primary cosmic-ray sources . . . 14
- 1.3 Propagation of cosmic rays . . . 14
- 1.4 Air shower composition . . . 16
- 1.5 Air Shower models . . . 18
  - 1.5.1 Heitler model . . . 18
  - 1.5.2 Heitler-Matthews model . . . 19
  - 1.5.3 Superposition model . . . 21
  - 1.5.4 Monte Carlo simulations . . . 21

2 The Pierre Auger Observatory **22**
- 2.1 Surface detector . . . 23
- 2.2 Fluorescence detector . . . 24
- 2.3 Shower reconstruction . . . 25
  - 2.3.1 FD reconstruction . . . 26
  - 2.3.2 SD reconstruction . . . 27
- 2.4 Selected results of the Pierre Auger Observatory . . . 30
  - 2.4.1 Energy spectrum . . . 30
  - 2.4.2 Mass composition . . . 31
  - 2.4.3 Arrival directions and anisotropy . . . 32

3 Invisible energy in cosmic-ray showers **34**
- 3.1 Invisible energy estimation using CONEX . . . 34
  - 3.1.1 C_{miss} parametrization . . . 37
  - 3.1.2 Muon number parametrization . . . 38
- 3.2 Invisible energy estimation using CORSIKA . . . 41
  - 3.2.1 $S(1000)$ parametrization using zenith angle . . . 42
  - 3.2.2 $S(1000)$ parametrization using DX . . . 44
  - 3.2.3 $S_{\mu}(1000)$ parametrization . . . 46
- 3.3 Application to simulated data . . . 47

4 Application to real cosmic-ray data **54**
- 4.1 Invisible energy parametrization using E_{cal} . . . 54
  - 4.1.1 Comparison of average invisible energy parametrizations . . . 56

4.2 FD and SD reconstructed energy comparison 57

Summary **59**

Appendix **61**

Bibliography **72**

Introduction

The enigmatic properties of Ultra-High Energy Cosmic Rays (UHECR) with energies exceeding 10^{18} eV such as their primary composition, arrival directions and exact processes through which they originate are still unclear. At these energies, observed cosmic-ray particle flux is so small that a direct detection using a normal size satellite at the top of Earth's atmosphere would be statistically insufficient. Nevertheless, primary cosmic-ray particles are interacting with nuclei of atmospheric gases and thus creating many energetic hadrons and leptons which further interact with atmosphere. More than 10^{10} secondary cosmic-ray particles creating a cosmic-ray air shower with diameter reaching $\sim$10 km can emerge through series of hadronic and electromagnetic multiplication cascades. These Extensive Air Showers (EAS) are being thoroughly studied for many years since their discovery by physicists Pierre Auger and Walther Bothe in 1930s.

Measured EAS parameters such as an energy deposition into the atmosphere or a depth of shower maximum can provide insight into the primary particle composition and its energy. Also a reconstructed arrival direction of the most energetic air shower events can pinpoint possible UHECR sources in the sky. These EAS studies are also considered to confront the predictions of hadronic interaction models of particle collisions at the energies several times exceeding the highest ones achievable at man-made particle accelerators. For illustration, the maximum possible center-of-mass energy of two colliding protons at the LHC is 14 TeV in comparison to center-of-mass energy of $\sim$450 TeV in proton-proton interaction of a 10^{20} eV proton primary particle hitting an atmospheric gas nucleus.

Several experiments for EAS detection are in operation in both hemispheres. Some of the most important are the Telescope Array in Utah and the largest cosmic ray detector array - the Pierre Auger Observatory (PAO) in Argentina. Hybrid detector approach with cooperation of surface and fluorescence detectors is used in both observatories and enables to collect precise cosmic-ray data. Since the beginning of the PAO data acquisition in 2004, important UHECR properties were established (see Sec. 2.4). Both observatories are also in progress of augmentation and enhancement of measuring devices - The AugerPrime upgrade at the PAO or the TALE extension at the Telescope Array.

The Master's thesis aims to understand the process of shower reconstruction at the PAO, mainly the estimation of shower total energy accounting for the invisible energy - the energy carried away by muons and neutrinos. Several methods of estimating the invisible energy are discussed and used on both Monte Carlo and real cosmic-ray data. The scope of the thesis is to find the connection between the invisible energy and an observable parameter at the PAO reflecting the number of muons hitting the surface detectors. Better energy reconstruction methods will lower systematic errors and can contribute to more educated physical interpretation of measured data.

In the chapter 1, primary and secondary cosmic rays are briefly characterized including a basic characteristics of astrophysical cosmic-ray sources. Important effects during propagation of primary cosmic rays from sources to the Earth are also mentioned. The creation and development of a cosmic-ray air shower in the Earth's atmosphere is described by semi-empirical models and basic shower properties are outlined.

The chapter 2 concerns the hardware setup of the Pierre Auger Observatory, methods of shower detection and reconstruction as well as energy calibration of measured data. Some main scientific results since the start of observatory's operation are highlighted here including the measured cosmic-ray energy spectrum, mass composition and arrival directions.

The main part of the thesis - the invisible energy in cosmic-ray showers - is discussed in the chapter 3. Several methods for estimation of the invisible energy using Monte Carlo simulations are proposed. Two newest hadronic interaction models are used - EPOS LHC and QGSJET-II-04. Possible event-by-event correction using measured shower parameters at the PAO is proposed and applied on simulated data.

In the last chapter 4, the best method from the previous chapter is applied to real cosmic-ray data measured at the PAO and new calibration of the Surface Detector signal is gain. The overall effectiveness is discussed when compared the reconstruction by the Fluorescence Detectors to the Surface Detectors.

Ultimately, the thesis is summarized in the Summary.

Chapter 1

Cosmic rays and Cosmic-ray air showers

The UHECR represent only a tiny fraction of all cosmic-ray particle spectrum arriving to the Earth with the majority being less energetic particles coming from the Sun. Cosmic-ray spectrum is steeply falling with energy, hence a particle with 10^{20} eV is expected to hit a square kilometer only once per century. Only possibility how to effectively study the UHECR is an indirect measurement of secondary cosmic-ray particles over vast area with the Earth's atmosphere acting as a huge calorimeter.

1.1 Primary cosmic-ray spectrum

Measured differential flux J of cosmic-ray particles can be expressed as a function of particle energy in the form

$$J(E) = \frac{\mathrm{d}N}{\mathrm{d}E\,\mathrm{d}S\,\mathrm{d}t\,\mathrm{d}\Omega} \propto E^{-\gamma}, \tag{1.1}$$

where N is number of cosmic ray particles with energy in interval $(E, E+\mathrm{d}E)$ detected per unit area S, time t and solid angle Ω. Parameter $\gamma \equiv \gamma(E)$ is called spectral index and it varies with energy. Its mean value is $\gamma \approx 2.7$.

Combined data from various experiments covering different energy regions shows scaled differential flux of primary cosmic rays in Fig. 1.1. Four main areas with different steepness are distinguishable. They are separated by three transitions in spectral index value - spectral breaks. Because of the plot's resemblance to a human leg, these transitions are called "knee", "ankle" and "toe".

The first spectral break (the "knee") occurs at energy $\sim 4 \times 10^{15}$ eV and spectral index shifts from $\sim$2.6 to $\sim$3.3. This transition can be explained by the fact that the most common sources in our Galaxy are reaching their limits for accelerating protons. It means that Larmor radius

$$R_L[\mathrm{kpc}] = \frac{E[\mathrm{EeV}]}{Z.B[\mu\mathrm{G}]} \tag{1.2}$$

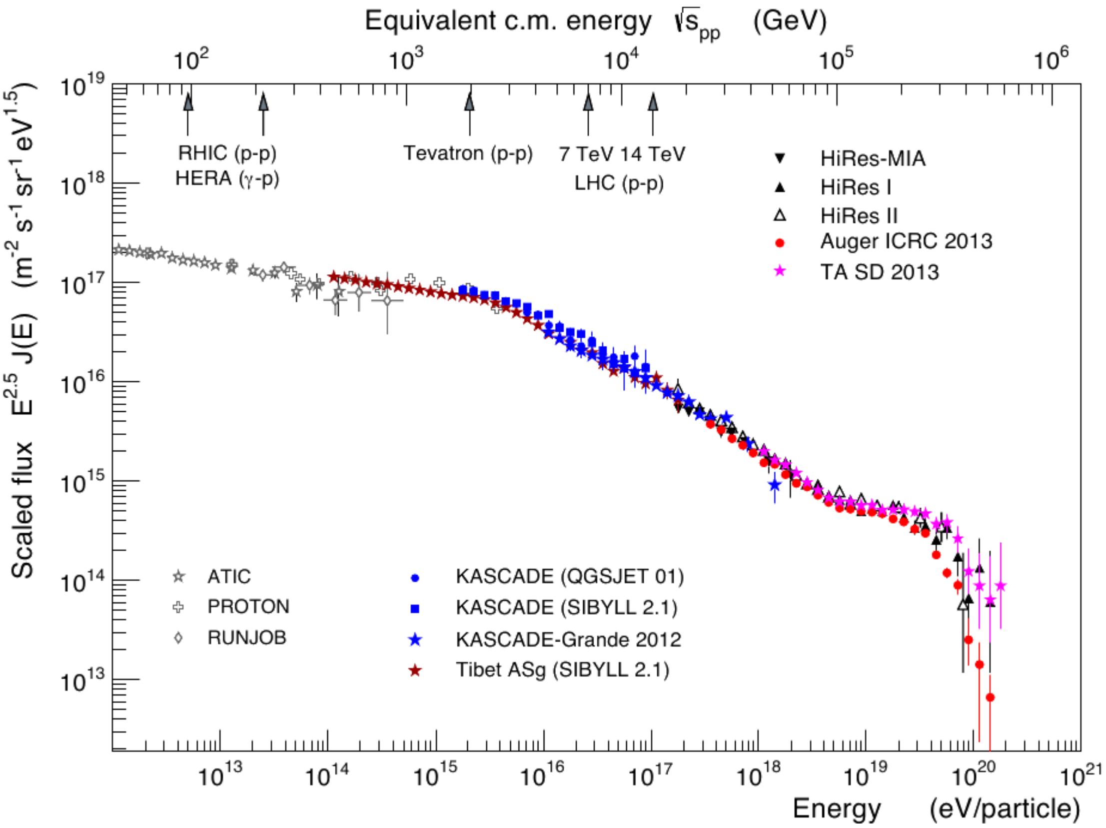

Figure 1.1: Measured differential flux $J(E)$ of cosmic rays as a function of energy scaled by factor $E^{2.5}$. Particle energy is compared with center-of-mass energy limits of man-made particle accelerators. Taken from [29].

reaches the characteristic size of a relevant source type and particles start escaping from the accelerating region. Since iron nuclei have $Z = 26$, the limit of Galaxy accelerators for these nuclei occurs at higher energies around $\sim 8 \times 10^{16}$ eV. This is indeed observable in the cosmic-ray energy spectrum as so called ”second knee”.

At the energy of $\sim 5 \times 10^{18}$ eV another spectral break is observed and γ changes from ~ 3.3 to ~ 2.5. This ”ankle” is often interpreted as transition between galactic and extragalactic sources. For proton with energy $E \approx 10^{18}$ eV and $Z = 1$ traveling in the Galaxy with mean magnetic field $B \approx 3\,\mu$G the Larmor radius (1.2) would reach $R_L \approx 0.3$ kpc which is comparable to the half-thickness of the Galactic disk. Protons then escape into extragalactic space more likely.

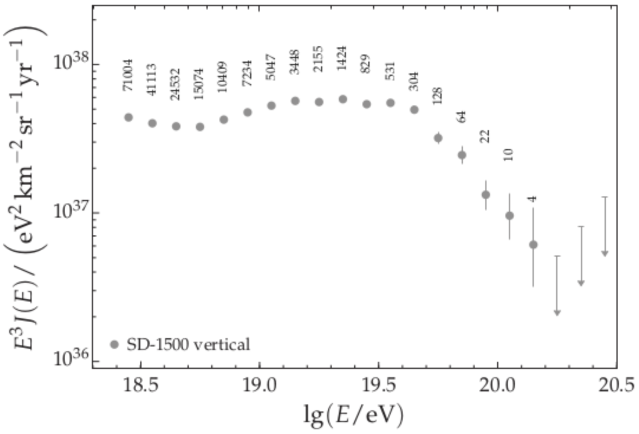

Figure 1.2: Measured differential flux $J(E)$ of cosmic rays at the highest energies at the PAO scaled by factor E^3. Number of events in each energy bin is shown. Taken from [2].

At even higher energies over $\sim 4 \times 10^{19}$ eV the spectrum begins to fall drastically with $\gamma \approx 4$ and higher. This "toe" could be understood as an overall limit for extragalactic sources for proton acceleration. However, other processes during UHECR propagation from its source can substantially lower the observed flux above the "toe" energy such as the GZK cut-off described in Sec. 1.3. The UHECR flux in the highest energy region was measured by the PAO (Fig. 1.2) and the existence of "ankle" and "toe" is confirmed without any doubt (see 2.4.1).

1.2 Primary cosmic-ray sources

Various processes exist in the Universe capable of accelerating charged particles. The most probable sources inside our Galaxy are supernova expanding remnants, pulsars and magnetars. Shock waves created by supernova explosions can theoretically produce particles with energies up to 10^{18} eV (for heavy ions) through the process of Fermi acceleration [14]. Magnetars posses magnetic fields reaching enormous values of 10^{11} T. This strong magnetic field can confine charged particles for sufficiently long time for accelerating them before they can escape.

The UHECR at the highest energies are considered to be of extragalactic origin as no sufficiently strong source is observed within our Galaxy. The most probable sources are AGNs - Active Galactic Nuclei - with supermassive black holes in their centers. Accretion disk around a supermassive black hole creates enormous jets of accelerated particles. According to direction in which the jet is observed we distinguish blasars, quasars or radio galaxies. Another possible source is a fusion of galaxies or black holes.

One can illustratively show various objects in the Universe sorted by the ability to confine a particle during an acceleration. The Hillas diagram in Fig.1.3 simply shows the sources according to their magnetic field and size. In order to confine particles at given high energy within a cosmic-ray source, its size must be larger than radius R_L from Eq. (1.2). It can be seen that several objects could theoretically accelerate proton up to 10^{20} eV. For more information about cosmic-ray sources and acceleration mechanism one can look in [17],[28].

1.3 Propagation of cosmic rays

Cosmic rays are strongly affected by magnetic fields - the particles from low energy part of the spectrum are deflected by Sun's and Earth's magnetic fields. The trajectories of UHECR up to the energy ~ 1 EeV for protons and ~ 26 EeV for iron nuclei paths are sufficiently distorted by Galactic magnetic fields through propagation from their sources, therefore their arrival directions appear isotropic. Above these energies the Larmor radius (1.2) is very large and the arrival information is not smeared by magnetic fields so much. The anisotropy of UHECR above 8 EeV was indeed measured at the

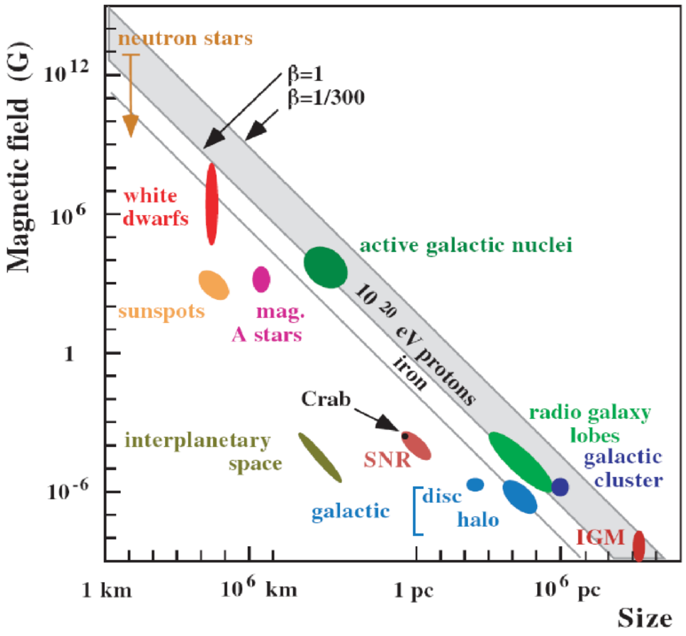

Figure 1.3: Hillas diagram - object's magnetic field strength plotted respectively to its size. Some sources lie on the limit line for accelerating protons to energy 10^{20} eV. β represents the relativistic factor of accelerating shock waves. Taken from [20].

PAO [8] and it indicates extragalactic origin of the most energetic cosmic rays.

The UHECR of sufficiently high energies can also interact with other particles during their propagation. Average matter density in the extragalactic space is low (1 proton per m^3) but the Cosmic Microwave Background (CMB) is sufficiently dense ($\varrho \approx 400\ \mathrm{cm}^{-3}$) to represent a substantial obstruction for the UHECR propagation. The possibility of UHECR to undergo a pion production via interactions with CMB was independently proposed by K. Greisen [16] and G. Zatsepin with V. Kuzmin [31]. The process goes via Δ^+(1232 MeV) resonance with two possible results

$$\gamma + p \rightarrow \Delta^+ \rightarrow p + \pi^0 \tag{1.3a}$$

$$\rightarrow n + \pi^+ . \tag{1.3b}$$

Threshold energy for reactions (1.3a), (1.3b) is $\sim 6 \times 10^{19}$ eV and the proton looses approximatively 15 % of its energy. Reaction is possible even with fotons from IR, UV or visible spectrum with lower threshold energy. Another reaction of cosmic-ray protons with CMB results in creation of electron positron pairs with threshold energy $\sim 5 \times 10^{17}$ eV:

$$\gamma + p \rightarrow p + e^+ + e^- . \tag{1.4}$$

The GZK limit creates an important constraint for distances of UHECR sources from the Earth to maximum of ~100 Mpc. Any UHECR from sources located further away would loose energy during propagation and arrive with energy of the GZK threshold at most. Many candidate UHECR sources are still within this limit e.g. the closest AGN Centaurus A (4 Mpc).

Heavier nuclei with nucleon number A can also interact with CMB through photo-pion and pair production processes with threshold energy roughly A-times larger than threshold energy of respective processes with protons. Nuclei at energies $\sim 3 \times 10^{20}$ eV can also undergo a photodisintegration through Giant Dipole Resonance channel

$$A + \gamma \rightarrow GDR \rightarrow (A-1) + N \tag{1.5a}$$
$$\rightarrow (A-4) + \alpha, \tag{1.5b}$$

where N is a nucleon and α is the alpha particle. This reactions alter energy and mass distributions of cosmic rays during propagation from their sources to the Earth.

1.4 Air shower composition

Primary cosmic ray particle undergoes the first hadronic reaction in upper atmosphere after traversing approximately $25 - 40$ g.cm^{-2} in average[1]. This corresponds to the altitude of $\sim 25 - 35$ km where the atmospheric pressure is $\sim$10 mbar. Many secondary particles are created, still very energetic to cause further reactions with atmospheric molecules and new generations of particles are born.

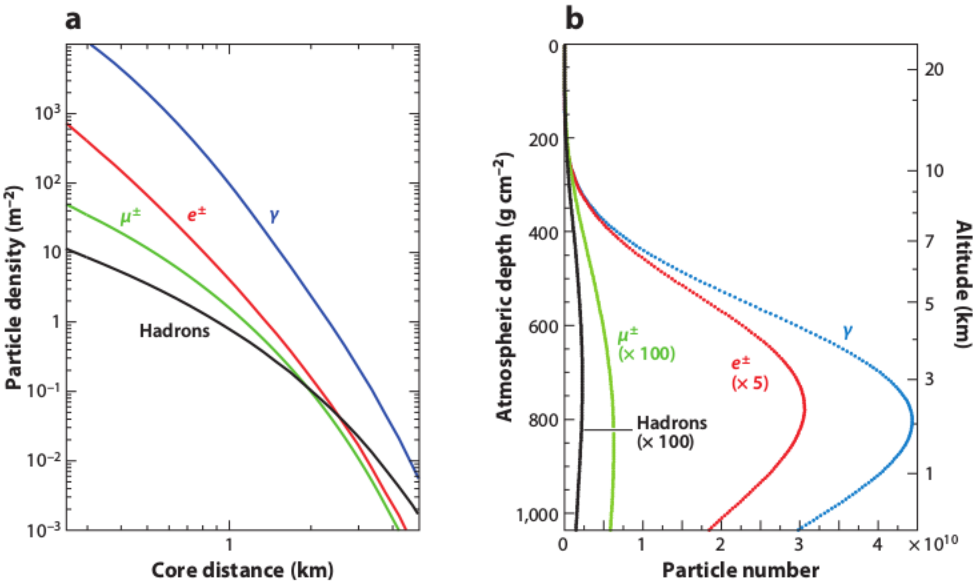

Figure 1.4: Average lateral (a) and longitudinal (b) shower profiles for simulated proton-induced showers with primary energy 10^{19} eV. Lateral profile is taken at depth 880 g.cm^{-2} which corresponds to the ground level at the PAO. Only γ and $e^{\pm}$ above 0.25 MeV, muons and hadrons above 0.1 GeV are counted. Taken from [15].

---

[1] For expressing the amount of distance traversed under a zenith angle θ respectively to the vertical direction until the altitude h in the atmosphere with variable density ϱ, it is convenient to use the atmospheric (or slant) depth $X(h) = \int_{\infty}^{h} \frac{\varrho(x)\mathrm{d}x}{\cos(\theta)}$.

The number of particles of such cosmic-ray air shower grows exponentially with traversed atmospheric depth until the energy of new particles drops below a critical value. Than it becomes more probable for a particle to decay before it can interact. An Extensive Air Shower created by UHECR primary particle with energy E_0 will have roughly $E_0/\text{eV} \times 10^{-10}$ secondary particles at maximum. A typical air shower profile can be seen in Fig. 1.4. A cosmic-ray air shower is comprised of four main components: hadron, electromagnetic, muon and neutrino component all schematically depicted in Fig. 1.5.

Hadronic component consists of mesons, baryons and nuclear fragments created through hadronical and spallation reactions of primary and secondary cosmic-ray particles with atmospheric molecules. Mostly (90 %) charged and neutral pions (π^0, $\pi^\pm$) are created. At smaller rate charged kaons are also created ($K^\pm$).

Pion π^0 is a neutral meson with mean lifetime $\tau = 8.52 \times 10^{-17}$ s. It decays instantly through two most probable channels

$$\begin{aligned} \pi^0 &\rightarrow \gamma + \gamma && 98.8\ \% && \text{(1.6a)} \\ &\rightarrow e^+ + e^- + \gamma && 1.2\ \%. && \text{(1.6b)} \end{aligned}$$

Pions $\pi^\pm$ are charged mesons with much longer mean lifetime $\tau = 2.6 \times 10^{-8}$ s. They can traverse hundreds of meters and interact with the atmosphere before decaying into muons and neutrinos with almost 100% probability:

$$\begin{aligned} \pi^+ &\rightarrow \mu^+ + \nu_\mu && \text{(1.7a)} \\ \pi^- &\rightarrow \mu^- + \bar{\nu}_\mu. && \text{(1.7b)} \end{aligned}$$

The less dominant collision products, kaons $K^\pm$, are mesons containing strange quark s. Mean lifetime is $\tau = 1.2 \times 10^{-8}$ s and its decay proceed through one of the following channels

$$\begin{aligned} K^+ &\rightarrow \mu^+ + \nu_\mu && 63.5\ \% && \text{(1.8a)} \\ &\rightarrow \pi^+ + \pi^0 && 20.6\ \% && \text{(1.8b)} \\ &\rightarrow \pi^+ + \pi^+ + \pi^- && 5.6\ \% && \text{(1.8c)} \\ &\rightarrow \pi^0 + e^+ + \nu_e && 5.0\ \% && \text{(1.8d)} \end{aligned}$$

(K^- decays to the charge conjugates of listed channels).

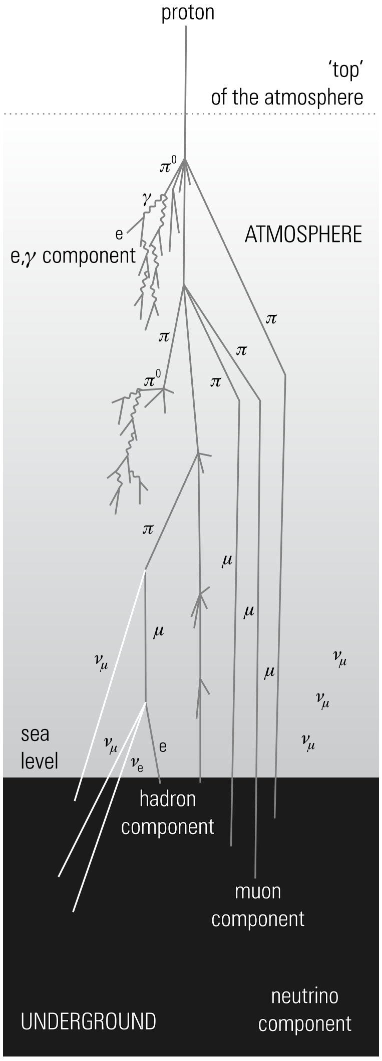

Figure 1.5: A model scheme of a cosmic ray shower composition. Taken from [17].

Decays of unstable charged pions (1.7a), (1.7b) and kaons (1.8a) give rise to the muonic part of the shower often called the hard component. Muons are unstable leptons with mean lifetime

$\tau = 2.2 \times 10^{-6}$ s. Highly relativistic muons reach the ground and create a substantial part of a surface detector signal in EAS arrays (see Sec. 2.1). Since muons excite the atmosphere minimally, they represent the first shower component carrying away invisible energy for fluorescence detectors. Muons decay into lighter leptons

$$\mu^+ \to e^+ + \nu_e + \bar{\nu}_\mu \tag{1.9a}$$

$$\mu^- \to e^- + \bar{\nu}_e + \nu_\mu . \tag{1.9b}$$

The most interacting shower component is the electromagnetic component which arises mainly from decays of neutral pions (1.6a),(1.6b) and little from kaon decays (1.8b), (1.8c) and (1.8d). Energetic photons can undergo a conversion process into electron and positron which can both subsequently emit new photons in the processes of bremsstrahlung. This electromagnetic cascade quickly amplifies the electromagnetic part of the shower which contributes to the major part of a fluorescence detector signal (see Sec. 2.2). Since the electromagnetic component is quickly dampen inside the atmosphere it is often called the soft component.

Finally, the last part of the shower consists of neutrinos emerged from various decay reactions. Neutrinos together with muons also carry away substantial part of the shower energy as they practically do not interact with atmosphere or surface detectors and can penetrate deep inside the Earth.

1.5 Air Shower models

Analytical solution for systems of cascade equations describing precisely all created particles and accounting for decays of unstable ones is not available. It is common to calculate shower numerically and to parametrize the results. However, semi-empirical models of electromagnetic showers described by W. Heitler with a possible generalization to hadronical shower by J. Matthews in [24] are also frequently used to understand basic shower properties.

1.5.1 Heitler model

The Heitler model of an electromagnetic cascade (Fig. 1.6) assumes that an electron (positron) emits a brehmsstrahlung photon after passing a splitting length d when it loses a half of its initial energy

$$d = \lambda_r \ln 2, \tag{1.10}$$

where λ_r is the radiation length (for an electron/positron in air $\lambda_r = 36.66$ g/cm^2). Same length d is considered for a photon to undergo a conversion to electron-positron pair. After n reactions the traversed length is $X = n\,\lambda_r \ln 2$ and there are

$$N = 2^n = e^{\frac{X}{\lambda_r}} \tag{1.11}$$

particles in the shower. Created particles are considered to have exactly half of mother's energy. When the energy decreases below the value of critical energy ξ_c^e, losses by ionization become larger than from brehmsstrahlung and the shower growth is stopped. (for electron/positron in air $\xi_c^e = 85$ MeV). Maximum particles in a shower with primary energy E_0 is

$$N_{max} = 2^{n_c} = \frac{E_0}{\xi_c^e}, \tag{1.12}$$

where n_c number of generations before reaching the critical energy. From Eq. (1.12) we have

$$n_c = \frac{\ln(E_0/\xi_c^e)}{\ln 2} \tag{1.13}$$

and we can approximate the traversed depth in which the electromagnetic shower reaches its maximum X_{max}^{γ} by

$$X_{max}^{\gamma} = n_c\, \lambda_r \ln 2 = \ln \frac{E_0}{\xi_c^e}. \tag{1.14}$$

From simple calculations we find that X_{max} is proportional to logarithm of primary energy. Important measurable parameter of air showers is the elongation rate D defined as

$$D^{\gamma} = \frac{\mathrm{d}\, X_{max}^{\gamma}}{\mathrm{d} \log E_0} \approx 85 \text{ g.cm}^{-2}. \tag{1.15}$$

This results for electromagnetic showers is not reproduced by MC models because the Heitler model neglects particles which can leave the shower and overestimates number of electrons and positrons over photons roughly by a factor of 10.

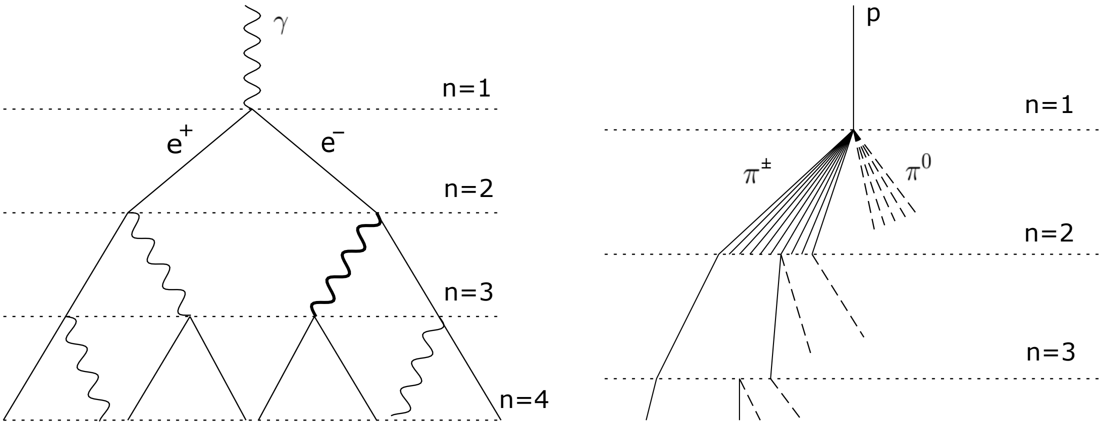

Figure 1.6: Scheme of electromagnetic cascade (a) and hadronic cascade (b), charged pions are represented by full lines, neutral by dashed ones. Taken from [24].

1.5.2 Heitler-Matthews model

Heitler model can be extended to characterize hadronic cascades in cosmic-air showers. We will assume the interaction length for strongly interacting particles does not vary much with energy and can be approximated by a constant $\lambda_I \approx 90$ g/cm^2. After traversing λ_I, a hadron interacts and creates N_{ch} charged and $\frac{1}{2}N_{ch}$ neutral pions.

Value N_{ch} grows with energy of the reaction but can be taken as $N_{ch} = 10$ on average. Created neutral pions π^0 decay instantly and give rise to electromagnetic sub-showers. Hadronic cascade stops when charged pions reach critical energy $\xi_c^\pi \approx 20$ GeV, when the mean traversed length is lower than interaction length and decay to muons is more probable than new interaction.

After n generations there is N_{ch}^n charged pions and if we assume equal division of energy between charged and neutral pions, the hadronic cascade will possess energy $\left(\frac{2}{3}\right)^n E_0$. The rest of primary energy is deposited in electromagnetic sub-showers from π^0 decays. A single pion will have energy

$$E_\pi = \frac{E_0}{\left(\frac{3}{2}N_{ch}\right)^n} \tag{1.16}$$

and number of generation to reach ξ_c^π will be

$$n_c = \frac{\ln(E_0/\xi_c^\pi)}{\ln(\frac{3}{2}N_{ch})} = 0,85 \log \frac{E_0}{\xi_c^\pi}. \tag{1.17}$$

If we approximate that all muons in proton induced shower are created by decays of charged pions in maximum, we can write

$$N_\mu^p = N_{max}^\pi = (N_{ch})^{n_c} = \beta_0 \left(\frac{E_0}{\xi_c^\pi}\right)^\beta \tag{1.18}$$

where β can be estimated using Eq. (1.16) as

$$\beta = \frac{\ln(N_{ch})}{\ln(\frac{2}{3}N_{ch})} \approx 0.85. \tag{1.19}$$

The estimation of the number of muons N_μ^p in a shower as a power function of primary energy in Eq. (3.4) is justified by Monte Carlo simulations giving values $\beta = 0.85 - 0.92$.

By combining the results from electromagnetic and hadronic cascades with restriction only for primary electromagnetic cascades it can be derived X_{max}^p for proton induced showers

$$X_{max}^p = X_I + \lambda_r \ln \frac{E_0}{3\, N_{ch}\, \xi_c^e}, \tag{1.20}$$

where $X_I = \lambda_I \ln 2$ is the atmospheric depth of the first proton interaction. The equation (1.20) underestimates the X_{max} in comparison with MC simulations, mainly because it neglects electromagnetic sub-showers. However, the value of elongation rate D^p for proton showers calculated from Eq. (1.20) gives value in good agreement with MC simulations:

$$D^p = \frac{\mathrm{d}}{\mathrm{d}\log E_0}(X_I + \lambda_r \ln \frac{E_0}{3\, N_{ch}\, E_c}) \approx 58 \text{ g/cm}^2. \tag{1.21}$$

1.5.3 Superposition model

When considering air showers induced by heavier nuclei it is convenient to use the superposition model. The hadronic interaction of a nucleus with mass number A and primary energy E_0 is treated as a superposition of A collisions creating A proton-induced showers with primary energy E_0/A. This simplifies the problematics of nucleus interaction of bind state of many nucleons. It is possible to express nucleus-induced shower parameters using results for proton-induced shower

$$X_{max}^A = D^p \log\left(\frac{E_0}{A}\right) \tag{1.22a}$$

$$N_\mu^A = N_\mu^p A^{1-\beta}. \tag{1.22b}$$

1.5.4 Monte Carlo simulations

Monte Carlo simulation codes are available for more exact description of the shower than those in Sec. 1.5.2, 1.5.3. The codes use MC techniques to decide when and where a given particle interacts or decays in the atmosphere. The software tracks all of representative parts of the produced particles and thus it simulates the shower in the whole atmosphere. For purposes of the description of the particle interaction the software uses a chosen model of hadronic interactions such as EPOS [30] and QGSJET [27]. Two codes to simulate cosmic-ray air shower are used in this thesis: CONEX and CORSIKA.

CONEX [13] combines MC simulations of particle interactions with numerical evaluation of cascade equations to obtain fast 1D shower data. Explicit MC simulation of the high-energy part of hadronic and electromagnetic cascades in the atmosphere is combined with a numeric solution of cascade equations for smaller energy sub-showers to obtain accurate shower predictions. CONEX calculates not only observables related to the number of particles (shower size) but also ionization energy deposit profiles which are needed for the interpretation of data of experiments employing the fluorescence light technique. The output of the CONEX simulation program is thus the full shower longitudinal profile expressed in ionization deposit and the number of particles. On the other hand no information is stored for individual particles that reached the ground level.

CORSIKA (COsmic Ray SImulations for KAscade) [18] is a program for detailed 3D simulation of extensive air showers initiated by high energy cosmic ray particles. Protons, light nuclei up to iron, photons, and many other particles may be treated as primaries. CORSIKA may be used up to and beyond the highest energies of 100 EeV. The particles are fully tracked through the atmosphere until they undergo reactions with the air nuclei or - in the case of unstable secondaries - decay. The output of the CORSIKA is not only the information for longitudinal shower profile but also the detailed information about particles reaching ground level.

Chapter 2

The Pierre Auger Observatory

The Pierre Auger Observatory is the largest experiment for the observation of Extensive Air Showers induced by the UHECR. It is located in the Argentinian pampas near the city of Malargüe. The PAO was designed to have sufficient area for detection of enough EAS events from the end of cosmic-ray spectrum at energies above 10^{18} eV. Proposals for the observatory have been laid in 1991 by J. Cronin and A. Watson and construction works began in 2002. First cosmic-ray data were collected in 2004 and full operation was achieved in 2008. Nowadays, the PAO collaboration associates more than 500 scientists from 19 countries and an upgrade of the observatory - AugerPrime - is underway.

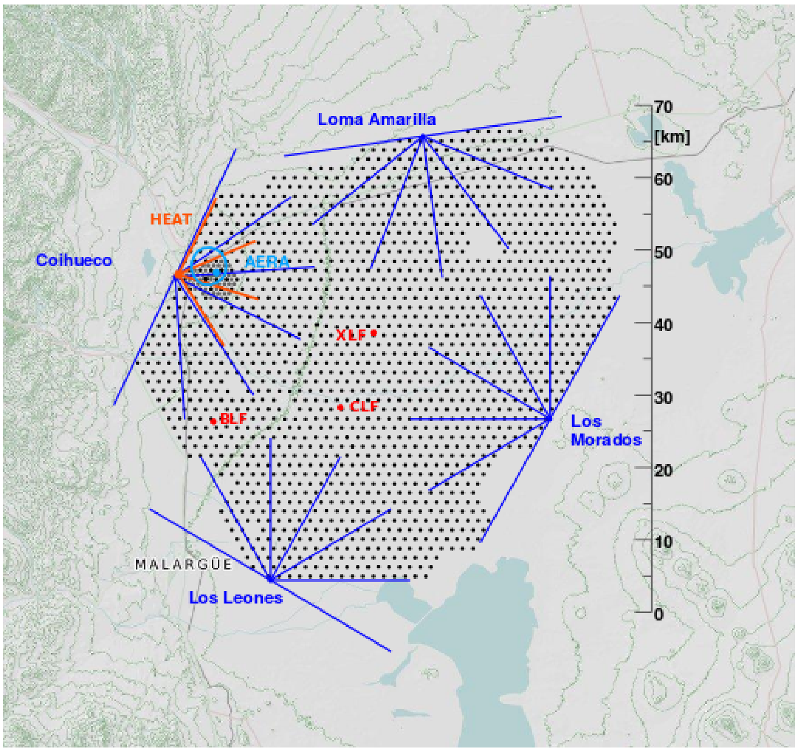

Figure 2.1: The layout of the Pierre Auger Observatory. Every black dot represents one of the Surface Detector station also with a denser Infill array. Four fluorescence stations - Loma Amarilla, Morandos, Leones, Coihueco - and HEAT fluorescence extension are depicted. Two stations for FD calibration - CLF (Central Laser Facility) a XLF (eXtreme Laser Facility) and weather balloon launching facility (BLF) are shown.

The Observatory has a hybrid design, combining an array of Surface Detectors (SD) and Fluorescence detectors (FD). The SD consist of more than 1660 Water Cherenkov Stations in a triangular grid with 1.5 km spacing and also in a extended denser Infill array with 750 m spacing. The overall SD area is around 3000 km^2. The FD stations - Loma Amarilla, Morandos, Leones, Coihueco - each contain 6 fluorescence telescopes, overwatching the sky above SD and searching for an UV fluorescence light emitted by excited atmospheric molecules. A number of extensions to the observatory have been added since the start of operation - the HEAT fluorescence detector and the AMIGA project both designed for measuring showers with energy below 10^{17} eV. Also a shower detection through emitted radio pulses is implemented in AERA project. For schematic layout of the Pierre Auger Observatory see Fig. 2.1.

Mean altitude of the observatory is 1400 m, that corresponds to atmospheric depth of 880 g/cm^2. The hybrid approach for the shower detection combines information from both types of detectors when possible thus effectively makes the measurement more precise. Events reconstructed by both SD and FD are called Golden events and are used for SD signal calibration by the energy measured with the FD. Up to 6000 Golden events with energy around 10^{18} eV are detected per year. At energies above 10^{19} eV it is around 300 Golden events per year. Moreover 90 % of events above 3×10^{19}eV are registered by more than one FD station, making the reconstruction even more precise.

2.1 Surface detector

The surface detector at the PAO is spanned over 3000 km^2 with 1600 water Cherenkov stations. Stations are aligned in a regular triangual grid with 1.5 km distance between every two stations. An extension of 60 stations was added later near the FD station Coihueco to form a denser grid with 750 m spacing - Infill - to observe showers with lower energies around 10^{17} eV.

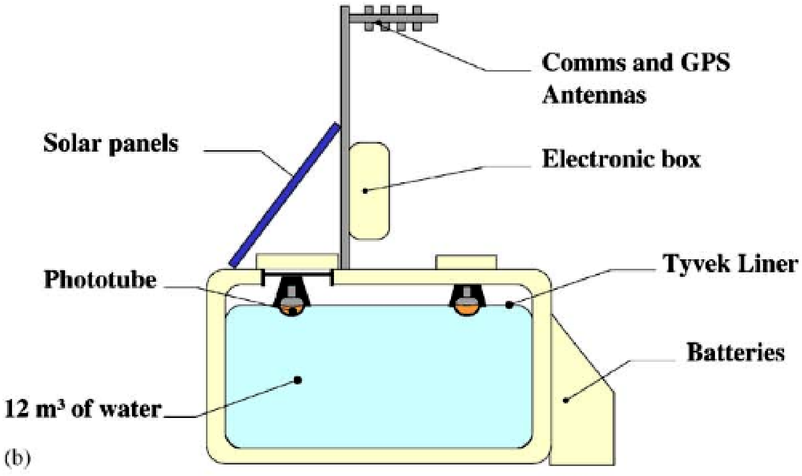

Figure 2.2: A scheme of one SD station with description of main parts. Taken from [9].

Each SD station is a polyethylene cylinder tank with diameter 3.6 m and height 1.2 m, containing 12 000 liters of pure demineralised water. When a relativistic charged particle traverses the water mass, the Cherenkov light is emitted and detected by three 9-inch photomultiplier tubes (PMT). A depicted station is in Fig. 2.2. The station is sensitive to electromagnetic as well as muon component of a shower and the registered signal is measured in Vertical Equivalent Muons (VEM) - signal corresponding to a 250 MeV muon passing the station vertically. Measured signal is digitalized by the station electronics and sent automatically with data from other activated stations for reconstruction via a system of antennas. Each station is supplied by 12 V batteries charged by a solar panel.

The main advantage of the SD is 100% duty cycle independent of local atmospheric conditions and sunlight. From the timing of triggered surface stations that have been hit by a shower front, a shower axis can be reconstructed. Depending on the number of activated stations, the reconstruction can be better than 1° at energies above 10 EeV. Showers with zenith angle up to 60° for regular SD and up to 55° for Infill can be reconstructed by the SD. Shower energy can be reconstructed from SD signals using a relation between energy measured by FD detectors and SD signal of Golden events (see Sec. 2.3.2).

One of the main part of AugerPrime upgrade is installation of 4 m^2 plastic scintillators. As scintillators are more sensitive to shower electromagnetic component in comparison to Cherenkov detectors which are sensitive to both EM and muon component, a better estimation of muon signal is expected from combination of simultaneous measurements of both detectors [7]. Furthermore, an upgrade for the station electronics and PMT signal readout is currently underway to improve station dynamic range and to decrease the amount of saturated PMT signals in the stations near the shower core.

2.2 Fluorescence detector

Four main fluorescence detector sites overwatch the surface detector array - Los Leones, Los Morados, Loma Amarilla and Coihueco - and the HEAT (High Elevation Auger Telescope) fluorescence station extension near the Coihueco for detection of less energetic showers developing at higher altitudes. Each of four main sites consists of six separated fluorescence telescopes with $30^\circ \times 30^\circ$ field of view resulting in the 180° coverage in azimuth. One fluorescence station and a detail scheme of one fluorescence telescope are shown in Fig. 2.3.

The UV light ($300 - 400$ nm) is emitted isotropically from nitrogen molecules by deexcitation and its amount is proportional to a deposited energy by shower ionizing particles. The fluorescence yield per 1 MeV of the deposited energy in the air under normal conditions (1013 hPa, 293 K) is approximately 5.6 photons of wavelength 337 nm. The fluorescence signal is very dim therefore only nights with the moon light fraction less than 60 % are suitable for measuring. This limits the overall duty cycle of

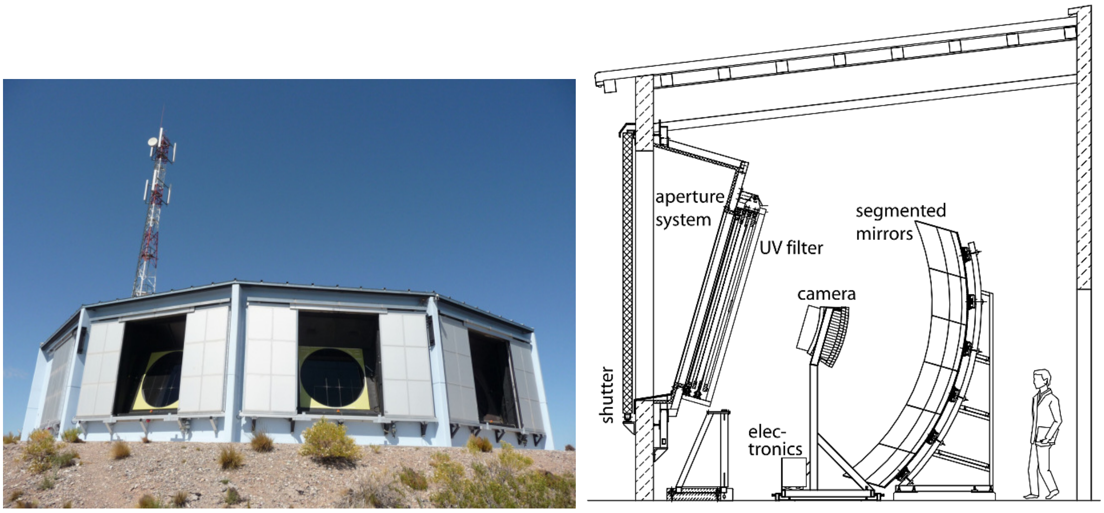

Figure 2.3: A photograph of Los Leones fluorescence station (left) and a scheme of one of six fluorescence telescopes in one station. Taken from [10].

the FD to only 13 % of total time.

Any background noise (e.g. shower Cherenkov light in air) must be subtracted and UV light scattering on atmospheric aerosols must be accounted for. For that, careful measurement of atmosphere properties expressed in quantities such as the Vertical Aerosol Optical Depth (VOAD) are carried out on hourly basis by several independent methods - two laser stations CLF, XLF, Lidar stations at each FD site and FRAM telescope at the Los Leones site. For more information about atmospheric monitoring at the PAO one should see [3].

The UV light enters fluorescence telescope through an optical filter transmitting only photons up to 410 nm in wavelength and thus eliminating the noise of any visible photons. Light is then transmitted through an aperture and a corrector ring onto a large 13 m^2 segmented spherical mirror focusing the light on a 440 pixel camera. Every pixel represents a hexagonal photomultiplier tube (PMT) capable of detecting even single photons. The amount of photons detected corresponds to shower energy deposit into the atmosphere at given location (with atmospheric corrections applied). Light pulses in PMTs are being read every 100 ns and time order of activated PMTs enables the reconstruction of shower axis and direction.

2.3 Shower reconstruction

The EAS can be reconstructed both from SD and FD data alone, but the best results are obtained with hybrid detection when both detector systems have been triggered by a single shower. Both reconstruction procedures are described in this section.

2.3.1 FD reconstruction

A sequence of activated fluorescence telescope pixels can be seen in Fig. 2.4(left) with blue representing the first pixels being activated and red the last ones. From the knowledge of activated pixel positions a shower-detector plane (SDP) depicted in Fig. 2.4(right) is fixed as the plane containing telescope position and shower axis.

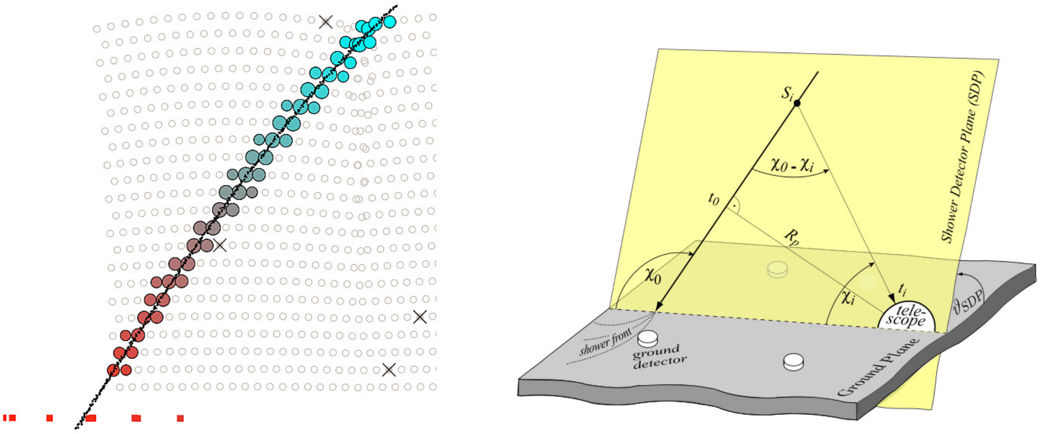

Figure 2.4: Left: A picture of the time progression of activated pixels in the fluorescence telescope by a cosmic ray shower with blue pixels being activated earlier than the red ones. Red squares represent activated surface detectors by the shower front. Right: A scheme of the shower-detector plane with depiction of important measured and fit parameters at a shower axis. Both pictures taken from [10].

Next, the time information of activated pixels is used to reconstruct the shower axis within the SDP. If the distance of closest approach of the shower axis to the telescope is R_p and shower front have crossed this point in time t_0, the time of i-th pixel activation can be represented by an equation

$$t_i = t_0 + \frac{R_p}{c} \operatorname{tg}\left(\frac{\chi_0 - \chi_i}{2}\right), \tag{2.1}$$

where c is the speed of light in vacuum, χ_0 is the angle between the shower axis and a ground plane in the SDP and χ_i is the angle between i-th activated pixel and the ground plane in the SDP. By fitting the equation (2.1) to measured χ_i and t_i one can obtain the shower axis parameters R_p and χ_0.

Possible variety of fitted (R_p,χ_0) for a single shower can be resolved by utilizing data from activated surface detectors which significantly lowers the total error of the shower reconstruction to 50 m in shower core location and 0.6° in shower arrival direction. This hybrid detector approach is very useful since the surface detectors duty cycle is 100% and majority of events above $10^{18.3}$ eV detected by the fluorescence detectors is accompanied by activation of several surface stations. At high energies it is possible that an event is simultaneously observed by two and more FD sites. In this case the shower geometry can be independently estimated as an intersection of two shower detector planes, see Fig. 2.5(left).

With shower geometry being reconstructed, next step is to estimate shower energy deposition into the atmosphere by measuring the light collected by the fluorescence telescopes. Resulting plot of the shower energy deposition into the atmosphere is shown in Fig. 2.5(right). It is fitted by the Gaisser-Hillas function

$$f_{GH}(X) = \left(\frac{\mathrm{d}E}{\mathrm{d}X}\right)_{max} \left(\frac{X - X_0}{X_{max} - X_0}\right)^{\frac{X_{max}-X_0}{\lambda}} e^{\frac{X_{max}-X}{\lambda}}. \tag{2.2}$$

This four-parameter fit estimates the largest energy deposit $(\mathrm{d}E/\mathrm{d}X)_{max}$ as well as the slant depth of this maximum X_{max}. Two other parameters X_0 and λ represent the slant depth of first interaction and radiation length respectively. With the function (2.2) fitted to the shower energetic profile, its integral by slant depth reveals the shower calorimetric energy.

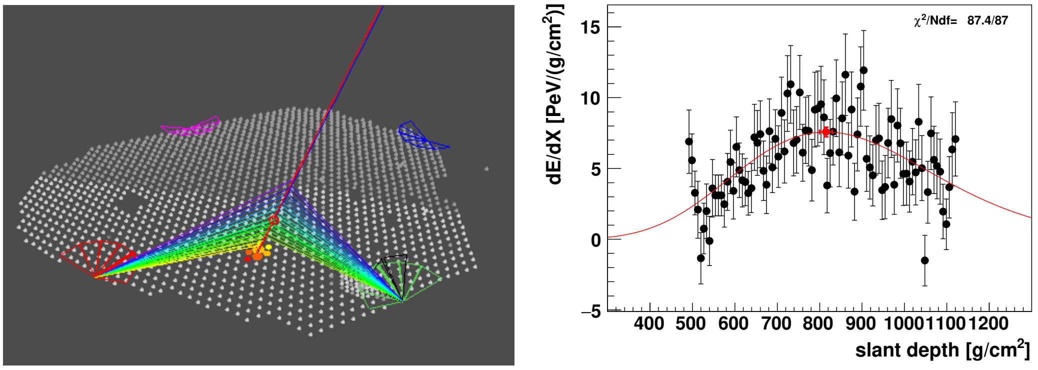

Figure 2.5: Left: Reconstructed shower detected by two FD stations with estimated energy $E = 6.55 \pm 0.41$ EeV. Right: Energy deposit profile of the same shower fitted by the Gaisser-Hillas function. Both pictures are taken from the EventBrowser program for EAS reconstruction at the PAO.

Mentioned already, the computed value represents roughly 80 − 95 % of the shower total energy. The rest of the shower energy - "invisible energy" - is carried away in the form or muons and neutrinos. The non-interacting shower fraction is estimated using Monte Carlo simulations for various primary particle parameters and will be discussed in the following chapters of this thesis.

2.3.2 SD reconstruction

The shower front of Extensive Air Showers can reach up to several kilometers in diameter. When the shower reaches the ground multiple SD stations are very probably triggered. System of hardware triggers determine which acquired data are physically relevant and are passed on to shower reconstruction. For more precise shower reconstruction so called 6T5 trigger can be applied. It counts only events with all 6 active SD stations around a central one (a working hexagon) with the highest signal. Activated SD stations signal with ordered trigger times can be seen in Fig. 2.6(right) for a detected shower with reconstructed energy $6.55 \pm 0.41\,\mathrm{EeV}$.

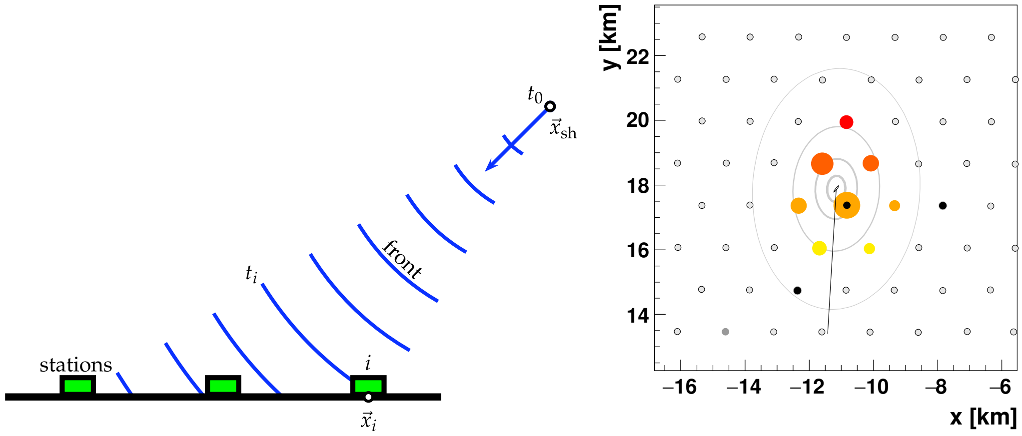

Figure 2.6: Left: Shower axis reconstruction using trigger timing information of the SD array. Taken from [6]. Right: Activated SD stations with the reconstructed shower core and arrival direction. Size of the circles corresponds to logarithm of signal strength and their colors correspond to time information with yellow (red) color representing earlier (later) triggering. Picture taken from the EventBrowser program for EAS reconstruction at the PAO.

Reconstruction of a shower axis using the SD array is shown in Fig. 2.6(left). When we approximate the shower front as a sphere inflating with the speed of light c and take known times t_i of i-th station activation with position $\vec{x}_i$ it is possible, by fitting the equation

$$c(t_i - t_0) = |\vec{x}_{sh} - \vec{x}_i|, \tag{2.3}$$

to obtain shower virtual starting position $\vec{x}_{sh}$ and time t_0. According to lateral shower profile in Fig. 1.4(a) station signals should fall quickly with increasing lateral distance r from the shower core position. The signals are fitted with the Lateral Distribution Function (LDF) in the form

$$S(r) = S(r_{\rm opt}) \left(\frac{r}{r_{\rm opt}}\right)^{\beta} \left(\frac{r + r_1}{r_{\rm opt} + r_1}\right)^{\beta+\gamma}, \tag{2.4}$$

where $r_1 = 750$ m, $r_{\rm opt}$ is optimal distance at which reconstructed SD signal has minimal uncertainty. For 1.5 km SD grid, the optimal distance was chosen $r_{\rm opt} = 1000$ m, hence the signal in the optimal distance is $S(1000)$. The parameter β is reflecting a shower size and zenith angle. Showers up to zenith angle $\theta = 60°$ have steeper LDF than more inclined ones, because the SD signal is caused by showers at a younger stage of development with smaller ratios of muon to electromagnetic part. The LDF function for the same reconstructed shower as in Figs. 2.5, 2.6(right) is shown in Fig. 2.7.

From maximum likelihood LDF fit the shower core position on the ground $\vec{x}_{gr}$ is estimated and the shower axis can then be calculated as

$$\vec{a}_0 = \frac{\vec{x}_{sh} - \vec{x}_{gr}}{|\vec{x}_{sh} - \vec{x}_{gr}|}. \tag{2.5}$$

The angular resolution achieved is better than 1.6° for events with more than three hit

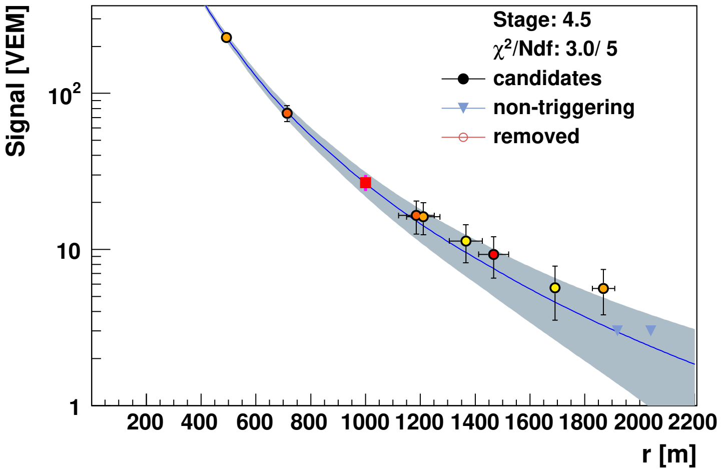

Figure 2.7: Lateral distribution function fitted to SD signals induced by a shower with reconstructed energy 6.55 ± 0.41 EeV and zenith angle $\theta = 45.6 \pm 0.4^\circ$. Taken from the EventBrowser program.

stations and reaching 0.9° for events with more than six activated stations.

For energy calibration of the SD, simultaneous measurements during moonless nights by both types of detectors (Golden events) are used to find a relation between reconstructed FD energy and SD signal. The optimal SD signal $S(1000)$ is dependent on the zenith angle θ as can be seen in Fig. 2.8(left). A Constant Intensity Cut method [19] is applied by fitting the $S(1000)$ zenith dependence by a third degree polynomial

$$f_{\mathrm{CIC}}(x(\theta)) = 1 + a\,x(\theta) + b\,x(\theta)^2 + c\,x(\theta)^3, \tag{2.6a}$$

$$x(\theta) = \cos^2\theta - \cos^2\bar{\theta}. \tag{2.6b}$$

The zenith angle $\bar{\theta} = 38^\circ$ was chosen as the reference angle to which other shower signals with different θ are converted

$$S_{38} = \frac{S(1000)}{f_{\mathrm{CIC}}(\theta)}. \tag{2.7}$$

S_{38} is effectively the signal $S(1000)$ of the same shower if it would come under zenith angle $\theta = 38^\circ$. The parameters of $f_{CIC}(\theta)$ function were found from PAO measurements as $a = 0.980 \pm 0.004$, $b = -1.68 \pm 0.01$ and $c = 1.30 \pm 0.45$ [1].

Relation between the S_{38} signals and fluorescence detector energies E_{FD} for 1475 carefully selected Golden events satisfying multiple conditions was used. The resulting parametrization by the power law

$$E_{FD} = A(S_{38}/\mathrm{VEM})^B, \tag{2.8}$$

was fitted in Fig.2.8(right) with the result: $A = (1.9 \pm 0.05) \times 10^{17}$ eV and $B = 1.025 \pm 0.007$ [1]. The total systematic error of energy scale at the PAO is estimated to 14 % and it is dominated by absolute calibration of response of fluorescence detectors.

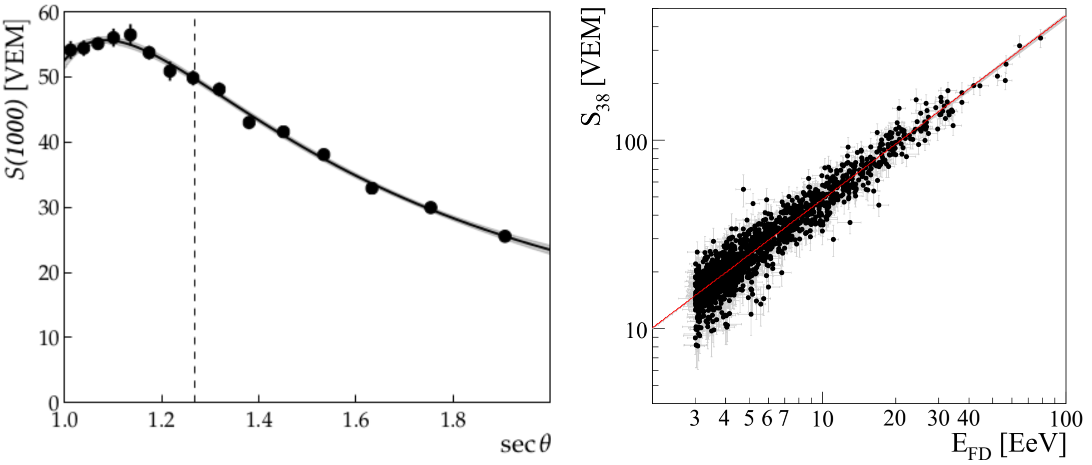

Figure 2.8: Left: Lateral Distribution Function fitted to data from the PAO. The dashed line represents the signal $S(1000)$ for showers with $\theta = 38^\circ$ and corresponds to signal 50 VEM. Right: The relation between the converted signal S_{38} and shower energy E_{FD}. Taken from [6].

The invisible energy uncertainty contributes to the total systematic uncertainty by 3 % [6].

2.4 Selected results of the Pierre Auger Observatory

Since the beginning of data acquisition in 2004 until 2016 a substantial number of EAS events were collected at the Pierre Auger Observatory with an overall exposure exceeding 67000 $\mathrm{km}^2\,\mathrm{sr}\,\mathrm{yr}$. Thanks to that, several major contributions to the field of UHECR were made. Some of them such as observed cosmic-ray flux, mass compositions and arrival directions are briefly described here.

2.4.1 Energy spectrum

Measurement of the energy spectrum above 3×10^{17} eV was done using multiple detector systems as can be seen in Fig. 2.9. Events detected by the SD-1500 grid with both vertical ($\theta < 60^\circ$) and inclined ($\theta > 60^\circ$) showers were accounted after passing several quality cuts. Data from the SD-750 Infill array were used in lower energy part of the spectrum as well as hybrid events (i.e. events recorded by the FD that also triggered at least one SD station) at energies higher than 1 EeV.

The measured spectrum by all detectors is fitted globally by maximum likelihood fit. The results are shown in Fig. 2.10, depicting the energy at which the "ankle" occurs as $E_{ankle} = 5.08 \pm 0.08\,(\mathrm{stat.}) \pm 0.8\,(\mathrm{syst.})$ EeV with the spectral index changing from $\gamma_1 = 3.293 \pm 0.002\,(\mathrm{stat.}) \pm 0.05(\mathrm{syst.})$ to $\gamma_2 = 2.53 \pm 0.02\,(\mathrm{stat.}) \pm 0.1(\mathrm{syst.})$. The energy of the flux suppression at the "toe" occurs at $E_s = 39 \pm 2\,(\mathrm{stat.}) \pm 8\,(\mathrm{syst.})$ EeV and the energy at which the integral spectrum lowers by a factor of two below what would be expected without any suppression is $E_{1/2} = 23 \pm 1\,(\mathrm{stat.}) \pm 4\,(\mathrm{syst.})$ EeV.

The suppression of the spectrum at the high energies is confirmed with large statistical certainty. Within the systematic uncertainties the results are compatible with measured spectrum of the Telescope Array. The position of the "ankle" is moved between the two observatories by 10 % and the energy spectrum at the "toe" is shifted up by 70 % in the TA. It is not known whether this shift is due to the lack of sufficient statistics or due to different fluxes of primary particles at different locations of the two observatories.

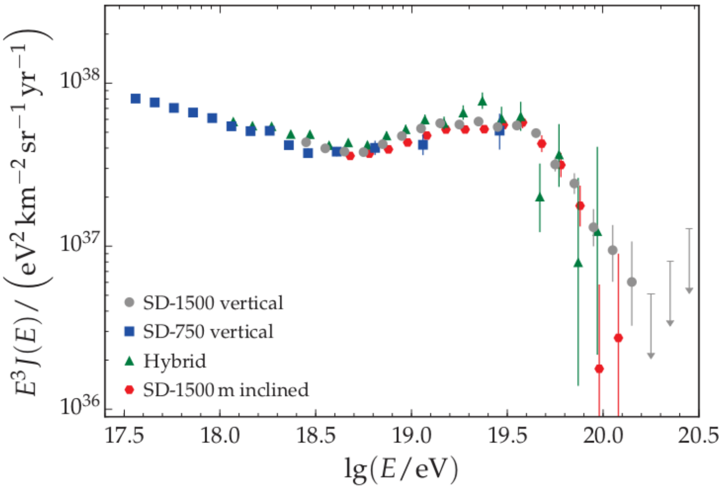

Figure 2.9: Energy spectra measured by different detector systems at the PAO. Systematic error for all data is 14 %. Taken from [2].

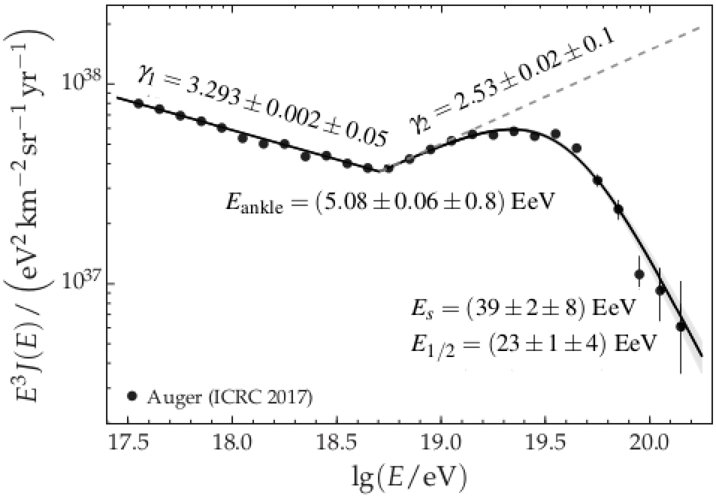

Figure 2.10: Fitted energy spectrum measured by the PAO. Energies of spectral breaks and corresponding spectral indexes are shown with statistical and systematical errors. Taken from [2].

2.4.2 Mass composition

Important measurements of shower depth of maximum X_{max} as the most direct indicator of the primary mass composition were made utilizing the fluorescence detectors at the PAO [4]. The mean measured $\langle X_{max}\rangle$ values as well as fluctuations $\sigma(X_{max})$ for a given energy bin are plotted in Fig. 2.11. When compared to predictions of models tuned to LHC data such as EPOS LHC and QGSJetII-04, a clear shift towards heavier composition occurs at energy 3×10^{18} eV. Below this energy the mass composition seems to be rather light until the elongation rate changes significantly. The change is supported by change in the X_{max} variance $\sigma(X_{max})$ in the same energy region. The size of the fluctuations relative to the mean X_{max} implies small primary mass variability in given energy region.

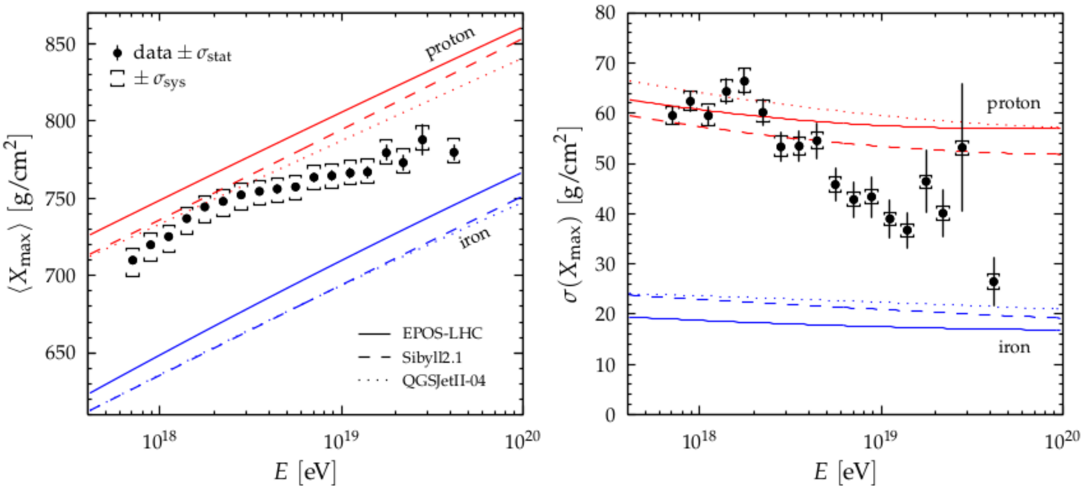

Figure 2.11: Mean X_{max} values and fluctuations in X_{max} as measured by the PAO. Model predictions for showers induced by proton and iron nucleus are drawn for comparison. Taken from [7].

2.4.3 Arrival directions and anisotropy

Significant measurements of arrival direction of the UHERC above 8 EeV at the PAO have shown large scale dipole anisotropy with an amplitude $6.5^{+1.3}_{-0.9}$ % in the direction of right ascension $\alpha_d = 100 \pm 10^\circ$ and declination $\delta_d = -24^{+12^\circ}_{-13}$ [8]. This has a probability of 2.6×10^{-8} for arising by a chance. A normalized rates of events as a function of right ascension in shown in Fig. 2.12 and fitted with first-harmonic function of Fourier series. A three-dimensional reconstruction of the cosmic-ray flux dipole in equatorial coordinates can be seen in Fig. 2.13.

Measurements for lower energy bin ($4\,\text{EeV} \leq E \leq 8\,\text{EeV}$) processed 81701 events and small dipole of amplitude $2.5^{+1.0}_{-0.7}$ towards the area of celestial south pole $(\alpha_d, \delta_d) = (80^\circ, -75^\circ)$ was found. This dipole is statistically unimportant when compared to the one for energy bin $E \geq 8\,\text{EeV}$. This indicates that the UHECR above the "ankle" are clearly extragalactic origin [8].

The detected dipole character of the UHECR at the highest energies cannot be directly used for possible sources indication due to effect of Galaxy magnetic field. Studies to correlate arrival directions of cosmic rays above $E \geq 58\,\text{EeV}$ to possible

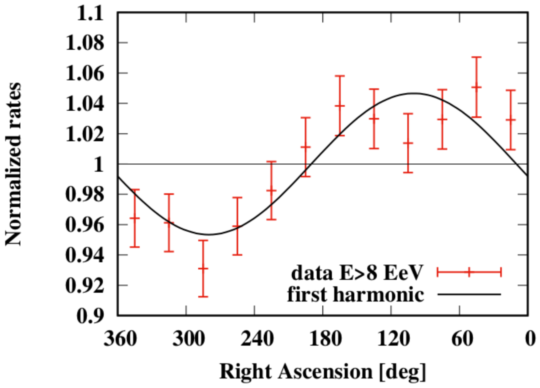

Figure 2.12: Rate normalized to all 32187 events for energy $E \geq 8\,\mathrm{EeV}$ as a function of right ascension. The data fits well to a dipole character cosmic-ray arrival direction ($\chi^2/n = 10.5/10$). Taken from [8].

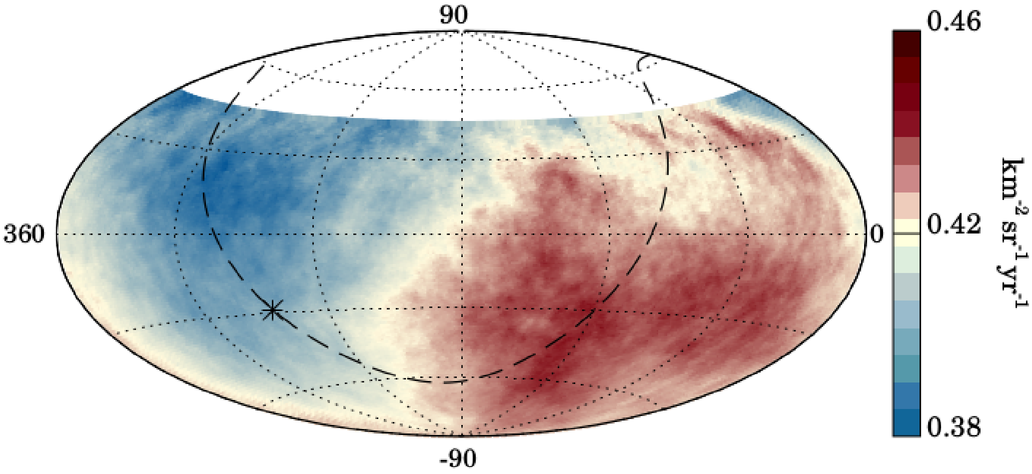

Figure 2.13: The map of cosmic-ray fluxes for energy $E \geq 8\,\mathrm{EeV}$ in equatorial coordinates. The Galactic center is marked with asterisk and the dashed line shows the Galactic plane. Taken from [8].

UHECR sources were done indicating a noticeable rise from isotropic flux around the AGN Centaurus A sky region. This anisotropy has a 1.4 % chance of arising from isotropic flux which is still statistically unsatisfactory to make firm conclusions. [5]

Chapter 3

Invisible energy in cosmic-ray showers

As was stated in the previous chapter, successful reconstruction of the shower primary energy by the FD (hence subsequently also by the SD) requires a solid estimation of the invisible energy in cosmic-ray showers. Several methods using Monte Carlo simulations in combination with data measured at the Pierre Auger Observatory were proposed [12], [1]. Currently used one at the PAO utilizes parametrization of the invisible energy as a function of the measured calorimetric energy. The parametrization process is described in [23].

3.1 Invisible energy estimation using CONEX

For an initial estimate of the mean invisible energy in cosmic-ray air showers and its dependence on primary particle type and energy as well as dependence on used hadronic interaction model, MC simulations by program CONEX were used (see Sec. 1.5.4). A large sample of cosmic-ray air showers was simulated using the newest hadronic interaction models - EPOS LHC and QGSJET-II-04. Seven primary energy groups with values of $\log(E_0/\mathrm{eV})$ - 17, 17.5, 18, 18.5, 19, 19.5, 20 - and two primary particle types - proton and iron nucleus - were included. For every possible combination of previously listed initial parameters and interaction models 200 showers were simulated with total number or simulations reaching 5600. A shower zenith angle was held at 60° for every simulated shower to obtain a long shower profile.

The invisible energy of a simulated cosmic ray shower was calculated as a difference between the simulated primary energy and the calorimetric energy that was estimated for each simulated shower similarly to the reconstruction process at the PAO as described in Sec. 2.3.1. With the knowledge of the shower longitudinal profile, energy deposition $\mathrm{d}E/\mathrm{d}X(X)$ is fitted according to the Gaiser-Hillas function (2.2) and integrated to obtain the shower calorimetric energy as follows

$$E_{cal} = \int_0^\infty f_{GH}(X)\mathrm{d}X. \tag{3.1}$$

Numerical integration of simulated shower data is one way to obtain the results needed. However, an analytical form of the integral (3.1) exists in the following form

$$E_{cal} = \lambda \left(\frac{\mathrm{d}E}{\mathrm{d}X}\right)_{max} \left(\frac{e\lambda}{X_{max} - X_0}\right)^{\frac{X_{max}-X_0}{\lambda}} \Gamma\left(\frac{X_{max} - X_0}{\lambda} + 1\right), \tag{3.2}$$

where Γ represents the Gamma function. By inserting parameter $(\mathrm{d}E/\mathrm{d}X)_{max}$ from Eq. (3.2) into Eq. (2.2) we obtain

$$f_{GH}(X) = \frac{E_{cal}}{\lambda} \left(\frac{X - X_0}{\lambda}\right)^{\frac{X_{max}-X_0}{\lambda}} e^{\frac{X_0-X}{\lambda}} \left[\Gamma\left(\frac{X_{max} - X_0}{\lambda} + 1\right)\right]^{-1}. \tag{3.3}$$

Hence, new fitting relation was obtained with E_{cal} becoming one of the fit parameters so that the shower calorimetric energy can be directly calculated by fitting Eq. (3.3) to the shower longitudinal energy deposit profile. The fitting itself remains four-parametric in E_{cal}, X_{max}, X_0 and λ.

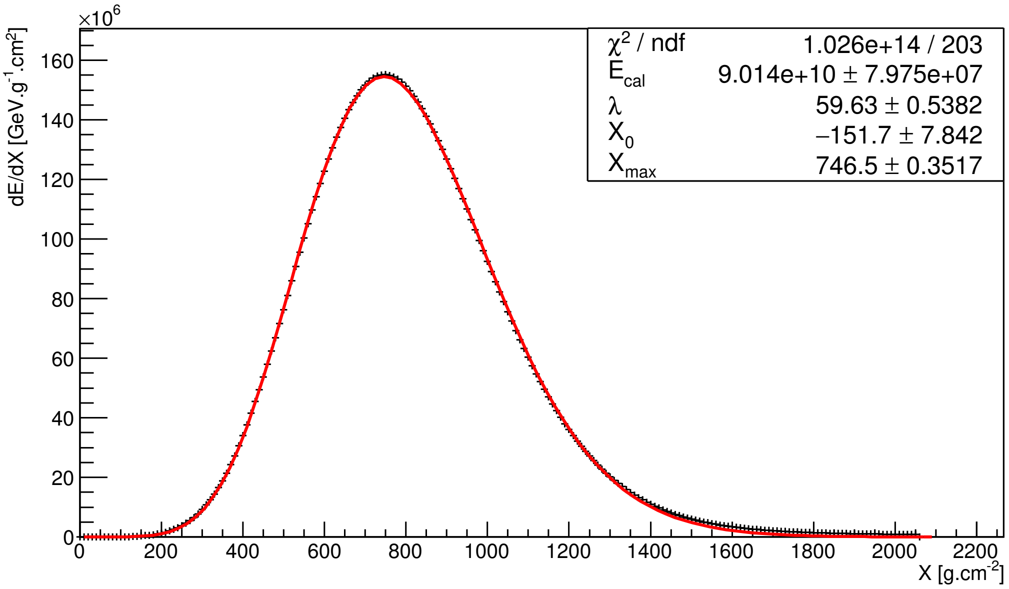

Figure 3.1: A fitted longitudinal energy deposit profile of a 10^{20} eV iron-induced shower simulated in CONEX using QGSJET-II-04 interaction model. E_{cal} is expressed in GeV, λ_0, X_0 and X_{max} in g.cm^{-2}.

For every simulated shower two step fitting procedure was realized. First, the simulated shower energy deposit profile was fitted to Eq. (2.2) to estimate the parameters X_{max}, X_0 and λ. Then a second fit was performed to Eq. (3.3) while utilizing the parameters estimated in the previous fit and additionally the new parameter E_{cal}

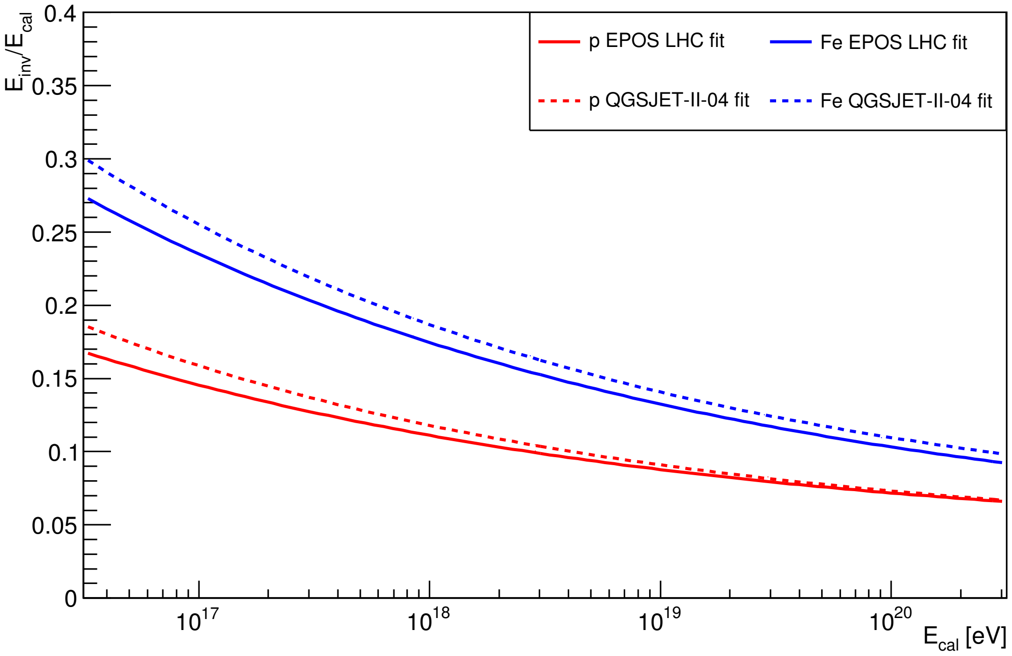

Figure 3.2: The behavior of E_{inv}/E_{cal} ratio as a function of E_{cal} for different primary energies and particle types shows decrease in the invisible energy portion with increasing E_{cal}.

was used instead of $(\mathrm{d}E/\mathrm{d}X)_{max}$. An example of fitted plot of simulated shower energy deposit profile of a 10^{20} eV iron-induced shower is shown in Fig. 3.1. The analytical calculation of E_{cal} as used at the PAO neglects the fact that a numerical integration of longitudinal energy deposit profile can yield more precise results. Here we stick to the approach applied at the PAO where the analytical integration is performed as well.

By estimation of average E_{cal} for all showers with the same primary energy and primary particle type, the general behavior of invisible to calorimetric energy ratio

$$\frac{\langle E_{inv}\rangle}{\langle E_{cal}\rangle} = \frac{E_0}{\langle E_{cal}\rangle} - 1 \tag{3.4}$$

was found by fitting the average values by simple power law function of E_{cal}. With increasing calorimetric energy the E_{inv}/E_{cal} ratio decreases as can be seen in Fig. 3.2. The results from both interaction models are comparable, albeit higher by cca $1-2$ % for QGSJET-II-04 in comparison with EPOS LHC with the difference also decreasing with E_{cal}. The highest portion of invisible energy is predicted for iron induced showers having up to 25 % for $E_{cal} = 10^{17}$ eV and falling to around 10 % for $E_{cal} = 10^{20}$ eV. Smaller invisible energy portion is predicted for proton induced showers reaching around 15 % and 7 % for the same extremal calorimetric energies.

3.1.1 C_{miss} parametrization

Let us define, similarly to other papers [12], [25], [26], the parameter C_{miss} by the relation

$$C_{miss}(E_{cal}) = \frac{E_{cal}}{E_0}. \tag{3.5}$$

Therefore, with the knowledge of behavior of the quantity $C_{miss}(E_{cal})$ for different E_{cal}, one can simply obtain the shower primary energy from measured calorimetric energy as follows

$$E_0 = \frac{E_{cal}}{C_{miss}(E_{cal})}. \tag{3.6}$$

Because of shower-to-shower fluctuations of calculated E_{cal} for the same parameters of shower primary particle, one needs to consider parametrization of C_{miss} as a function of mean $\langle E_{cal}\rangle$ calculated for all simulated bins of different primary particle types and energies. A good parametrization is

$$C_{miss} = \frac{\langle E_{cal}\rangle}{E_0} = a - b\left(\frac{\langle E_{cal}\rangle}{\mathrm{EeV}}\right)^c, \tag{3.7}$$

where a, b and c are constants characterizing used hadronic interaction model.

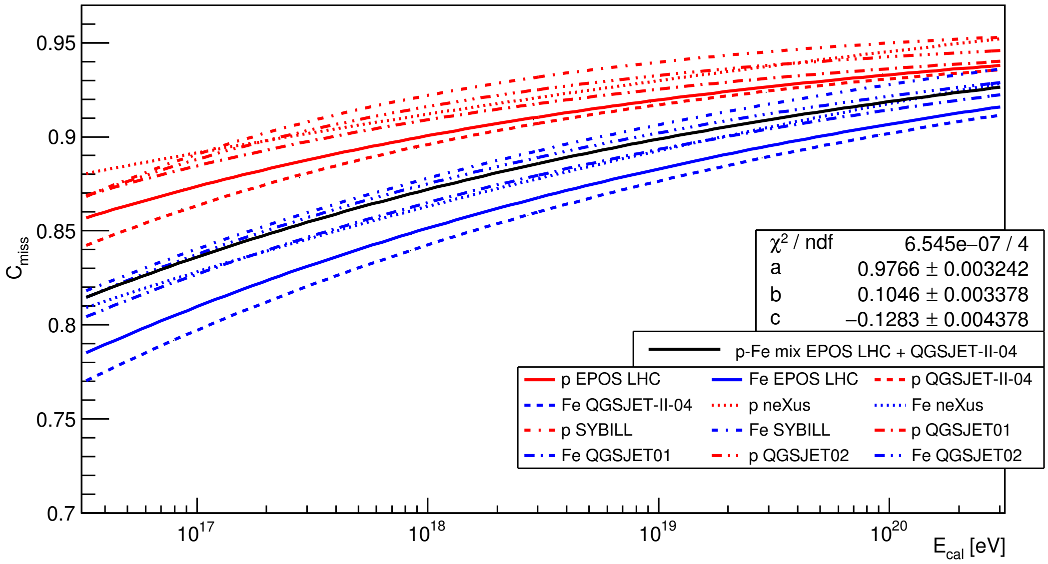

Figure 3.3: Parametrization curves of C_{miss} as functions of E_{cal} predicted by different hadronic interaction models.

The parametrization C_{miss} was estimated by fitting Eq. (3.7) to simulated data. The results for the parametrization constants a, b and c are listed in Tab. 3.1 together with results from [26] utilizing older hadronic interaction models. Parametrization curves as functions of E_{cal} for different interaction models are compared in Fig. 3.3. All interaction models predict similar behavior of C_{miss} with increasing E_{cal}. The smallest C_{miss} values (i.e. the largest E_{inv} portion) for all E_{cal} are predicted by QGSJET-II-04 and then by EPOS LHC, whereas the largest C_{miss} values are predicted by SYBILL.

Final set of universal parameters a, b and c used onwards (in the average shower energy reconstruction) is estimated by fitting the data bins for mixture of both EPOS LHC and QGSJET-II-04 and also for both proton-induced and iron-induced showers. This universal parametrization reflects the fact that we cannot know from measured data which of the most recent models of hadronic interactions describes the real processes better. Such computed results are shown in Tab. 3.2 and displayed in Fig. 3.3 as the black line.

Table 3.1: Values of the C_{miss} parametrization constants for different hadronic interaction models. The quoted errors for EPOS LHC and QGSJET-II-04 come from the fitting procedures. Results of this thesis are in bold, other are taken from [26].

	protons		
	a	b	c
EPOS LHC	$\mathbf{0.965 \pm 0.004}$	$\mathbf{0.064 \pm 0.005}$	$\mathbf{-0.152 \pm 0.011}$
QGSJET-II-04	$\mathbf{0.980 \pm 0.003}$	$\mathbf{0.128 \pm 0.004}$	$\mathbf{-0.122 \pm 0.004}$
neXus	1.046	0.134	-0.062
SYBILL	0.963	0.041	-0.246
QGSJET01	0.958	0.049	-0.176
QGSJET02	0.957	0.041	-0.226

	iron nuclei		
	a	b	c
EPOS LHC	$\mathbf{0.956 \pm 0.004}$	$\mathbf{0.060 \pm 0.004}$	$\mathbf{-0.187 \pm 0.012}$
QGSJET-II-04	$\mathbf{0.977 \pm 0.003}$	$\mathbf{0.134 \pm 0.003}$	$\mathbf{-0.126 \pm 0.003}$
neXus	1.059	0.196	-0.071
SYBILL	0.993	0.115	-0.123
QGSJET01	0.975	0.110	-0.129
QGSJET02	0.972	0.097	-0.142

Table 3.2: Final values of the universal parameters a, b and c. Values in bold are results of this work with errors estimated from the fitting, whereas the others are showed for comparison.

	a	b	c
Thesis	$\mathbf{0.977 \pm 0.003}$	$\mathbf{0.105 \pm 0.003}$	$\mathbf{-0.128 \pm 0.004}$
GAP [26]	0.978	0.085	-0.135
Article [12]	0.967	0.078	-0.140

3.1.2 Muon number parametrization

While the average C_{miss} method is easy to implement, it brings in a large systematic uncertainties originating in different results of different hadronic interaction models used and different primary particle type a priory unknown from measurements. A different event-by-event approach can be employed using information from a particular shower to estimate its invisible energy.

The method utilizing number of muons in a shower that are reaching the ground was proposed in [25]. Muons created during shower propagation constitute the major part of shower particles ionizing the atmosphere minimally thus a direct link between the shower invisible energy E_{inv} and the number of muons reaching Earth's ground N_μ is expected. Simulated showers in CONEX were evaluated to obtain the plot in Fig 3.4 showing logarithm of E_{inv} as a function of logarithm of respective shower's N_μ. The plot indicates that independently of the used hadronic interaction model, primary particle type and energy, the logarithm of invisible energy corresponds to logarithm of muon number with linear dependence. A linear fit describes the data well with with the result

$$\log(\frac{E_{inv}}{\mathrm{eV}}) = a.\log(N_\mu) + b \tag{3.8}$$

$$a = 0.9657 \pm 0.0007 \tag{3.9}$$

$$b = 10.820 \pm 0.005. \tag{3.10}$$

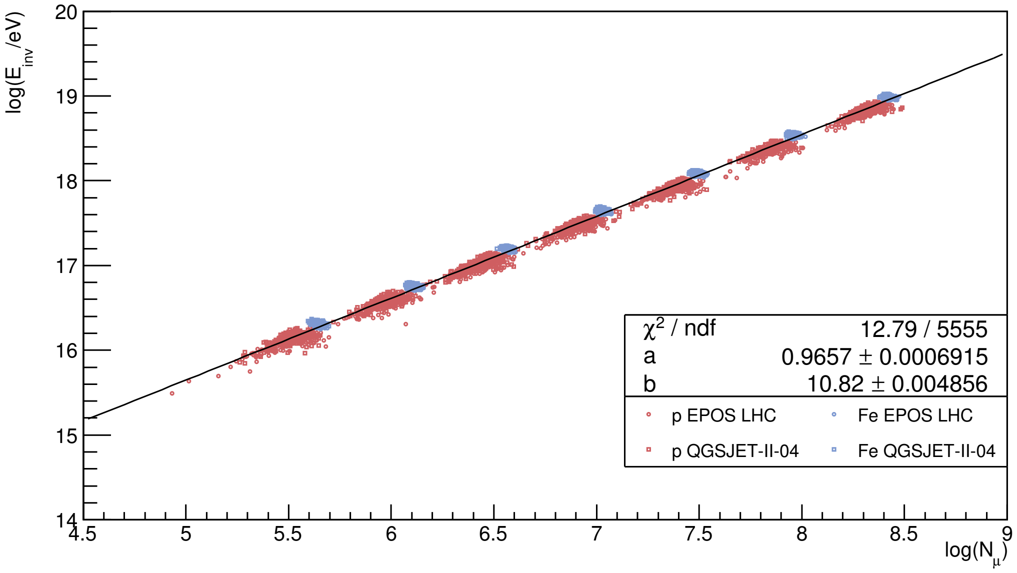

Figure 3.4: A fitted graph showing relation between logarithm of missing energy of a shower and logarithm of the shower muon count independently of the two hadronic interaction models used. Seven data groups are clearly visible corresponding from left to right to the simulated primary energies - $\log(E_0/\mathrm{eV})$ - 17, 17.5, 18, 18.5, 19, 19.5, 20.

Hence, the shower invisible energy can be estimated solely from measured shower muons reaching the ground using the relation (3.8). This reconstruction method of E_{inv} is completely independent of the shower calorimetric energy and it is estimated without dependence on the type of simulated shower primary particle or used interaction model. Thus the precision of muon reconstruction method will be significantly better than the C_{miss} method as can be seen in the comparison of relative energy reconstruction errors between the C_{miss} method and the muon number method as shown in Fig. 3.5.

Naturally, taking the final parameters of the C_{miss} parametrization as an even mixture of simulated proton and iron nucleus primaries results into the fact, that reconstructed shower invisible energy would be overestimated for lighter primary particles resp. underestimated for heavier primaries relatively to the average between proton and iron mass number. On the contrary, the muon reconstruction method utilizing event-by-event correction lowers the distance between means of proton and iron histograms in Fig. 3.5 from approximatively 5.7 % to 1.5 %. Overall, a decrease of the standard deviation from 3.1 % to 1.2 % can be seen for the histogram mixing two primary particles.

This application of muon reconstruction method to simulated cosmic-ray data clearly shows the advantages over the average C_{miss} method. These improvements have served us as a motivation for implementation of similar approach at the PAO. On one hand, measurement of the real number of muons in a cosmic-ray shower at the PAO is not sufficiently precise. On the other hand, the SD signal is sensitive to both electromagnetic and muon component and it can be used for parametrization of the invisible energy in the similar event-by-event method as shown in the following section.

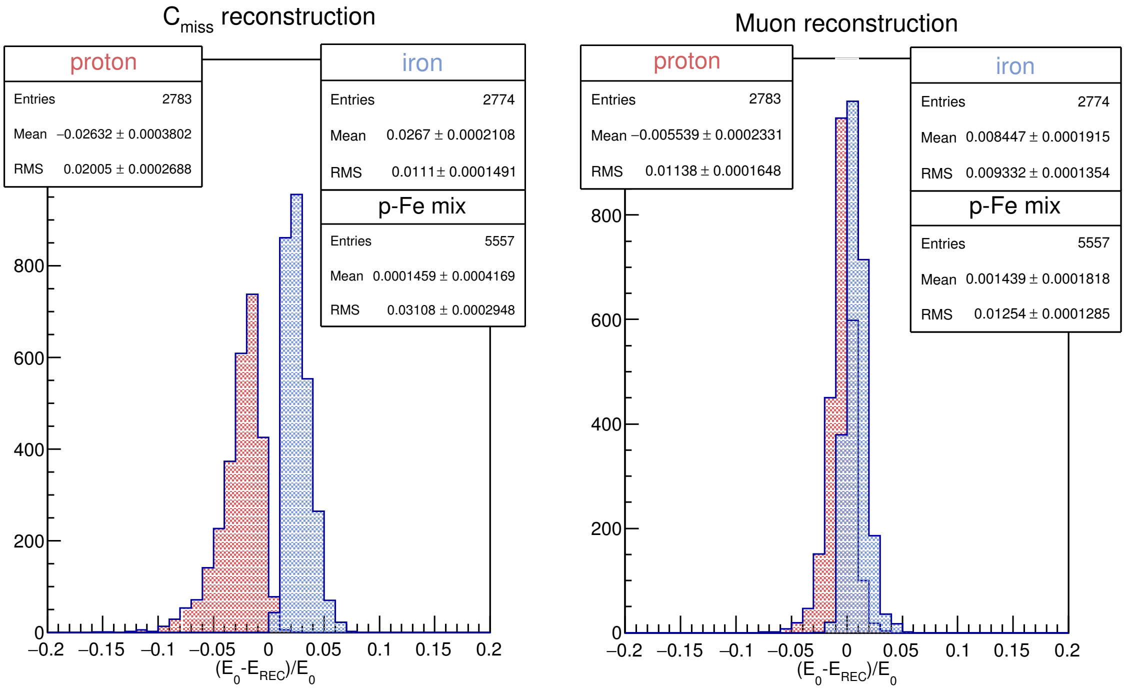

Figure 3.5: Comparison of the relative difference between reconstructed E_{REC} and simulated E_0 shower primary energies. All simulated showers by both interaction models were reconstructed by the C_{miss} (left) and the muon number method (right). The muon number reconstruction method shows nearly three times narrower distribution of $(E_0 - E_{REC})/E_0$.

3.2 Invisible energy estimation using CORSIKA

A possible parametrization of the invisible energy by a measurable parameter at the PAO directly connected to shower muon content was investigated using Hybrid Offline simulations of CORSIKA shower files from the data library of the Naples Auger Group. The library contains simulated CORSIKA shower data reconstructed by Offline software framework v2r9p5 utilized at the PAO [11]. Hadronic interaction models EPOS LHC and QGSJET-II-04 were taken in the analysis with three types of primary particle - protons, helium and iron nuclei. Continuous spectrum of primary energy from 10^{18} eV to 10^{20} eV and zenith angles from 0° to 65° were used.

Fiducial cuts that ensure same selection efficiencies for different primary particle types were applied to obtain the best reconstructed data from both FD and SD. Only T5Trigger events with minimum of 5 working SD stations around the central one with the maximal signal were taken for further study. Also no events with SD signal saturation near the shower core were included. For the FD events the selection method described in [4] was used to take only events with sufficiently good X_{max} reconstruction in the field-of-view of respective FD station. For events detected by multiple FD telescopes, the weighted mean of measured E_{cal} and X_{max} is taken for further analysis. Overall, 200779 events satisfied the cuts and were analyzed.

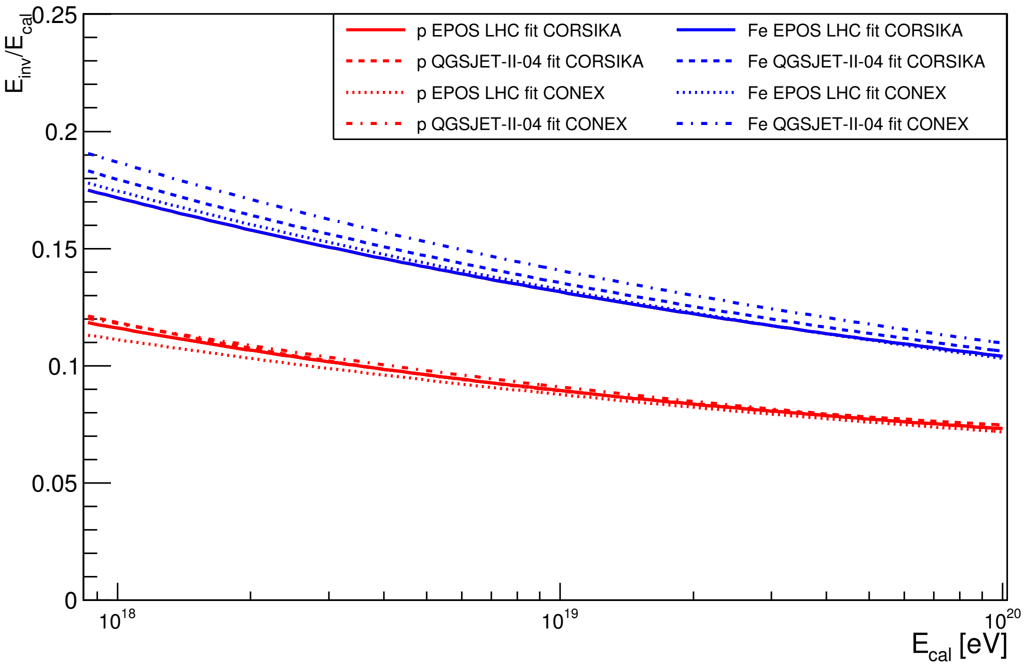

Figure 3.6: The behavior of E_{inv}/E_{cal} ratio as a function of E_{cal} for different particle types and hadronic interaction models calculated from CORSIKA simulations for $\theta \in \langle 58°, 62° \rangle$ and compared to CONEX results in corresponding E_{cal} region.

An average estimation of $\langle E_{inv} \rangle / \langle E_{cal} \rangle$ was done similarly to the process related to CONEX data, however, CORSIKA files already store the information about the calorimetric energy carried by a shower, therefore no fitting procedure had to be used. The invisible energy portion was estimated for showers in zenith bin $\langle 58^\circ, 62^\circ\rangle$ for comparison with CONEX data where we imposed all showers to impact at 60° zenith angle. The result is shown in Fig. 3.6 and it shows comparable E_{inv}/E_{cal} ratio with CONEX results for proton primaries with 0.5 % difference at maximum and decreasing with E_{cal}. Results for iron primaries shows larger discrepancies between the two MC codes mainly for the QGSJET-II-04 prediction with maximally 1 % difference that falls to 0.5 % at $E_{cal} = 10^{20}$ eV.

The differences between CONEX and CORSIKA results can be caused by different approaches of the invisible energy estimation. The CONEX approach used fitting procedure on longitudinal energy deposit profiles (as it is done at the PAO) while the CORSIKA calculates calorimetric deposits step-by-step in the atmosphere. A clear explanation of the small differences is subject to current research of the author and the reconstruction teams at the PAO and it was not possible to be obtained before the submission of the thesis.

3.2.1 $S(1000)$ parametrization using zenith angle

A similar way to parametrize E_{inv} as described in Sec. 3.1.2 is possible by utilizing the SD reconstructed signal $S(1000)$. The SD stations are sensitive to both electromagnetic and muon component of a cosmic-ray shower, therefore we can state

$$S(1000) = S_{el}(1000) + S_{\mu}(1000). \tag{3.11}$$

The $S_{\mu}(1000)$ part of the signal is proportional to the invisible energy of the shower, hence an approximatively linear dependence between logarithms of E_{inv} and $S(1000)$ is expected independently of the primary particle type, energy and hadronic interaction model. However, the electromagnetic component is being quickly absorbed in the atmosphere so in a first approximation, a substantial dependence of this relation on the zenith angle of studied showers is expected. This can be seen in Fig. 3.7 where the relation between these logarithms is plotted for four narrow bins in shower zenith angle θ_1, θ_2, θ_3 and θ_4. The invisible energy is taken from CORSIKA simulations with 1% relative error for all events, S(1000) signal is taken from Offline reconstruction of the respective shower with error estimated from LDF fit. All three primary particles and both interaction models were used covering the whole primary energy region 10^{18} eV $-$ 10^{20} eV.

The plots were fitted by simple linear approximation in $\log(S(1000)/\mathrm{VEM})$:

$$\log(\tfrac{E_{inv}}{\mathrm{eV}}) = B_{\theta} \log(\tfrac{S(1000)}{\mathrm{VEM}}) + A_{\theta}. \tag{3.12}$$

Resulting χ^2/Ndf of the fits listed in the statistical boxes on the left part of Fig. 3.7 indicates that binning in zenith angle poorly corresponds with the expected linear dependence between the two quantities (E_{inv}, $S(1000)$) in logarithm. Nevertheless, the

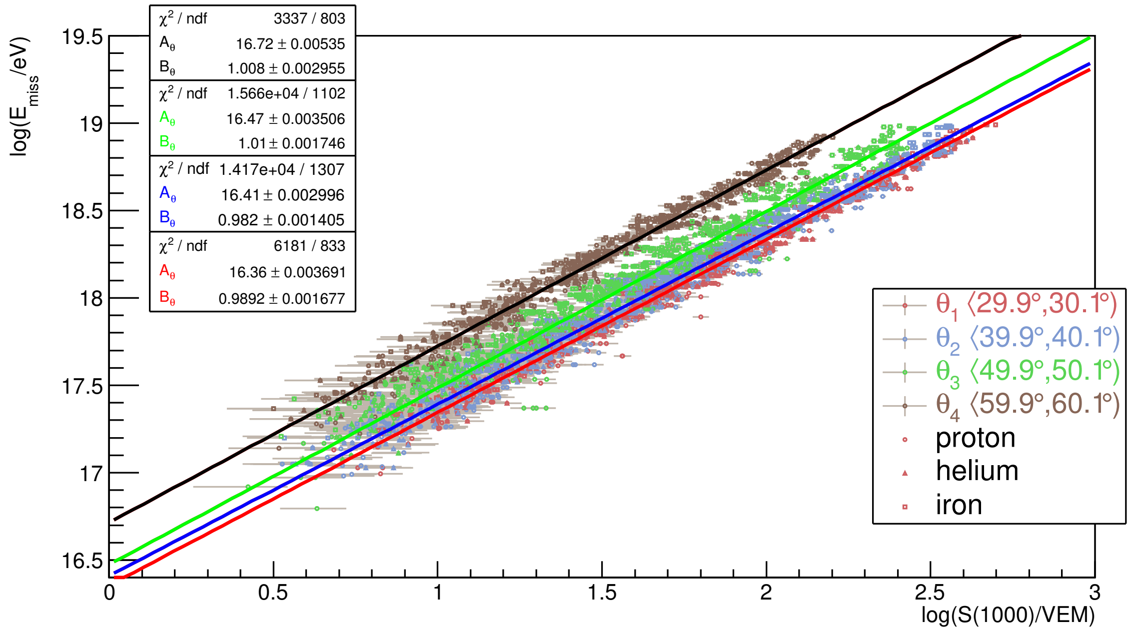

Figure 3.7: Plots of logarithm E_{inv} respective to logarithm of $S(1000)$ for four different zenith angle bins θ_1, θ_2, θ_3 and θ_4 show approximatively linear dependence of the two quantities irrespectively to primary particle type and energy or used interaction model. Four plots are fitted according to (3.12) with results displayed in corresponding colors.

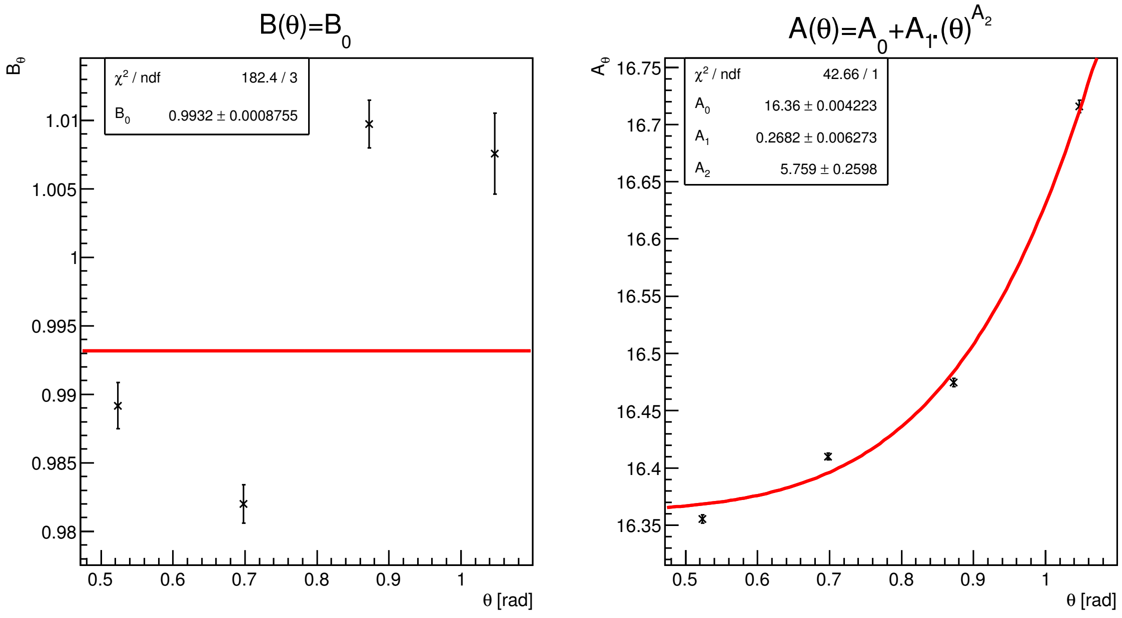

Figure 3.8: Parameters A_θ and B_θ as estimated in four linear fits (3.13) for different zenith angle bins with errors estimated from the fits. The parameters are fitted with power function and constant function respectively. Results of the fits are showed and used in the E_{inv} estimation using Eq. (3.13).

fitted parameter A_θ was considered as a power function of zenith angle and the four different values for respective theta bins were fitted as can be seen in Fig. 3.8(right). The B_θ parameter was considered as a constant function in zenith angle and fitted in Fig. 3.8(left). With both parameters expressed as functions of θ it is possible to calculate the invisible energy event-by-event with the knowledge of shower $S(1000)$ and zenith angle directly from Eq. (3.12) as

$$\tfrac{E_{inv}}{\text{eV}} = (\tfrac{S(1000)}{\text{VEM}})^{B(\theta)} 10^{A(\theta)}. \tag{3.13}$$

However, this E_{inv} parametrization in θ bins is not the best one as can be seen in the $A(\theta)$ and $B(\theta)$ estimation by fits in Fig. 3.8. A better method combining information about the shower X_{max} position and zenith angle is described in the following section.

3.2.2 $S(1000)$ parametrization using DX

If we use the semi-empirical results of the Heitler-Matthews cosmic-ray air shower model described in Sec. 1.5.2 and approximate that the invisible energy originates mainly from muons present at the depth of shower maximum we can write

$$E_{inv} = N_\mu \xi_c^\pi = \xi_c^\pi \beta_0 \left(\frac{E_0}{\xi_c^\pi}\right)^\beta, \tag{3.14}$$

where we used the relation (3.4) for expressing the number of muons at the maximum with the shower primary energy E_0 and critical energy of charged pions ξ_c^π. Parameters β and β_0 depend on pion multiplicity, interactions inelasticity and energy distribution between decay products. This is a simplification as we neglect muons originating from kaon decays and assume that all of charged pion critical energy ξ_c^π goes to the invisible energy part of a shower. It is possible to express the E_0 with the SD signal $S(1000)$ by power function

$$E_0 = \gamma_0(DX)[S(1000)]^{\gamma(DX)}, \tag{3.15}$$

where $\gamma_0(DX)$, $\gamma(DX)$ are parameters representing the stage of shower development at the time of reaching the SD stations. Both parameters are taken as function of the slant depth between the shower maximum and the ground called DX. For a shower reaching the PAO[1] it can be calculated as

$$\frac{DX}{\text{g.cm}^{-2}} = \frac{880}{\cos\theta} - \frac{X_{max}}{\text{g.cm}^{-2}}. \tag{3.16}$$

Combination of Eq. (3.14) and Eq. (3.15) results in the relation between E_{inv} and $S(1000)$

$$E_{inv} = \beta_0 \xi_c^\pi \left(\frac{\gamma_0(DX)[S(1000)]^{\gamma(DX)}}{\xi_c^\pi}\right)^\beta. \tag{3.17}$$

---

[1] Vertical atmospheric depth above the PAO is approximatively 880 g.cm^{-2}.

By taking a logarithm of the Eq. (3.17), we obtain the linear dependence similar to the one assumed heuristically in Eq. (3.12):

$$\log(\tfrac{E_{inv}}{\text{eV}}) = B(DX)\log(\tfrac{S(1000)}{\text{VEM}}) + A(DX) \tag{3.18a}$$

$$A(DX) = (1-\beta)\log(\xi_c^{\pi}) + \log(\beta_0) + \beta\log(\gamma_0(DX)) \tag{3.18b}$$

$$B(DX) = \beta\,\gamma(DX). \tag{3.18c}$$

Another supporting argument for the linear relation in Eq. (3.18a) follows from simple assumption about universality of electromagnetic part of the shower signal (3.11). As shown in several papers [22], [21], for a given distance DX between the ground and the shower maximum the electromagnetic size of signal $S_{el}(1000)$ is largely independent on the primary particle type and even on interaction model. Therefore, if the data are grouped in DX bins, the differences in $S(1000)$ account for different size of the muon signal.

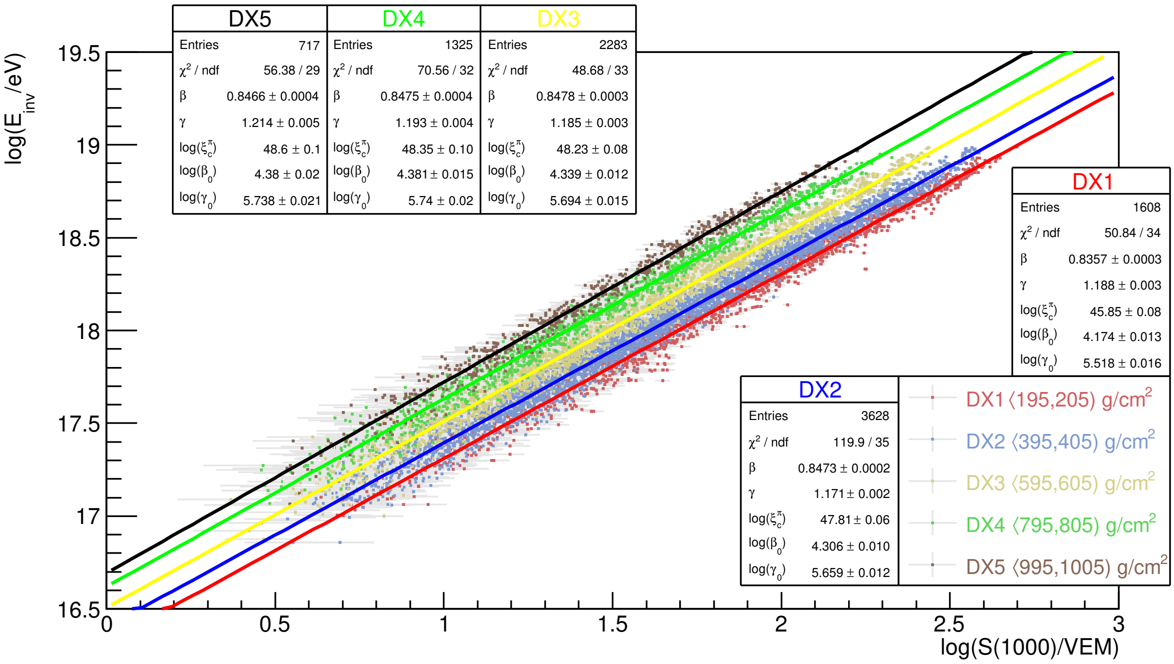

Figure 3.9: Plots of logarithm of E_{inv} respective to logarithm of $S(1000)$ for five bins in DX. Different primary particle types, energies and interaction models are not distinguished in the plot. Data are fitted by a five-parameter fit according to (3.18a), (3.18b) and (3.18c).

The linear dependence in (3.18a) was studied in 5 bins of DX by evaluating showers induced by one of three primary particles in the whole energy range and utilizing both interaction models. The results of fits are shown in Fig. 3.9 and they indicate a much better linear fit parametrization using bins in DX in comparison to bins in θ. The parameters $A(DX)$ and $B(DX)$ are expressed with linear resp. exponential dependence on DX as can be seen in Fig. 3.12 and they can then be used in event-by-event E_{inv}

calculation from the knowledge of the $S(1000)$ and DX of a particular shower by

$$\frac{E_{inv}}{\mathrm{eV}} = \left(\frac{S(1000)}{\mathrm{VEM}}\right)^{B(DX)} 10^{A(DX)}. \tag{3.19}$$

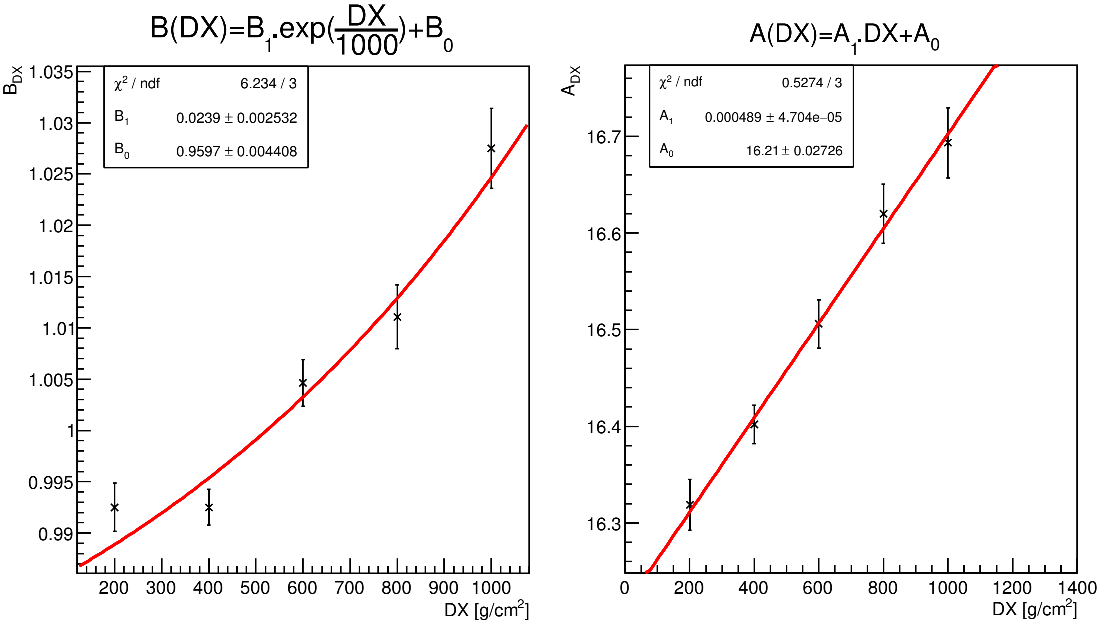

Figure 3.10: Parameters $A(DX)$ and $B(DX)$ as estimated in five linear fits in Fig. 3.9 for five different DX bins with errors estimated from the fits. The parameters are fitted with linear function and exponential respectively. Results of the fits are showed and used in the E_{inv} estimation using Eq. (3.19).

3.2.3 $S_\mu(1000)$ parametrization

Another possible method was tested for lower energy regions ($10^{18} - 10^{19}$ eV) of analyzed showers simulated in CORSIKA. The method attempts to parametrize the E_{inv} directly by muon fraction of $S(1000)$ signal - $S_\mu(1000)$. From simulations one can quantify the amount of the SD station signal that was induced by muon component and the other part induced by electromagnetic component. By analyzing the ratio of the muon induced signal to the whole SD signal at the 1000 m distance from the shower core a quantity f_μ called muon fraction in 1000 m is obtained. Value of f_μ is accessible only from simulations. Currently for the data measured at the PAO it is of course not known which part of $S(1000)$ corresponds to muon induced signal. However, with the AugerPrime upgrade of the observatory it will be possible to calculate $S_\mu(1000)$ from comparison of the signal in the SD tank and the signal in scintillators. The part of $S(1000)$ signal corresponding to muons can be expressed as

$$S_\mu(1000) = f_\mu\, S(1000). \tag{3.20}$$

The parametrization was done similarly to the process described in Sec. 3.16 and the relation between logarithms of E_{inv} and $S_\mu(1000)$ was studied for the same five bins in DX. The plots were fitted by the linear dependence

$$\log(\frac{E_{inv}}{\mathrm{eV}}) = B_\mu(DX)\log(\frac{f_\mu\, S(1000)}{\mathrm{VEM}}) + A_\mu(DX) \tag{3.21}$$

as a two parameter fit in $A_\mu(DX)$ and $B_\mu(DX)$. The fit results are in Fig. 3.11 and they show that the parametrization using $S_\mu(1000)$ is not as clearly dependent on DX as in the previous parametrization using $S(1000)$. Nevertheless, the fitted parameters $A_\mu(DX)$ and $B_\mu(DX)$ were expressed as exponential function in DX in Fig. 3.12 and they can be used for the invisible energy calculation using equation

$$\frac{E_{inv}}{\mathrm{eV}} = (\frac{f\mu\, S(1000)}{\mathrm{VEM}})^{B_\mu(DX)} 10^{A_\mu(DX)}, \tag{3.22}$$

provided that the shower muon fraction in 1000 m is known.

As mentioned before, the method is currently not applicable directly to the data measured at the PAO but it can be compared with the other methods using simulations and used later in modified way for data of the upgraded observatory.

3.3 Application to simulated data

The previously established methods for calculating the invisible energy were compared all together on reconstructed events of CORSIKA simulations at the PAO. Calorimetric energy E_{cal} measured by the FD telescopes was corrected by four methods:

- The average C_{miss} method utilizing Eq. (3.6), taking only E_{cal} information from every shower.
- The $S(1000)$ θ method using Eq. (3.13), taking the information about $S(1000)$ signal and shower zenith angle θ.
- The $S(1000)$ DX method taking $S(1000)$, θ and also X_{max} information to event-by-event estimation of E_{inv} from Eq. (3.19).
- The $S_\mu(1000)$ DX method taking all of previous method inputs, but multiplying the $S(1000)$ by the muon fraction in 1000 m.

Comparison of the reconstruction quality expressed as relative difference of reconstructed and simulated energies $(E_0 - E_{REC})/E_0$ of the first three methods are depicted in Fig. 4.26. This figure compares the p/Fe biases between the reconstructed energy and the primary energy for each shower generated by either EPOS LHC or QGSJET-II-04. Only showers with $S(1000) > 10$ VEM and $DX > 10$ g.cm^{-2} were taken for reconstruction.

The results show considerably smaller mean reconstruction difference for the $S(1000)$ methods compared to the average C_{miss} method. The overall standard devia-

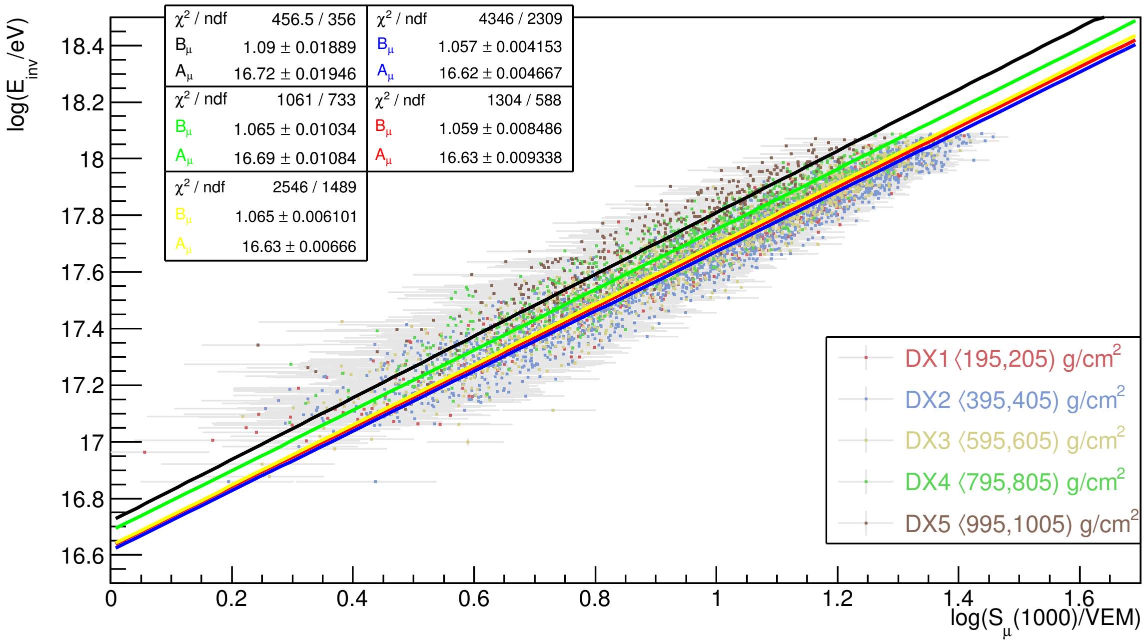

Figure 3.11: Plots of logarithm of E_{inv} respective to logarithm of $S_\mu(1000)$ for five bins in DX. Different primary particle types, energies and interaction models are not distinguished in the plot. Data are fitted by a two-parameter fit according to (3.21) and fit results are shown in boxes colored respectively to the fit functions.

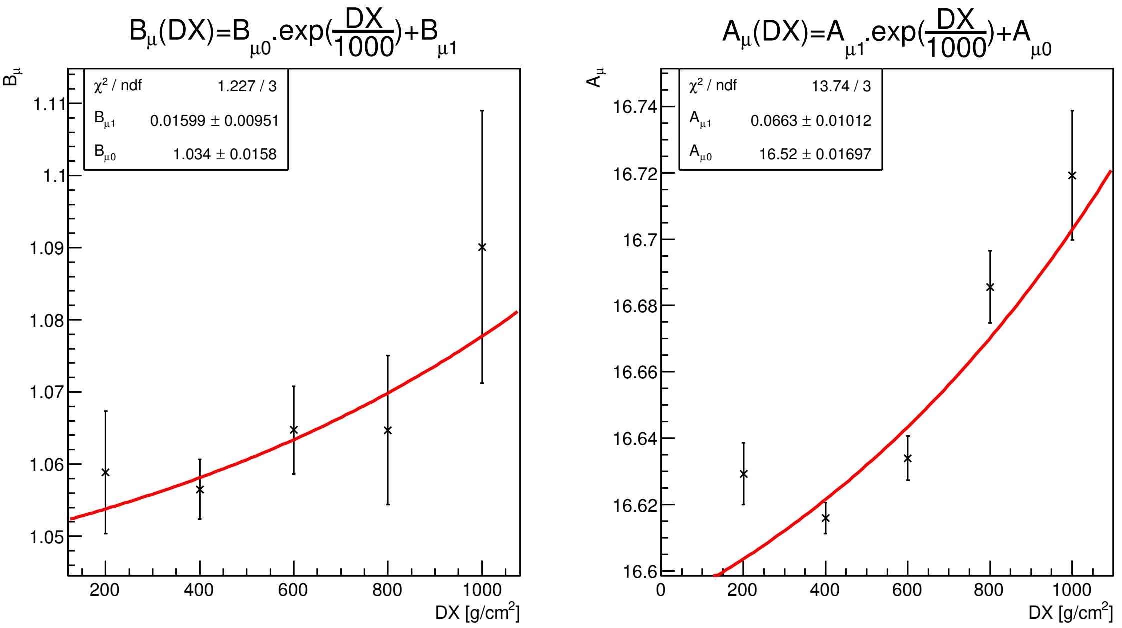

Figure 3.12: Parameters $A_\mu(DX)$ and $B_\mu(DX)$ as estimated in five linear fits in Fig. 3.11 for five different DX bins with errors estimated from the fits. The parameters are fitted with linear function and exponential respectively. Results of the fits are showed and used in the E_{inv} estimation using Eq. (3.19).

tion of $(E_0 - E_{REC})/E_0$ decreased by almost 1 % and the distance between means of proton and iron histograms diminished by 2 %. Comparison of reconstruction methods for specific energy regions is showed in Tab. 3.3 for both interaction models. In all energy ranges a better reconstruction is achieved using $S(1000)$ methods. The largest improvement of reconstruction is in the lowest primary energy region $10^{18} - 10^{18.5}$ eV where the standard deviation of $(E_0 - E_{REC})/E_0$ decreased by almost 1.1 % and the p-Fe separation decreased by 3.3 %.

When utilizing the $S_\mu(1000)\ DX$ method on the available energy range $10^{18} - 10^{19}$ eV with the f_μ fraction known, histograms of reconstruction error are shown in Fig. 4.27 with comparison to the C_{miss} method in the same energy range. The $S_\mu(1000)\ DX$ method appears to be significantly better than the average correction and also slightly better when compared to the $S(1000)$ DX method at the low energy range $10^{18} - 10^{18.5}$ eV as can be seen in Tab. 3.3. Despite the promising results of the $S_\mu(1000)\ DX$, it is not possible to use it on real data as the muon fraction in 1000 m is not known from measurements at the moment.

More tables comparing the four reconstruction methods at given energy ranges for showers generated only by EPOS LHC resp. by QGSJET-II-04 are in Tab. 3.4 resp. Tab. 3.5. This comparison was done in order to see the impact of the different reconstruction methods for the cases when we assume that the nature behaves as described by EPOS LHC or by QGSJET-II-04.

From all three tables (3.3 - 3.5) the one describing only the results for the showers generated by EPOS LHC is showing the best improvements. A comparative histograms of relative differences of reconstructed and primary energies for all E_{inv} estimation methods used on different sets of simulated data in different energy ranges are located in Appendix.

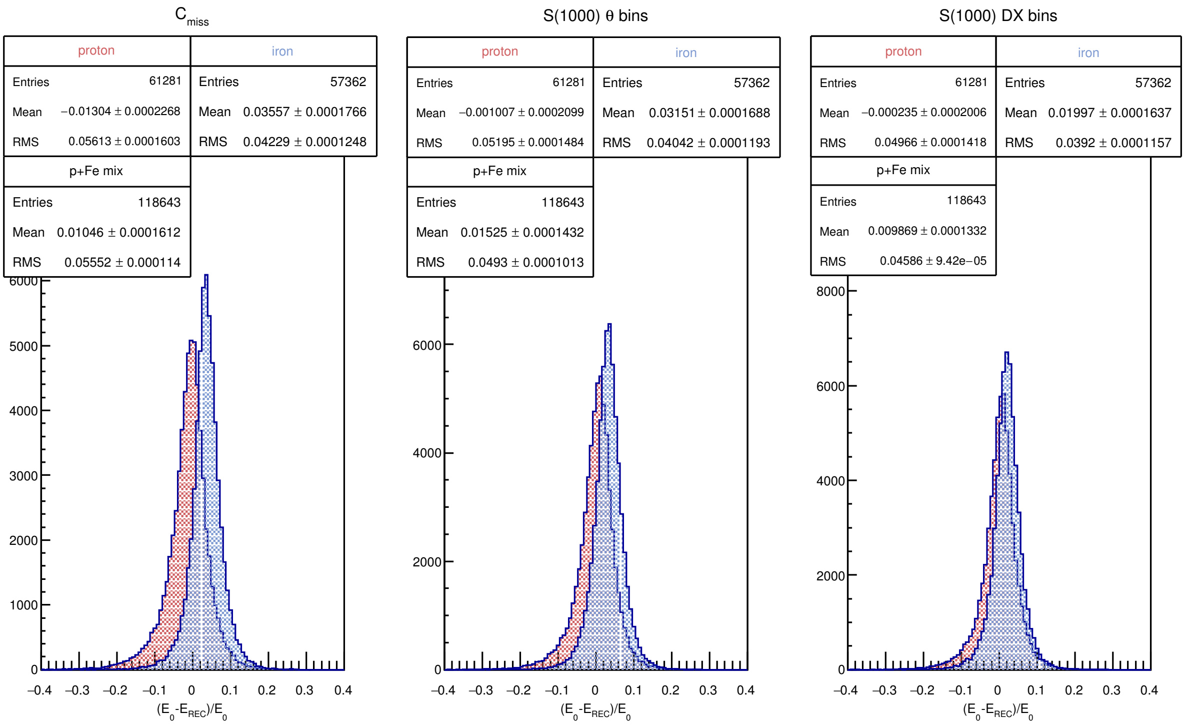

Figure 3.13: Histograms of relative reconstructed energy difference to the primary energy for three different methods used - C_{miss}, $S(1000)\ \theta$ and $S(1000)\ DX$ - for the primary energy range $10^{18} - 10^{20}$ eV. Both **EPOS LHC** and **QGSJET-II-04** model simulated showers are reconstructed. The histograms for iron-induced showers were scaled to have the same integral area as the proton-induced histograms.

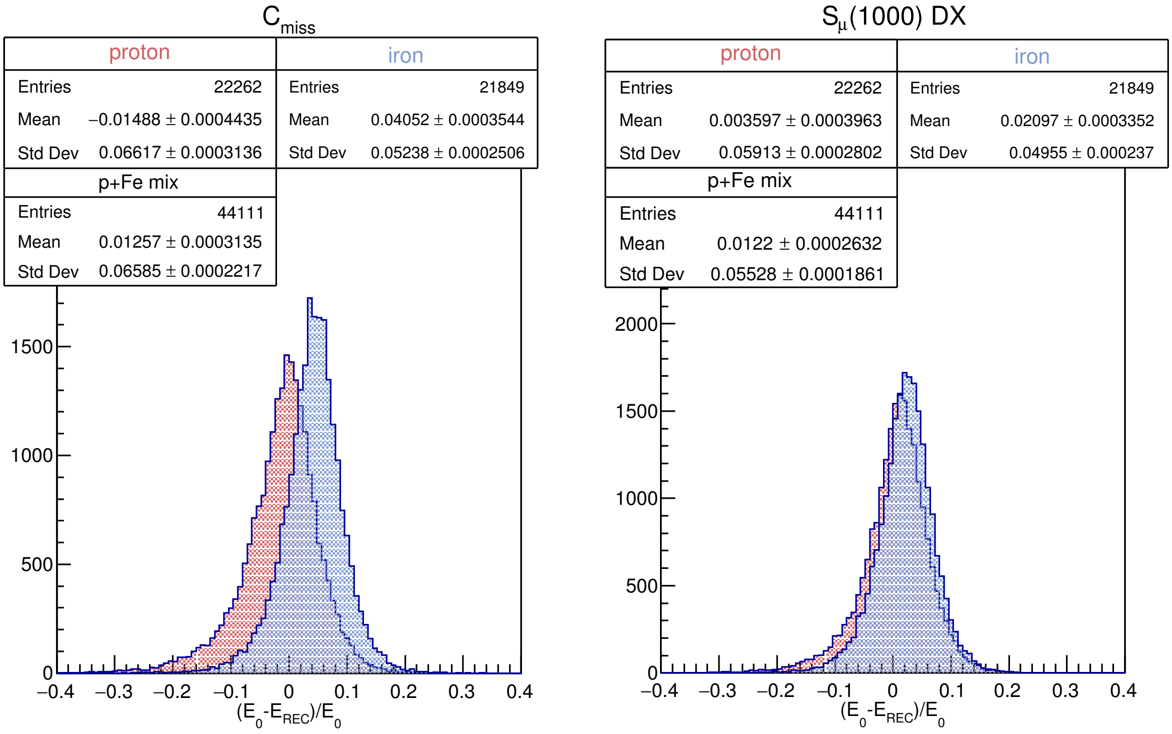

Figure 3.14: Histograms of relative reconstructed energy difference to the primary energy for two methods used - C_{miss} and $S_{\mu}(1000)\ DX$ - for the primary energy range $10^{18} - 10^{19}$ eV. Both **EPOS LHC** and **QGSJET-II-04** simulated showers are reconstructed. The histograms for iron-induced showers were scaled to have the same integral area as the proton-induced histograms.

Table 3.3: Tables comparing the four reconstruction methods - C_{miss}, $S(1000)\ \theta$, $S(1000)\ DX$ and $S_{\mu}(1000)\ DX$ - by total error mean, standard deviation and distance between error histograms for proton-induced and iron-induced showers. Four tables for different primary energy ranges E_0 are showed. Both **EPOS LHC** and **QGSJET-II-04** model simulated showers are reconstructed.

$\log(E_0/\text{eV})$: $18 - 18.5$	$\langle \frac{E_0-E_{rec}}{E_0} \rangle$	$\sigma\left(\frac{E_0-E_{rec}}{E_0}\right)$	$\lvert\langle \frac{E_0-E_{rec}}{E_0} \rangle_p$ - $\langle \frac{E_0-E_{rec}}{E_0} \rangle_{Fe}\rvert$
C_{miss}	0.014 ± 0.001	0.0752 ± 0.0007	0.061 ± 0.003
$S(1000)\ \theta$	0.0123 ± 0.0009	0.0664 ± 0.0006	0.044 ± 0.002
$S(1000)$ DX	0.0064 ± 0.0009	0.0636 ± 0.0006	0.028 ± 0.002
$S_{\mu}(1000)$ DX	0.0125 ± 0.0008	0.0631 ± 0.0006	0.019 ± 0.002

$\log(E_0/\text{eV})$: $18.5 - 19$	$\langle \frac{E_0-E_{rec}}{E_0} \rangle$	$\sigma\left(\frac{E_0-E_{rec}}{E_0}\right)$	$\lvert\langle \frac{E_0-E_{rec}}{E_0} \rangle_p$ - $\langle \frac{E_0-E_{rec}}{E_0} \rangle_{Fe}\rvert$
C_{miss}	0.0126 ± 0.0003	0.0643 ± 0.0002	0.0545 ± 0.0008
$S(1000)\ \theta$	0.0184 ± 0.0003	0.0571 ± 0.0002	0.0368 ± 0.0008
$S(1000)$ DX	0.0110 ± 0.0003	0.0538 ± 0.0002	0.0236 ± 0.0008
$S_{\mu}(1000)$ DX	0.0122 ± 0.0003	0.0540 ± 0.0002	0.0172 ± 0.0008

$\log(E_0/\text{eV})$: $19 - 19.5$	$\langle \frac{E_0-E_{rec}}{E_0} \rangle$	$\sigma\left(\frac{E_0-E_{rec}}{E_0}\right)$	$\lvert\langle \frac{E_0-E_{rec}}{E_0} \rangle_p$ - $\langle \frac{E_0-E_{rec}}{E_0} \rangle_{Fe}\rvert$
C_{miss}	0.0115 ± 0.0002	0.0506 ± 0.0002	0.0479 ± 0.0006
$S(1000)\ \theta$	0.0161 ± 0.0002	0.0449 ± 0.0001	0.0315 ± 0.0006
$S(1000)$ DX	0.0111 ± 0.0002	0.0412 ± 0.0001	0.0196 ± 0.0005

$\log(E_0/\text{eV})$: $19.5 - 20$	$\langle \frac{E_0-E_{rec}}{E_0} \rangle$	$\sigma\left(\frac{E_0-E_{rec}}{E_0}\right)$	$\lvert\langle \frac{E_0-E_{rec}}{E_0} \rangle_p$ - $\langle \frac{E_0-E_{rec}}{E_0} \rangle_{Fe}\rvert$
C_{miss}	0.0083 ± 0.0003	0.0437 ± 0.0002	0.0392 ± 0.0006
$S(1000)\ \theta$	0.0102 ± 0.0002	0.0397 ± 0.0002	0.0260 ± 0.0006
$S(1000)$ DX	0.0070 ± 0.0002	0.0362 ± 0.0001	0.0151 ± 0.0006

Table 3.4: Tables comparing the four reconstruction methods - C_{miss}, $S(1000)\ \theta$, $S(1000)\ DX$ and $S_\mu(1000)\ DX$ - by total error mean, standard deviation and distance between error histograms for proton-induced and iron-induced showers. Four tables for different primary energy ranges E_0 are showed. Only showers generated by **EPOS LHC** model are reconstructed.

log(E_0/eV): $18 - 18.5$	$\langle\frac{E_0-E_{rec}}{E_0}\rangle$	$\sigma\left(\frac{E_0-E_{rec}}{E_0}\right)$	$\lvert\langle\frac{E_0-E_{rec}}{E_0}\rangle_p$ - $\langle\frac{E_0-E_{rec}}{E_0}\rangle_{Fe}\rvert$
C_{miss}	0.012 ± 0.001	0.075 ± 0.001	0.059 ± 0.003
$S(1000)\ \theta$	0.006 ± 0.001	0.0655 ± 0.0008	0.042 ± 0.003
$S(1000)$ DX	0.0004 ± 0.0001	0.0627 ± 0.0008	0.025 ± 0.003
$S_\mu(1000)$ DX	0.006 ± 0.001	0.0624 ± 0.0008	0.018 ± 0.003

log(E_0/eV): $18.5 - 19$	$\langle\frac{E_0-E_{rec}}{E_0}\rangle$	$\sigma\left(\frac{E_0-E_{rec}}{E_0}\right)$	$\lvert\langle\frac{E_0-E_{rec}}{E_0}\rangle_p$ - $\langle\frac{E_0-E_{rec}}{E_0}\rangle_{Fe}\rvert$
C_{miss}	0.0114 ± 0.0005	0.0646 ± 0.0003	0.054 ± 0.001
$S(1000)\ \theta$	0.0129 ± 0.0004	0.0567 ± 0.0003	0.035 ± 0.001
$S(1000)$ DX	0.0058 ± 0.0004	0.0535 ± 0.0003	0.022 ± 0.001
$S_\mu(1000)$ DX	0.0065 ± 0.0004	0.0540 ± 0.0003	0.015 ± 0.001

log(E_0/eV): $19 - 19.5$	$\langle\frac{E_0-E_{rec}}{E_0}\rangle$	$\sigma\left(\frac{E_0-E_{rec}}{E_0}\right)$	$\lvert\langle\frac{E_0-E_{rec}}{E_0}\rangle_p$ - $\langle\frac{E_0-E_{rec}}{E_0}\rangle_{Fe}\rvert$
C_{miss}	0.0104 ± 0.0003	0.0513 ± 0.0002	0.0468 ± 0.0009
$S(1000)\ \theta$	0.0109 ± 0.0003	0.0451 ± 0.0002	0.0290 ± 0.0008
$S(1000)$ DX	0.0063 ± 0.0003	0.0414 ± 0.0002	0.0177 ± 0.0007

log(E_0/eV): $19.5 - 20$	$\langle\frac{E_0-E_{rec}}{E_0}\rangle$	$\sigma\left(\frac{E_0-E_{rec}}{E_0}\right)$	$\lvert\langle\frac{E_0-E_{rec}}{E_0}\rangle_p$ - $\langle\frac{E_0-E_{rec}}{E_0}\rangle_{Fe}\rvert$
C_{miss}	0.0073 ± 0.0004	0.0452 ± 0.0003	0.037 ± 0.001
$S(1000)\ \theta$	0.0046 ± 0.0004	0.0406 ± 0.0002	0.0227 ± 0.0009
$S(1000)$ DX	0.0023 ± 0.0003	0.0374 ± 0.0002	0.0118 ± 0.0009

Table 3.5: Tables comparing the four reconstruction methods - C_{miss}, $S(1000)\ \theta$, $S(1000)\ DX$ and $S_\mu(1000)\ DX$ - by total error mean, standard deviation and distance between error histograms for proton-induced and iron-induced showers. Four tables for different primary energy ranges E_0 are showed. Only showers simulated by **QGSJET-II-04** model are reconstructed.

$\log(E_0/\mathrm{eV})$: $18 - 18.5$	$\langle \frac{E_0 - E_{rec}}{E_0} \rangle$	$\sigma\left(\frac{E_0 - E_{rec}}{E_0}\right)$	$\lvert\langle \frac{E_0 - E_{rec}}{E_0} \rangle_p$ - $\langle \frac{E_0 - E_{rec}}{E_0} \rangle_{Fe}\rvert$
C_{miss}	0.016 ± 0.002	0.076 ± 0.001	0.064 ± 0.004
$S(1000)\ \theta$	0.020 ± 0.001	0.067 ± 0.001	0.047 ± 0.004
$S(1000)$ DX	0.014 ± 0.001	0.064 ± 0.001	0.032 ± 0.004
$S_\mu(1000)$ DX	0.021 ± 0.001	0.0630 ± 0.0009	0.022 ± 0.004

$\log(E_0/\mathrm{eV})$: $18.5 - 19$	$\langle \frac{E_0 - E_{rec}}{E_0} \rangle$	$\sigma\left(\frac{E_0 - E_{rec}}{E_0}\right)$	$\lvert\langle \frac{E_0 - E_{rec}}{E_0} \rangle_p$ - $\langle \frac{E_0 - E_{rec}}{E_0} \rangle_{Fe}\rvert$
C_{miss}	0.0140 ± 0.0005	0.0638 ± 0.0003	0.054 ± 0.001
$S(1000)\ \theta$	0.0245 ± 0.004	0.0567 ± 0.0003	0.038 ± 0.001
$S(1000)$ DX	0.0168 ± 0.0004	0.0535 ± 0.0003	0.025 ± 0.001
$S_\mu(1000)$ DX	0.0186 ± 0.004	0.0533 ± 0.0003	0.018 ± 0.001

$\log(E_0/\mathrm{eV})$: $19 - 19.5$	$\langle \frac{E_0 - E_{rec}}{E_0} \rangle$	$\sigma\left(\frac{E_0 - E_{rec}}{E_0}\right)$	$\lvert\langle \frac{E_0 - E_{rec}}{E_0} \rangle_p$ - $\langle \frac{E_0 - E_{rec}}{E_0} \rangle_{Fe}\rvert$
C_{miss}	0.0126 ± 0.0003	0.0499 ± 0.0002	0.049 ± 0.001
$S(1000)\ \theta$	0.0212 ± 0.0003	0.0442 ± 0.0002	0.034 ± 0.001
$S(1000)$ DX	0.0158 ± 0.0003	0.0405 ± 0.0002	0.022 ± 0.001

$\log(E_0/\mathrm{eV})$: $19.5 - 20$	$\langle \frac{E_0 - E_{rec}}{E_0} \rangle$	$\sigma\left(\frac{E_0 - E_{rec}}{E_0}\right)$	$\lvert\langle \frac{E_0 - E_{rec}}{E_0} \rangle_p$ - $\langle \frac{E_0 - E_{rec}}{E_0} \rangle_{Fe}\rvert$
C_{miss}	0.0090 ± 0.0003	0.0423 ± 0.0002	0.0406 ± 0.0008
$S(1000)\ \theta$	0.0147 ± 0.0003	0.0381 ± 0.0002	0.0278 ± 0.0008
$S(1000)$ DX	0.0108 ± 0.0003	0.0345 ± 0.0002	0.0170 ± 0.0007

Chapter 4

Application to real cosmic-ray data

Finally, the $S(1000)$ DX method was chosen according to its results when applied to simulated showers as the best applicable method to real cosmic-ray data measured at the PAO. Set of data obtained during the observations from December 2004 to December 2014 were taken for this analysis. The time restriction to events before 2014 is to guarantee the same reconstruction (same Offline versions) as for the simulated data library. The initial set contained about 2.6×10^6 triggered events that were subjected to both quality and fiducial cuts similar to ones in Sec. 3.2. A more detailed description of cuts is in [4]. For events being registered by more than one FD telescope, the weighted average of shower E_{cal} and X_{max} was taken as the relevant value. Only Golden events above FD energy $10^{18.3}$ eV were taken for the study - this resulted in 2944 events in total.

4.1 Invisible energy parametrization using E_{cal}

For every one of the 2944 Golden events the invisible energy E_{inv} was calculated applying the Eq. (3.19) where we utilize measured parameters - $S(1000)$, X_{max} and θ. If we plot the resulting E_{inv} to respective E_{cal} measured by the FD a power function can be expected. This comes from fact that simple parametrization of E_{inv}/E_{cal} as obtained from CONEX and CORSIKA simulations followed a power law in E_{cal} with negative exponent (see Fig. 3.6). A power law was assumed as

$$\frac{E_{inv}}{\mathrm{EeV}} = a \left(\frac{E_{cal}}{\mathrm{EeV}} \right)^b \tag{4.1}$$

and was fitted to calculated data in Fig. 4.1 with results $a = 0.1406 \pm 0.0007$, $b = 0.973 \pm 0.003$ and compared to the same parametrization done in [2] where the parameters for the same energy region were estimated as $a' = 0.1633$ and $b' = 0.9463$. Thus, the master's thesis predicts slightly steeper behavior of the absolute E_{inv} value when parametrized by the measured E_{cal} but in overall it shows slightly less invisible energy in energy range around 10^{18} eV when compared to [2]. This is presumably caused by different methods of estimating E_{inv} in the two works.

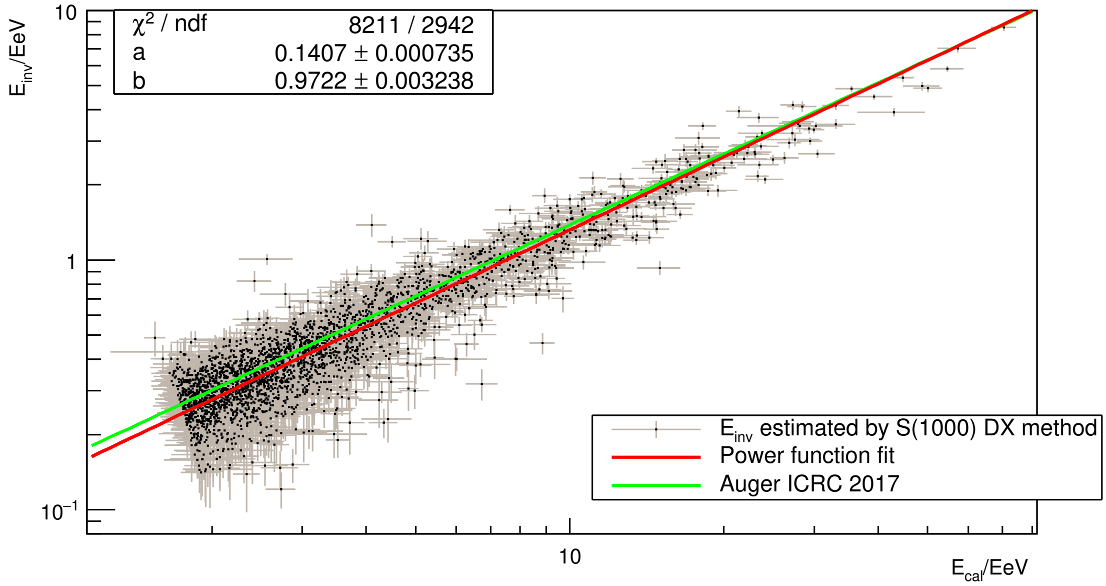

Figure 4.1: Plot of the shower invisible energy estimated by $S(1000)$ DX method versus its respective measured calorimetric energy E_{cal}. The data are fitted by the Eq. 4.1 with results of the fit showed in the left box. Fit is compared to results of the same parametrization in [2].

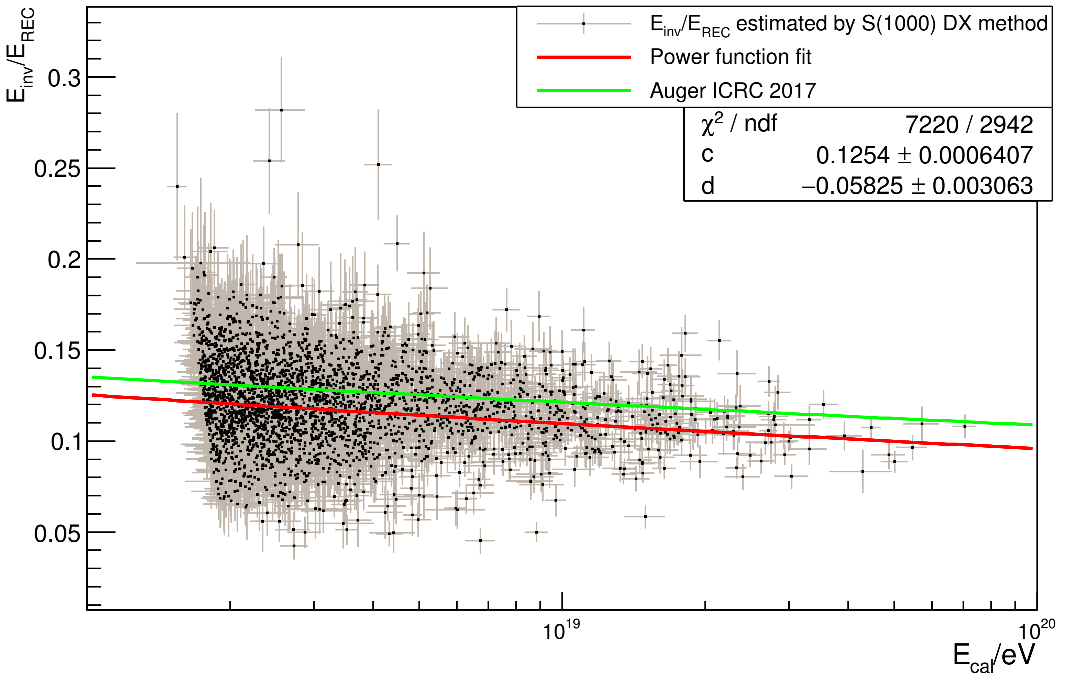

Figure 4.2: Plot of the E_{inv}/E_{REC} ratio versus its respective measured calorimetric energy E_{cal}. The data are fitted by the Eq. 4.2 with results of the fit showed in the lower box. Fit is compared to results of the same parametrization in [2].

A better comparison of the two results can be seen in Fig. 4.2 where a ratio E_{inv}/E_{REC} of the invisible to the total reconstructed energy is plotted against measured E_{cal} and fitted by a power law

$$\frac{E_{inv}}{E_{REC}} = c\left(\frac{E_{cal}}{\mathrm{EeV}}\right)^{d} \tag{4.2}$$

with the results $c = 0.1254 \pm 0.0006$ and $d = -0.058 \pm 0.003$. The difference of E_{inv}/E_{REC} in this thesis and in work [2] is around 1-1.5 % for the displayed energy range with the results of this work indicating smaller portion of the invisible energy to the total reconstructed energy at the PAO. The relation (4.1) between mean E_{inv} and E_{cal} can be used for the energy reconstruction for the non hybrid events with no SD stations triggered or to events with the $S(1000)$ signal not reconstructed.

4.1.1 Comparison of average invisible energy parametrizations

With the average invisible energy estimated from the fit of (4.1) as a function of E_{cal}, it is possible to modify the power function, so that it corresponds to the C_{miss} factor defined in Sec. 3.1.1. By simple manipulations we obtain the relation

$$C_{miss} = \frac{E_{cal}}{E_0} = \frac{E_{cal}}{E_{cal} + E_{inv}} = \left[1 + a\left(\frac{E_{cal}}{\mathrm{EeV}}\right)^{b-1}\right]^{-1}. \tag{4.3}$$

The four different C_{miss} average parametrizations are plotted in Fig. 4.3. The plot

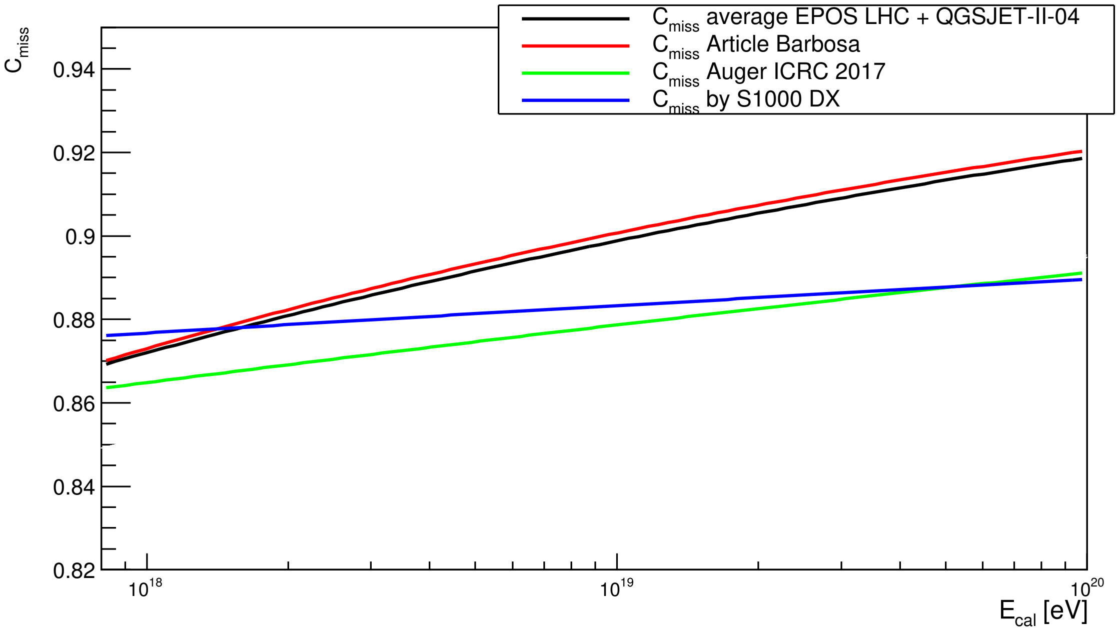

Figure 4.3: Plot of four different C_{miss} parametrization. The one obtained from CONEX simulations is represented by black line, another red one was taken from article [12]. The last two were obtained using the (4.3) for the results of [2] (green) and for the results of this thesis (blue).

indicates almost the same results of the C_{miss} calculated in this thesis as an average between results of EPOS LHC and QGSJET-II-04 and as an even mixture of proton and iron primaries and of the C_{miss} obtained in the article [12]. The other two estimations of the C_{miss} using the Eq. (4.3) indicate slower increase of C_{miss} value with E_{cal}. The C_{miss} calculated using the $S(1000)$ DX method to Auger data predicts the smallest change of E_{cal}/E_0 ratio with E_{cal} and also predicts the largest invisible energy part at the highest energies.

4.2 FD and SD reconstructed energy comparison

The new event-by-event $S(1000)$ DX method for the invisible energy estimation slightly alters the FD energy spectrum. This also changes the calibration of SD signal by the reconstructed shower energy estimated from the FD. For the new calibration by Golden events the $S(1000)$ signal was converted to the zenith independent quantity - S_{38} - using the Constant Intensity Cut function of the form (2.6a) in the formula (2.7). Obtained S_{38} signals were plotted respectively to the new reconstructed FD energies in Fig. 4.4. The data were fitted by a power law function (2.8) with the results $A = (1.90 \pm 0.02) \times 10^{17}$ eV and $B = (1.016 \pm 0.003)$.

With the new SD calibration obtained, the two methods of the invisible energy estimation can be compared also by evaluating a relative difference between the shower energy estimated by the FD and the SD. The histograms for relative E_{FD} and E_{SD} difference are shown in Fig. 4.5. The E_{SD} values for the two methods were calculated using respective SD calibration relations. It is clear from the histograms that the standard deviation of the difference was lowered significantly from 19.67 % for the standard approach to 17.29 % for the $S(1000)$ DX method. This indicates both better reconstruction of shower total energy and better calibration of the SD and it can serve as an indication of the good performance and applicability of the proposed method of the invisible energy estimation in cosmic-ray air showers.

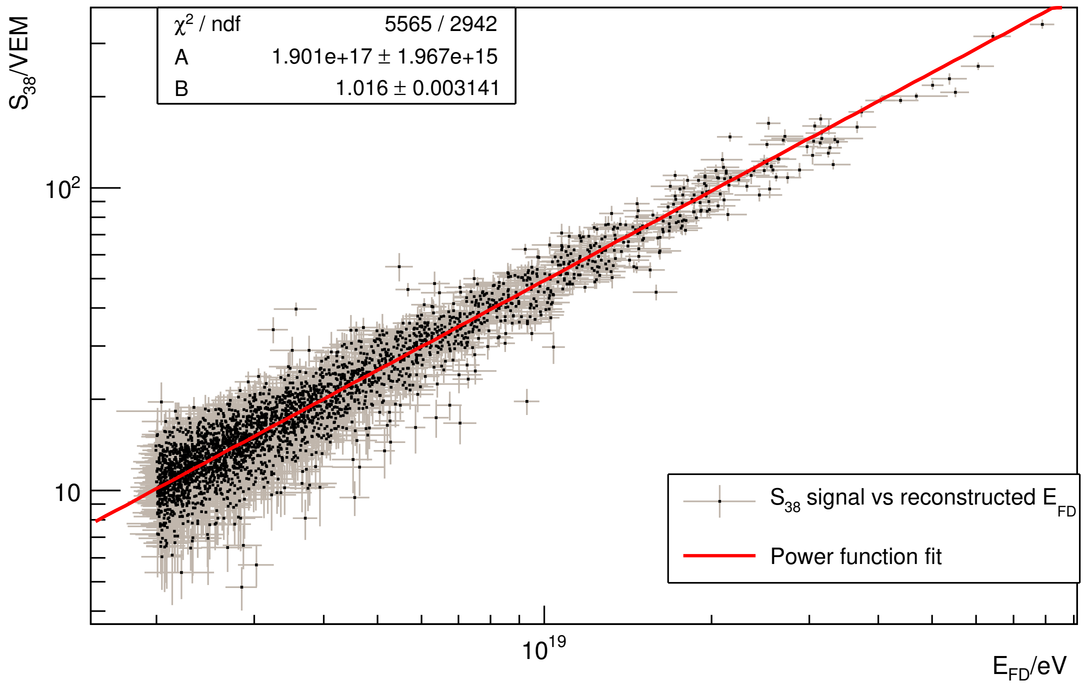

Figure 4.4: New calibration plot of S_{38} signal by reconstructed E_{FD} using $S(1000)$ DX method. The plot is fitted with a power law with the results displayed in the left box.

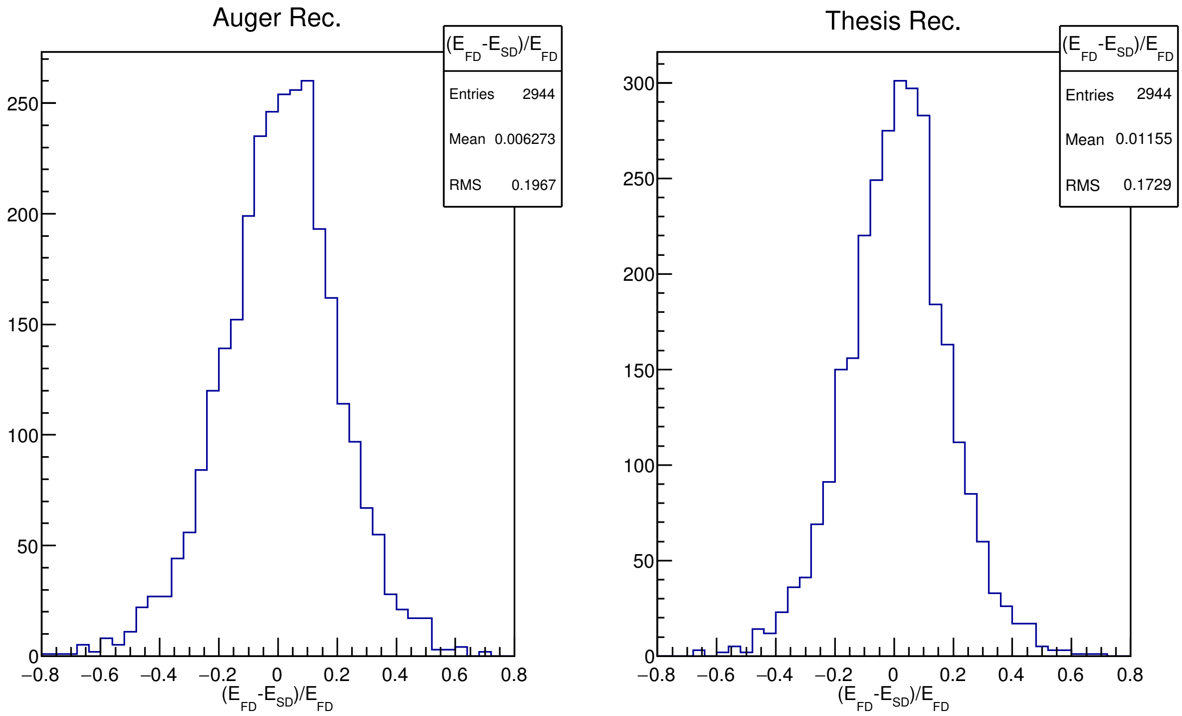

Figure 4.5: Histograms of relative difference between the shower total energy reconstructed by the fluorescence - E_{FD} - and surface detectors E_{SD} when applying the reconstruction method at the PAO (left) and the $S(1000)$ DX method (right).

Summary

The master's thesis was concerning about the Ultra-High Energy Cosmic Rays and their interaction in the Earth's atmosphere, resulting into the creation of Extensive Air Showers. Their composition, development and detection method at the Pierre Auger Observatory were also discussed. Main focus was dedicated on the estimation of the shower invisible energy carried away by muons and neutrinos that originated in a shower. A solid estimation of the shower invisible energy is needed for the successful shower reconstruction process at the PAO and thus a precise measurement of the UHECR energy spectrum.

Several methods for the invisible energy estimation using Monte Carlo simulations were investigated utilizing two newest hadronic models EPOS LHC and QGSJET-II-04. The average C_{miss} method parametrization of E_{inv} as a function of measured calorimetric energy E_{cal} was calculated and the universal parameters a, b and c were estimated as an even mixture of proton and iron-induced showers using cosmic-ray simulation code CONEX. The possible event-by-event correction utilizing the number of muons in a shower was also analyzed and tested on CONEX simulated data. The advantages of an event-by-event approach were pointed out.

As the next step, the possible relation between the invisible energy and the measurable SD signal $S(1000)$ was investigated for its possible application at the PAO using simulations by CORSIKA code. Three parametrizations of E_{inv} by $S(1000)$ with binning in the zenith angle θ or in the distance DX were found. The methods were compared using simulated data of reconstructed showers by Offline framework at the PAO. The best improvement in the reconstructed energy estimation was found for the $S(1000)$ DX method mainly in the energy range $10^{18} - 10^{18.5}$ eV.

The best method was applied to real cosmic-ray Golden data measured at the PAO. The invisible energy was estimated event-by-event for every shower using its measured parameters $S(1000)$, θ and X_{max} and parametrized as a power function of measured E_{cal}. The results were compared to energy reconstruction method as presented at the ICRC 2017 and the results of the thesis were found to predict slightly less amount of the E_{inv}/E_{REC} ratio by approximatively 1 % to 2 %.

Ultimately, method proposed in this thesis was compared to the standard shower energy reconstruction at the PAO by comparing the differences in the energy estimated by the FD and energy estimated by the SD while utilizing the modified SD signal calibration. A significant improvement in standard deviation by 2.38 % was achieved.

This indicates the usability of the proposed method of event-by-event correction to invisible energy in cosmic-ray showers.

If further elaborated, the $S(1000)\ DX$ method could eventually lower the systematic uncertainty of the reconstructed energy spectrum at the PAO which could ultimately improve our understanding of cosmic rays at the highest energies.

Appendix

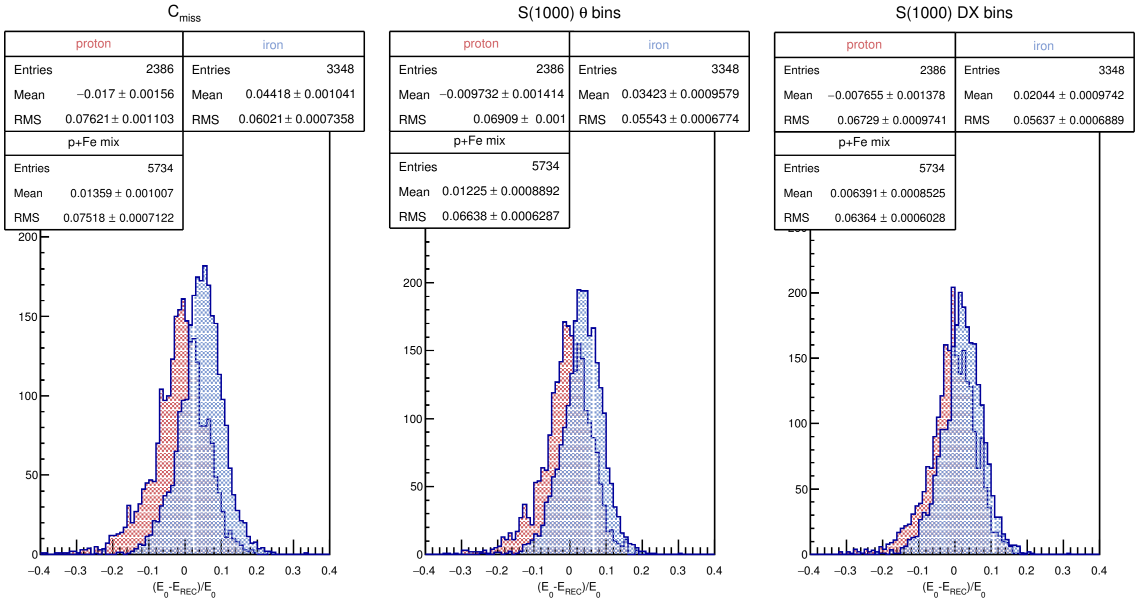

Figure 4.6: Histograms of relative reconstructed energy difference to the primary energy for three different methods used - C_{miss}, $S(1000)\ \theta$ and $S(1000)\ DX$ - for the primary energy range $10^{18} - 10^{18.5}$ eV. Both **EPOS LHC** and **QGSJET-II-04** model simulated showers are reconstructed. The histograms for iron-induced showers were scaled to have the same integral area as the proton-induced histograms.

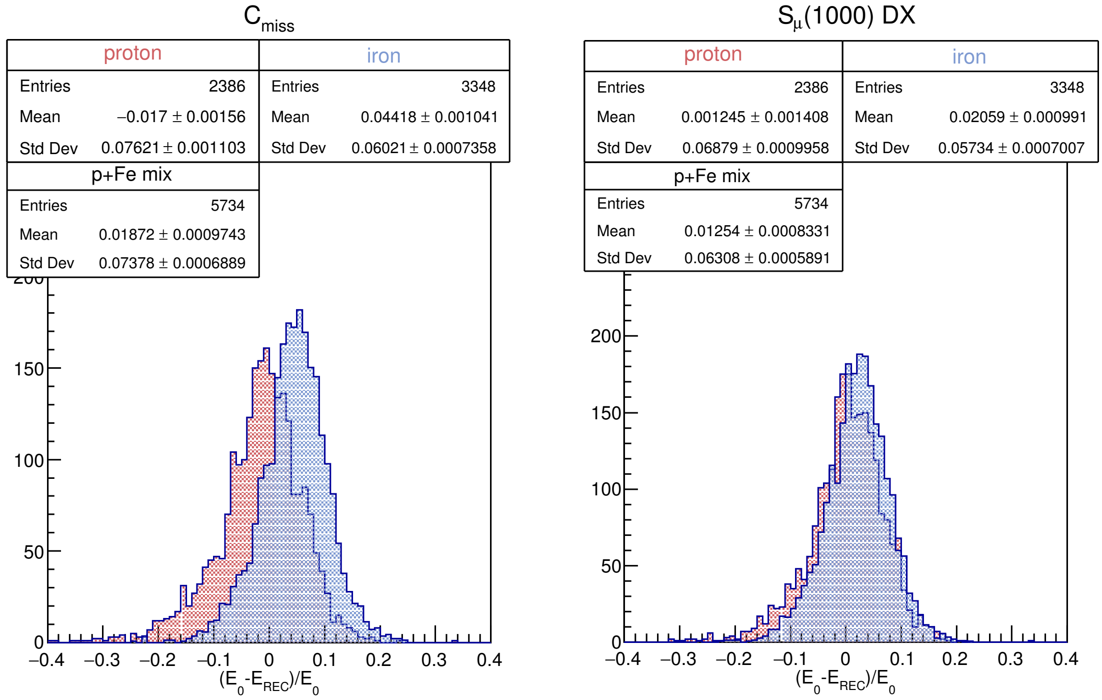

Figure 4.7: Histograms of relative reconstructed energy difference to the primary energy for two methods used - C_{miss} and $S_\mu(1000)\ DX$ - for the primary energy range $10^{18} - 10^{18.5}$ eV. Both **EPOS LHC** and **QGSJET-II-04** simulated showers are reconstructed. The histograms for iron-induced showers were scaled to have the same integral area as the proton-induced histograms.

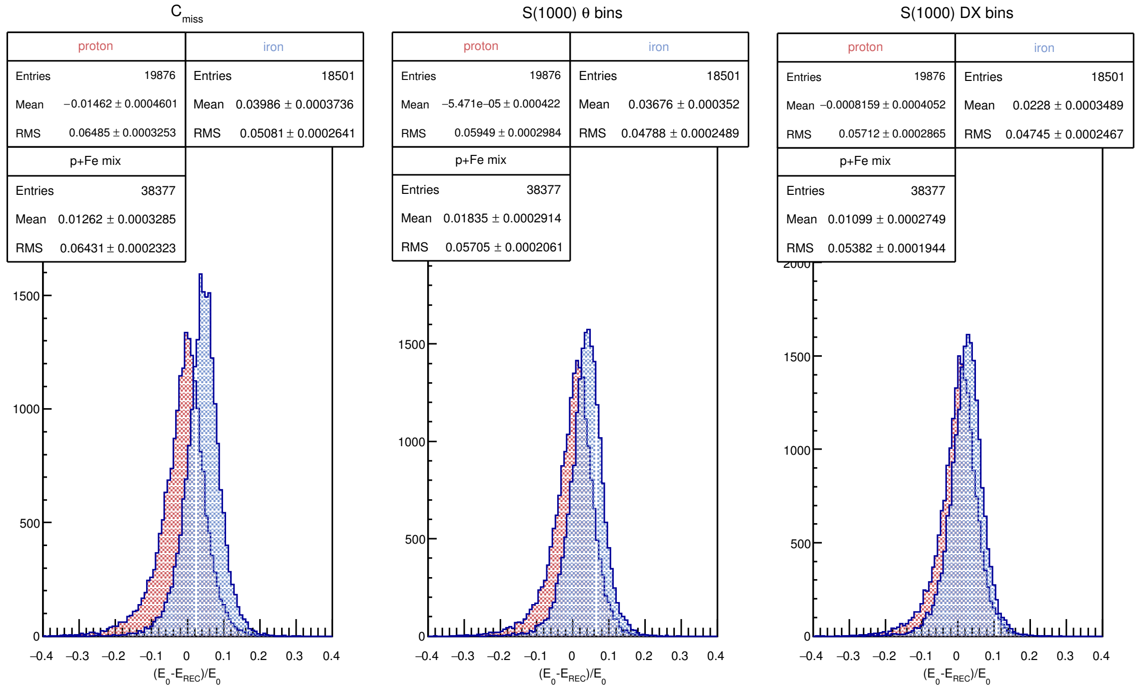

Figure 4.8: Histograms of relative reconstructed energy difference to the primary energy for three different methods used - C_{miss}, $S(1000)\ \theta$ and $S(1000)\ DX$ - for the primary energy range $10^{18.5} - 10^{19}$ eV. Both **EPOS LHC** and **QGSJET-II-04** model simulated showers are reconstructed. The histograms for iron-induced showers were scaled to have the same integral area as the proton-induced histograms.

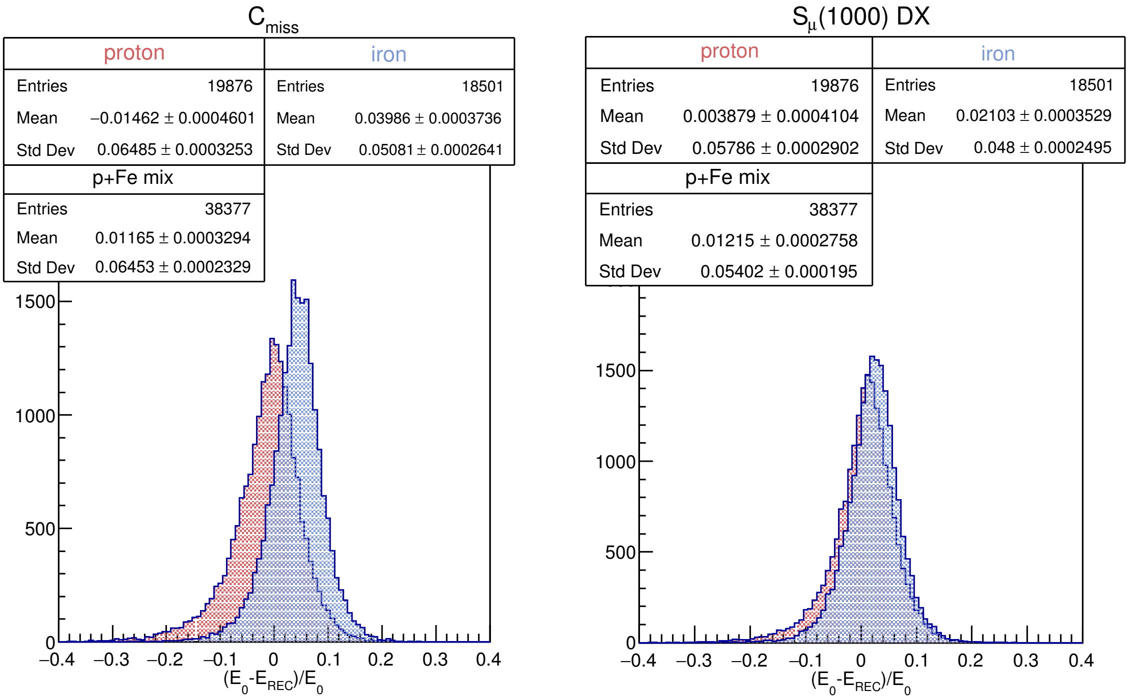

Figure 4.9: Histograms of relative reconstructed energy difference to the primary energy for two methods used - C_{miss} and $S_{\mu}(1000)\ DX$ - for the primary energy range $10^{18.5} - 10^{19}$ eV. Both **EPOS LHC** and **QGSJET-II-04** simulated showers are reconstructed. The histograms for iron-induced showers were scaled to have the same integral area as the proton-induced histograms.

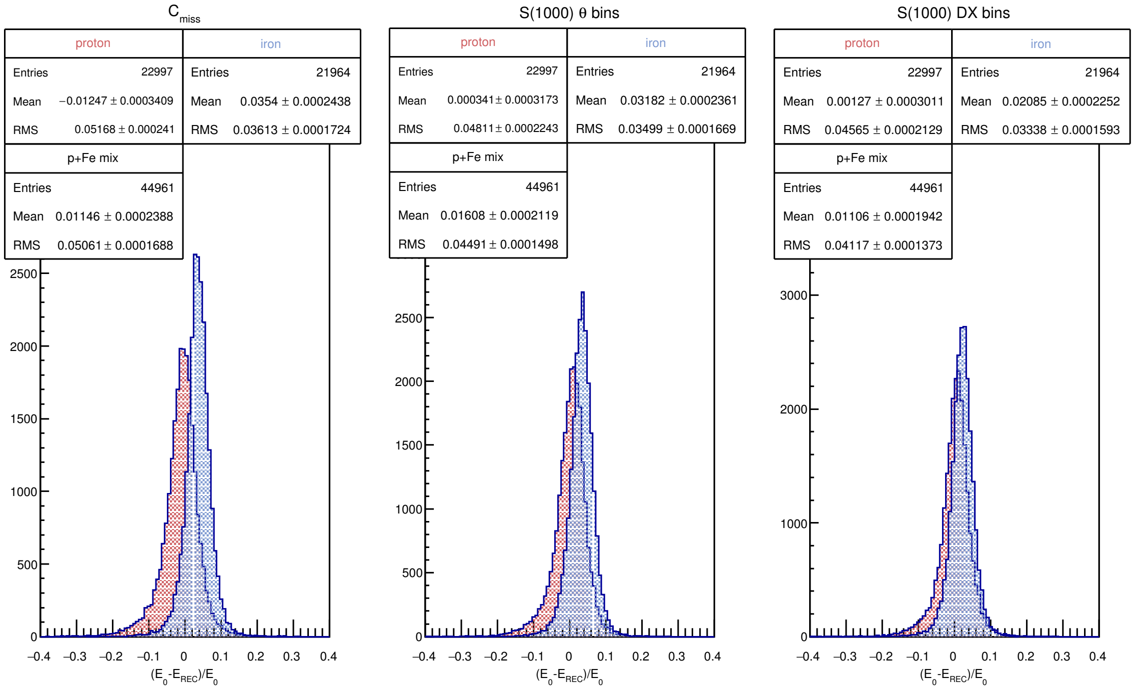

Figure 4.10: Histograms of relative reconstructed energy difference to the primary energy for three different methods used - C_{miss}, $S(1000)\ \theta$ and $S(1000)\ DX$ - for the primary energy range $10^{19} - 10^{19.5}$ eV. Both **EPOS LHC** and **QGSJET-II-04** model simulated showers are reconstructed. The histograms for iron-induced showers were scaled to have the same integral area as the proton-induced histograms.

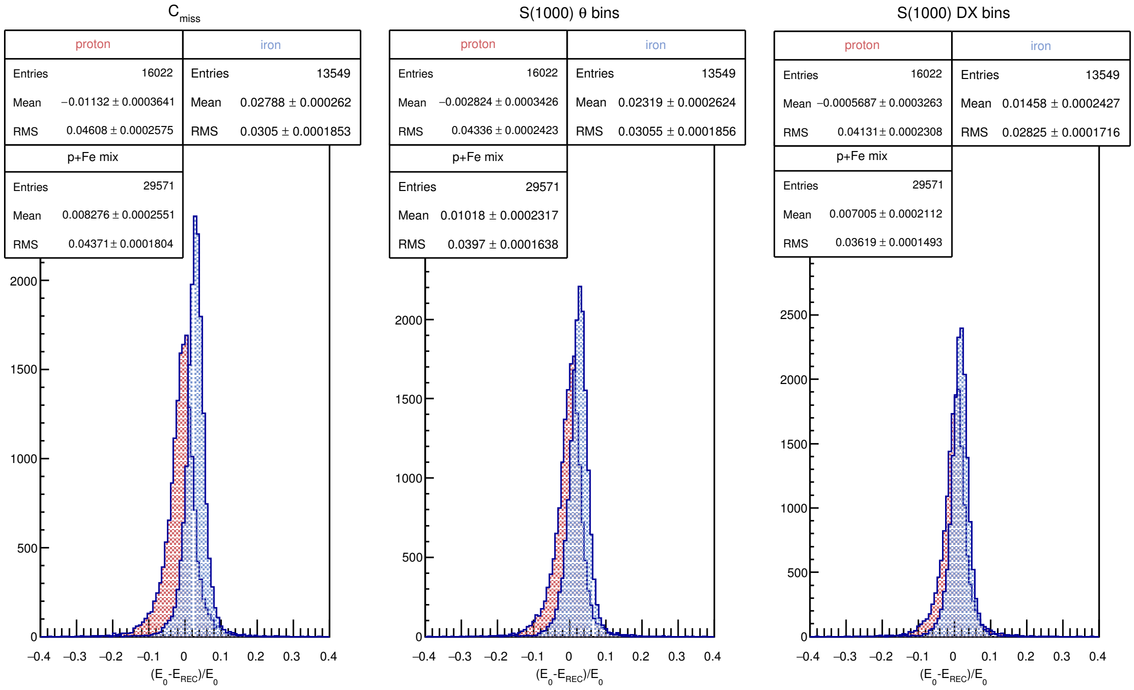

Figure 4.11: Histograms of relative reconstructed energy difference to the primary energy for three different methods used - C_{miss}, $S(1000)\ \theta$ and $S(1000)\ DX$ - for the primary energy range $10^{19.5} - 10^{20}$ eV. Both **EPOS LHC** and **QGSJET-II-04** model simulated showers are reconstructed. The histograms for iron-induced showers were scaled to have the same integral area as the proton-induced histograms.

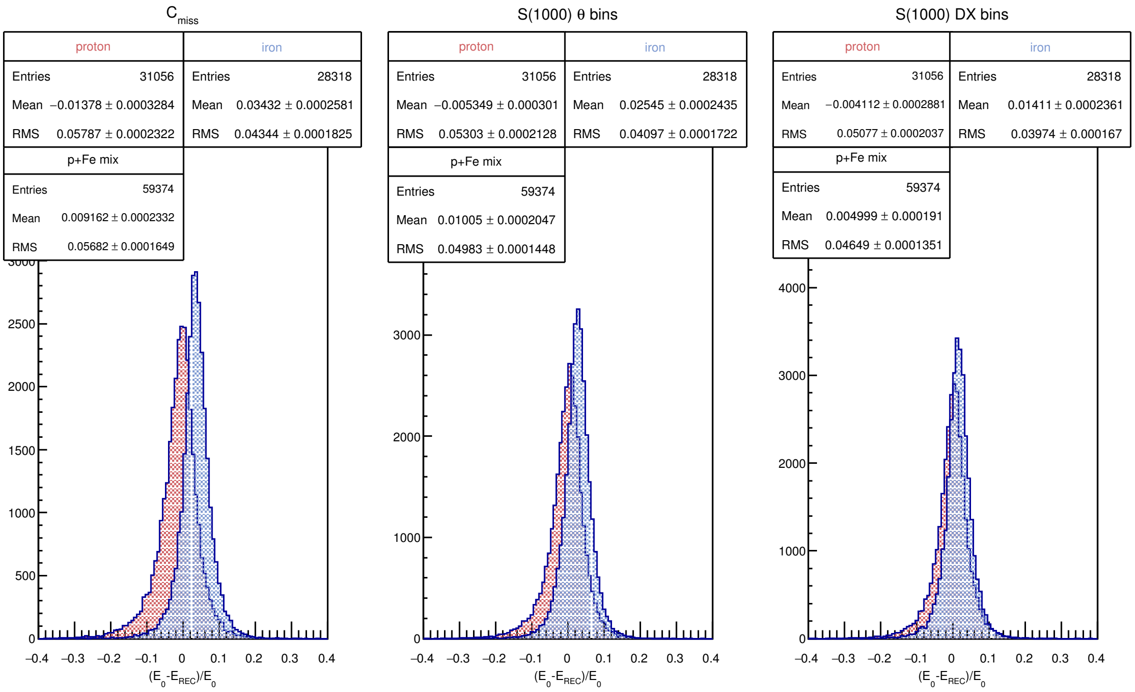

Figure 4.12: Histograms of relative reconstructed energy difference to the primary energy for three different methods used - C_{miss}, $S(1000)\ \theta$ and $S(1000)\ DX$ - for the primary energy range $10^{18} - 10^{20}$ eV. Only **EPOS LHC** model simulated showers are reconstructed. The histograms for iron-induced showers were scaled to have the same integral area as the proton-induced histograms.

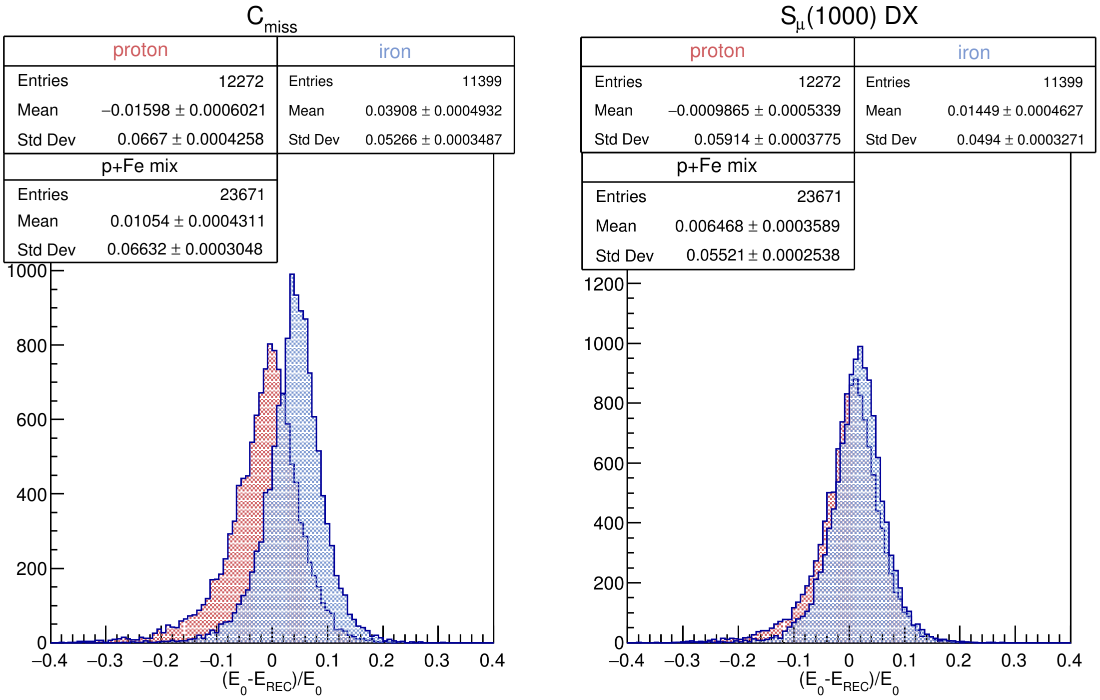

Figure 4.13: Histograms of relative reconstructed energy difference to the primary energy for two methods used - C_{miss} and $S_{\mu}(1000)\ DX$ - for the primary energy range $10^{18} - 10^{19}$ eV. Only **EPOS LHC** simulated showers are reconstructed. The histograms for iron-induced showers were scaled to have the same integral area as the proton-induced histograms.

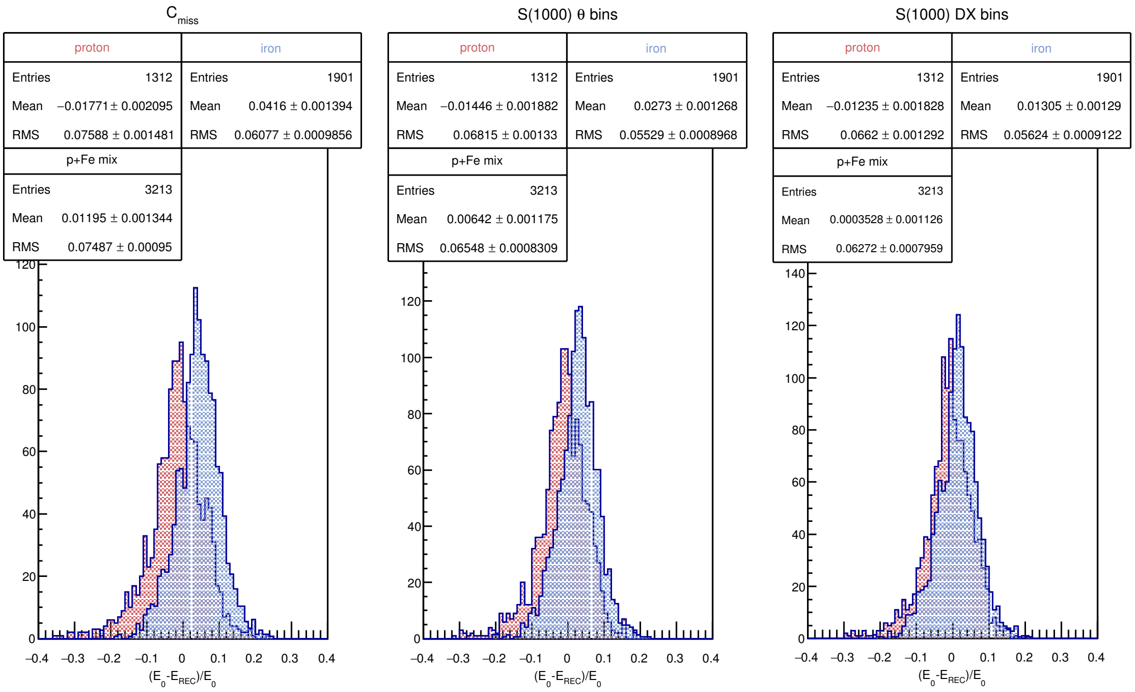

Figure 4.14: Histograms of relative reconstructed energy difference to the primary energy for three different methods used - C_{miss}, $S(1000)$ θ and $S(1000)$ DX - for the primary energy range $10^{18} - 10^{18.5}$ eV. Only **EPOS LHC** model simulated showers are reconstructed. The histograms for iron-induced showers were scaled to have the same integral area as the proton-induced histograms.

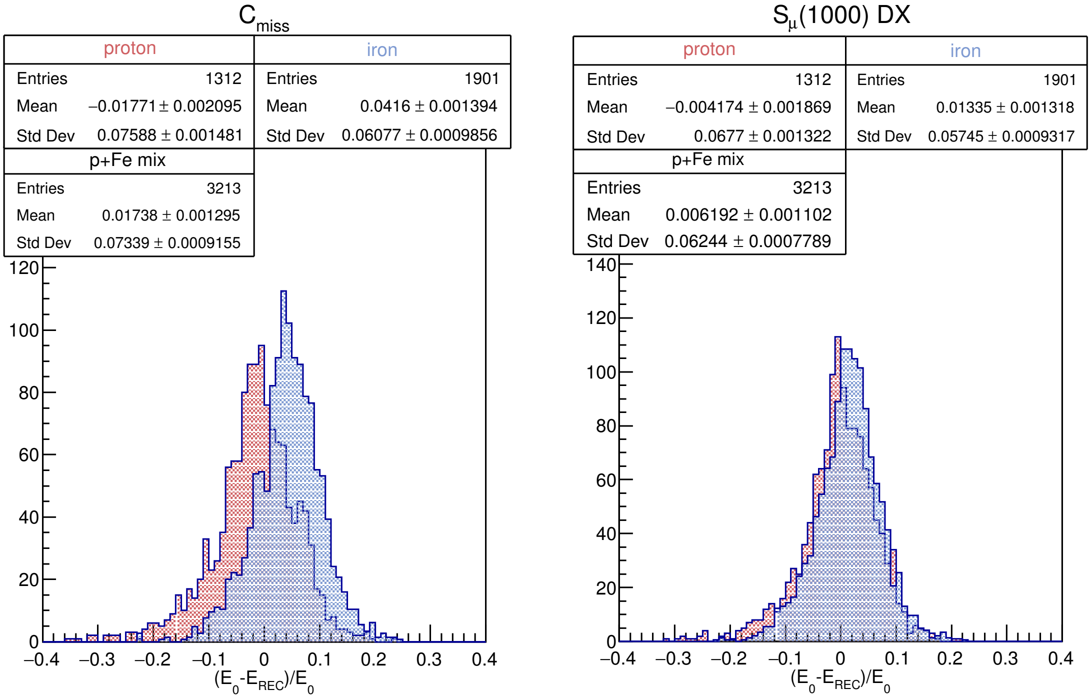

Figure 4.15: Histograms of relative reconstructed energy difference to the primary energy for two methods used - C_{miss} and $S_\mu(1000)$ DX - for the primary energy range $10^{18} - 10^{18.5}$ eV. Only **EPOS LHC** simulated showers are reconstructed. The histograms for iron-induced showers were scaled to have the same integral area as the proton-induced histograms.

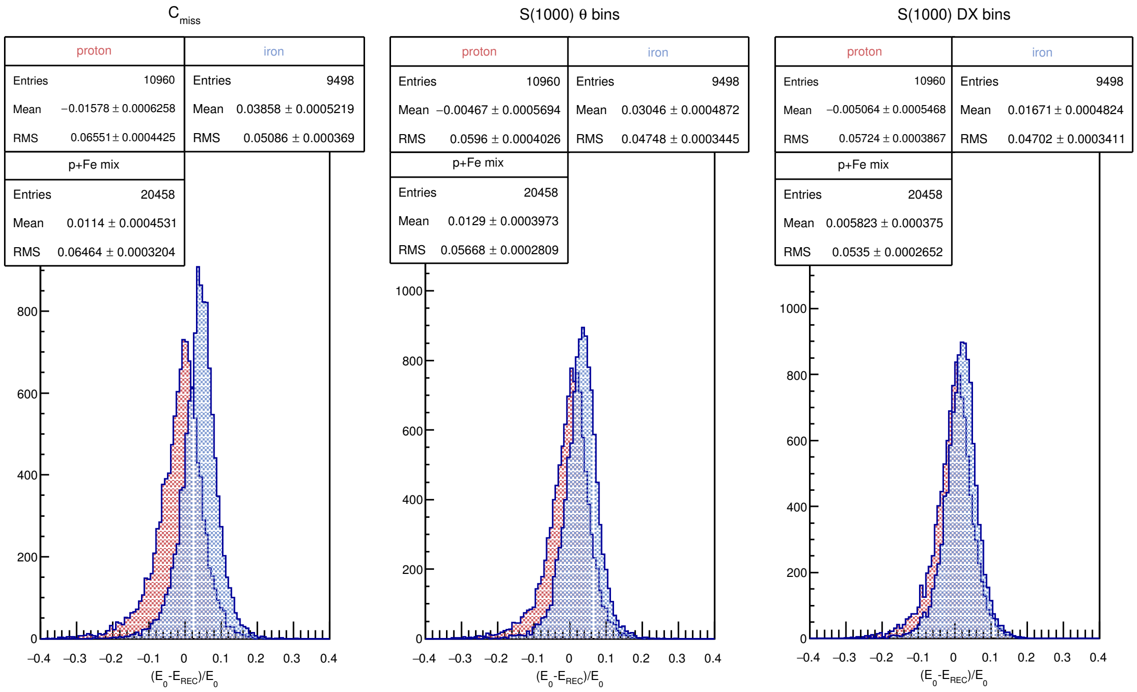

Figure 4.16: Histograms of relative reconstructed energy difference to the primary energy for three different methods used - C_{miss}, $S(1000)\ \theta$ and $S(1000)\ DX$ - for the primary energy range $10^{18.5} - 10^{19}$ eV. Only **EPOS LHC** model simulated showers are reconstructed. The histograms for iron-induced showers were scaled to have the same integral area as the proton-induced histograms.

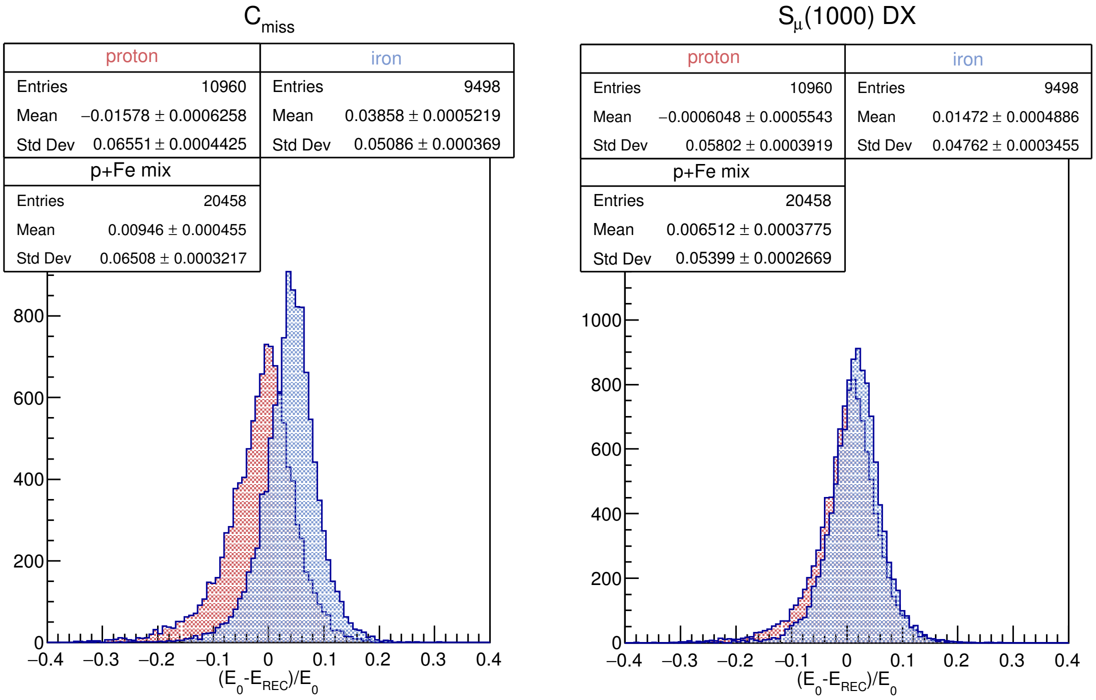

Figure 4.17: Histograms of relative reconstructed energy difference to the primary energy for two methods used - C_{miss} and $S_\mu(1000)\ DX$ - for the primary energy range $10^{18.5} - 10^{19}$ eV. Only **EPOS LHC** simulated showers are reconstructed. The histograms for iron-induced showers were scaled to have the same integral area as the proton-induced histograms.

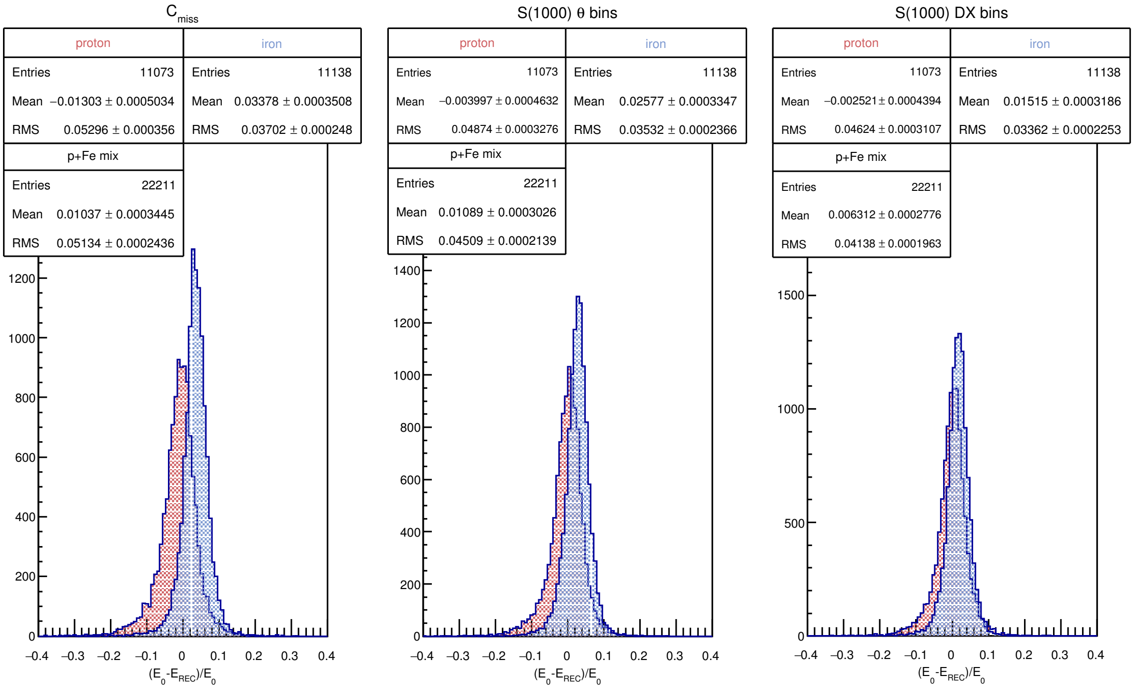

Figure 4.18: Histograms of relative reconstructed energy difference to the primary energy for three different methods used - C_{miss}, $S(1000)\ \theta$ and $S(1000)\ DX$ - for the primary energy range $10^{19} - 10^{19.5}$ eV. Only **EPOS LHC** model simulated showers are reconstructed. The histograms for iron-induced showers were scaled to have the same integral area as the proton-induced histograms.

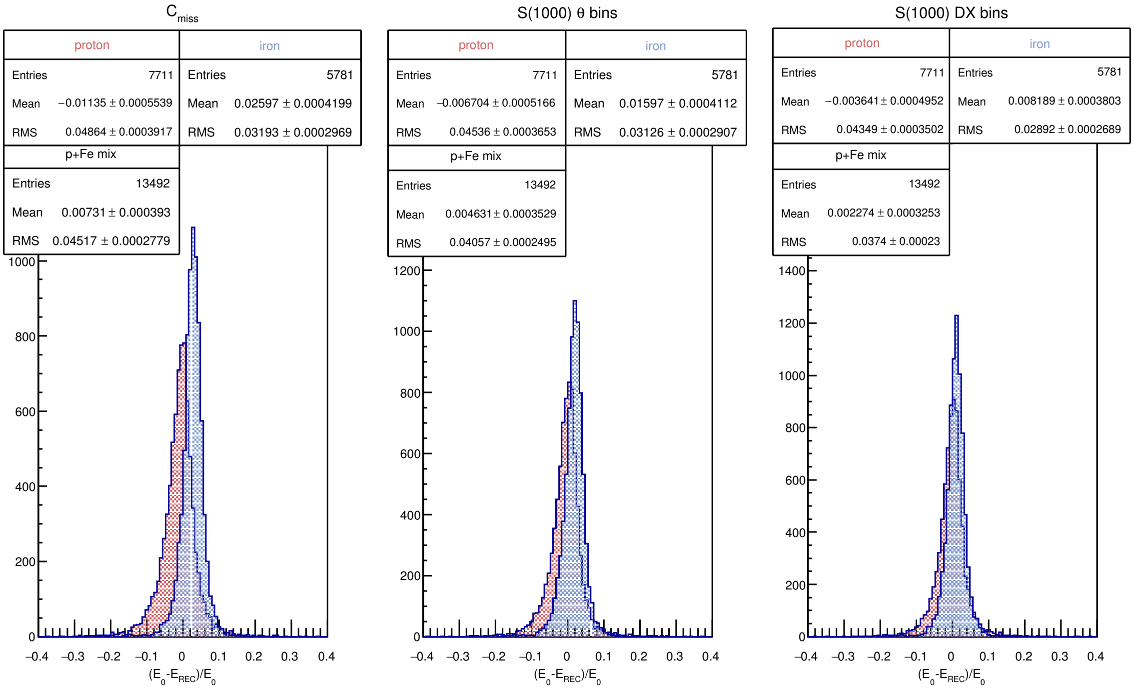

Figure 4.19: Histograms of relative reconstructed energy difference to the primary energy for three different methods used - C_{miss}, $S(1000)\ \theta$ and $S(1000)\ DX$ - for the primary energy range $10^{19.5} - 10^{20}$ eV. Only **EPOS LHC** model simulated showers are reconstructed. The histograms for iron-induced showers were scaled to have the same integral area as the proton-induced histograms.

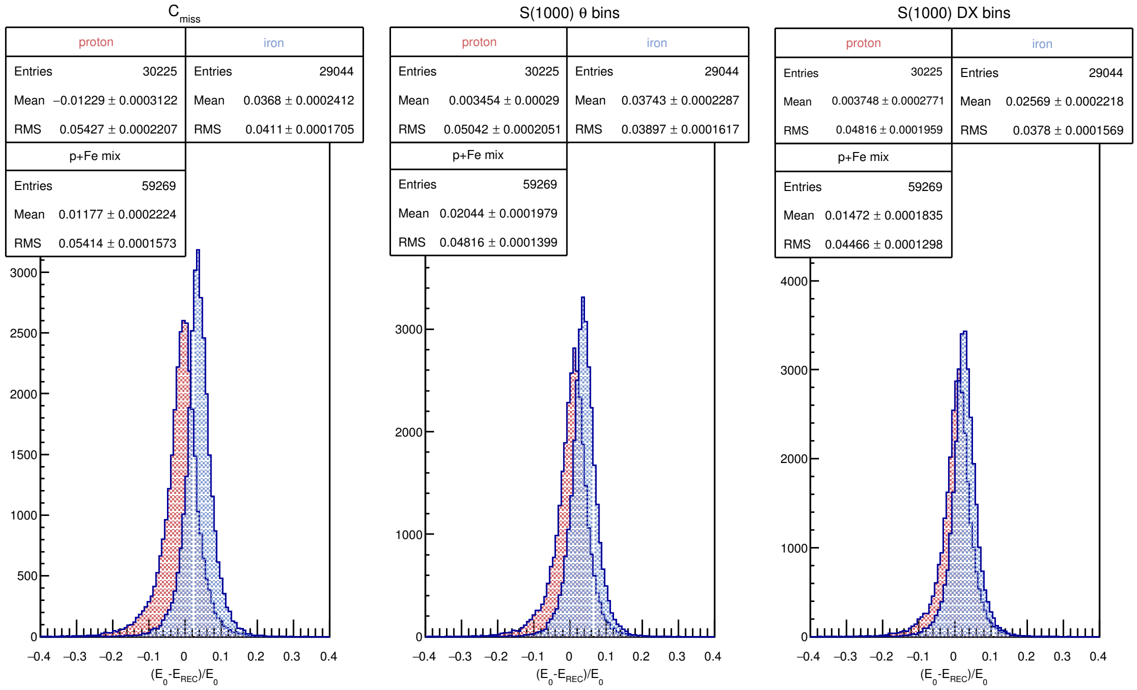

Figure 4.20: Histograms of relative reconstructed energy difference to the primary energy for three different methods used - C_{miss}, $S(1000)\ \theta$ and $S(1000)\ DX$ - for the primary energy range $10^{18} - 10^{20}$ eV. Only **QGSJET-II-04** model simulated showers are reconstructed. The histograms for iron-induced showers were scaled to have the same integral area as the proton-induced histograms.

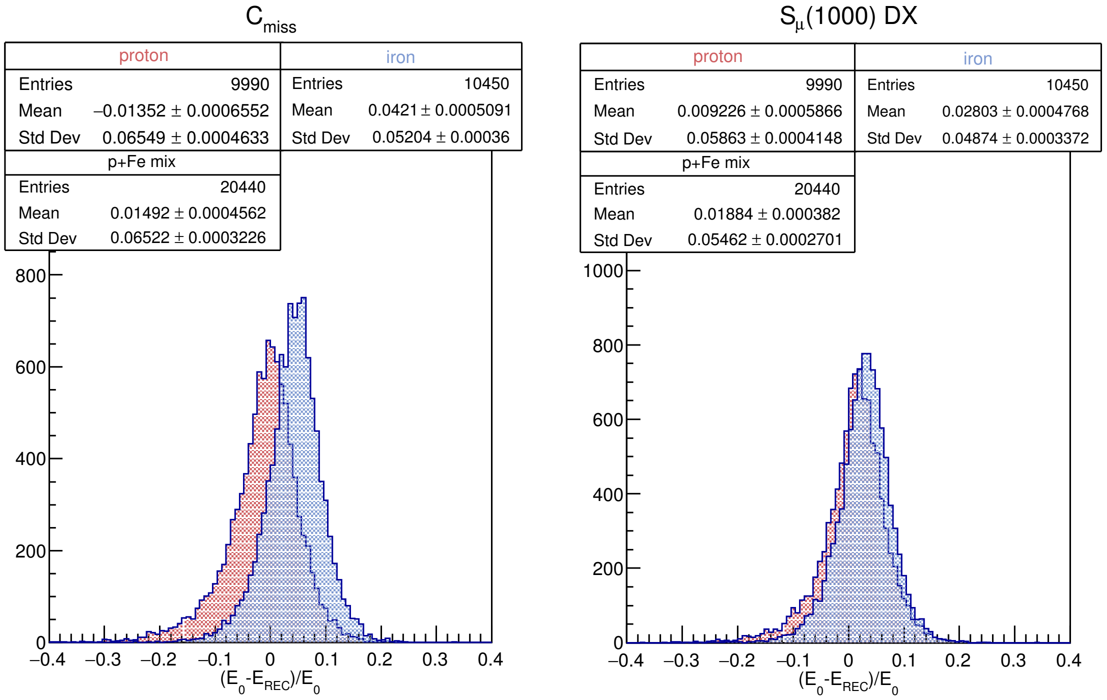

Figure 4.21: Histograms of relative reconstructed energy difference to the primary energy for two methods used - C_{miss} and $S_{\mu}(1000)\ DX$ - for the primary energy range $10^{18} - 10^{19}$ eV. Only **QGSJET-II-04** simulated showers are reconstructed. The histograms for iron-induced showers were scaled to have the same integral area as the proton-induced histograms.

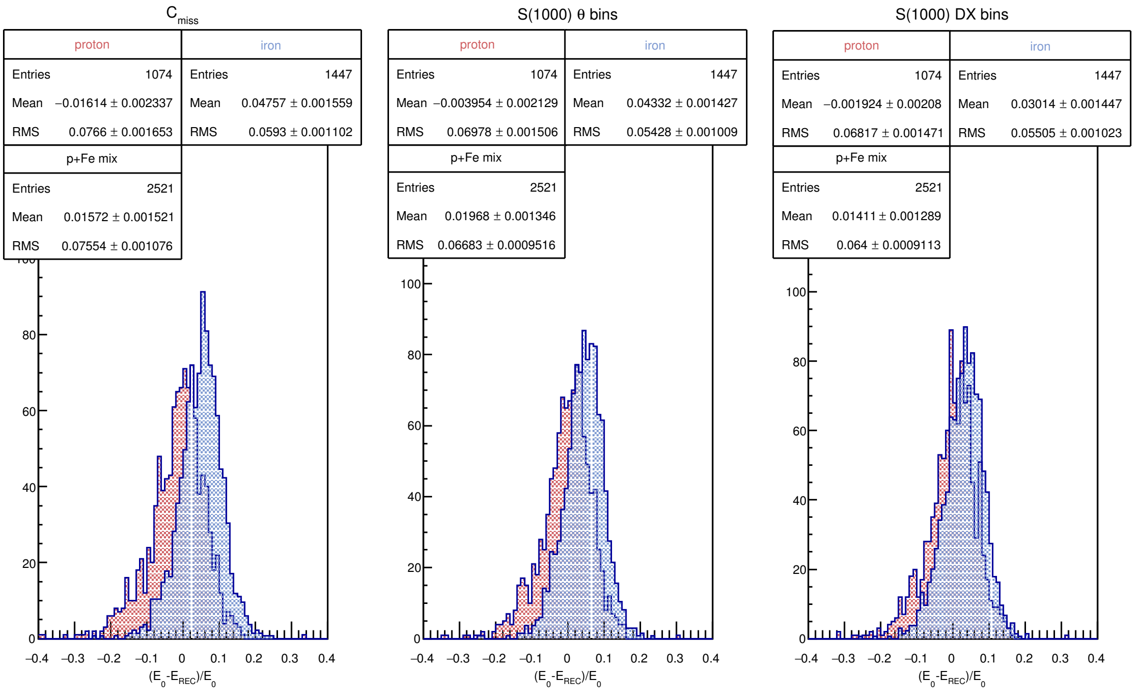

Figure 4.22: Histograms of relative reconstructed energy difference to the primary energy for three different methods used - C_{miss}, $S(1000)\ \theta$ and $S(1000)\ DX$ - for the primary energy range $10^{18} - 10^{18.5}$ eV. Only **QGSJET-II-04** model simulated showers are reconstructed. The histograms for iron-induced showers were scaled to have the same integral area as the proton-induced histograms.

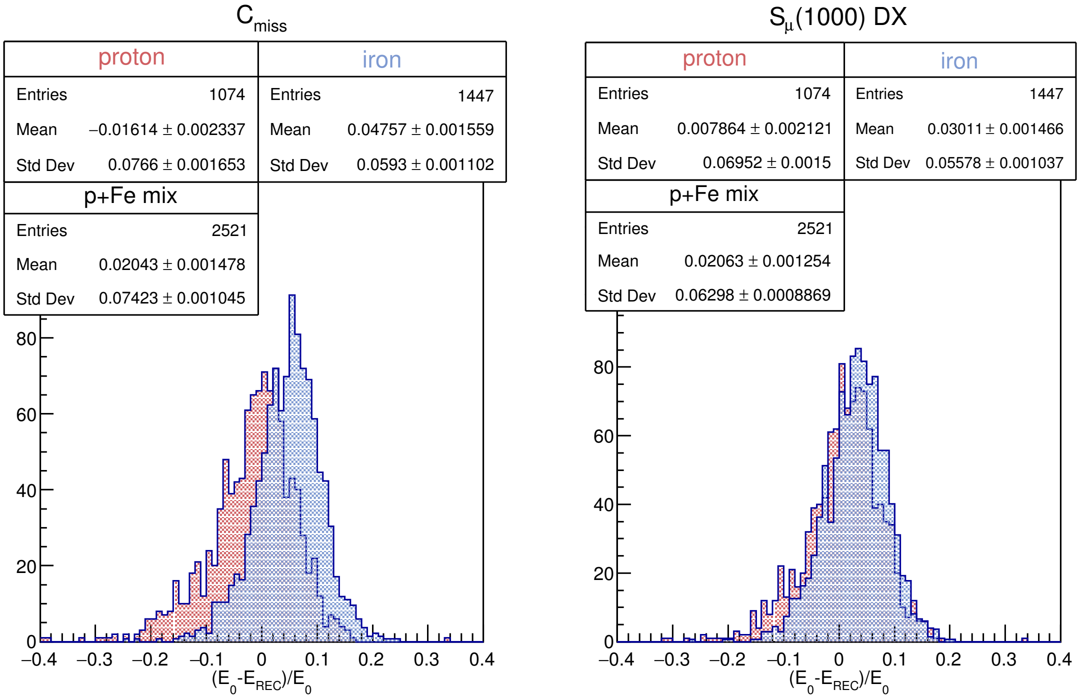

Figure 4.23: Histograms of relative reconstructed energy difference to the primary energy for two methods used - C_{miss} and $S_{\mu}(1000)\ DX$ - for the primary energy range $10^{18} - 10^{18.5}$ eV. Only **QGSJET-II-04** simulated showers are reconstructed. The histograms for iron-induced showers were scaled to have the same integral area as the proton-induced histograms.

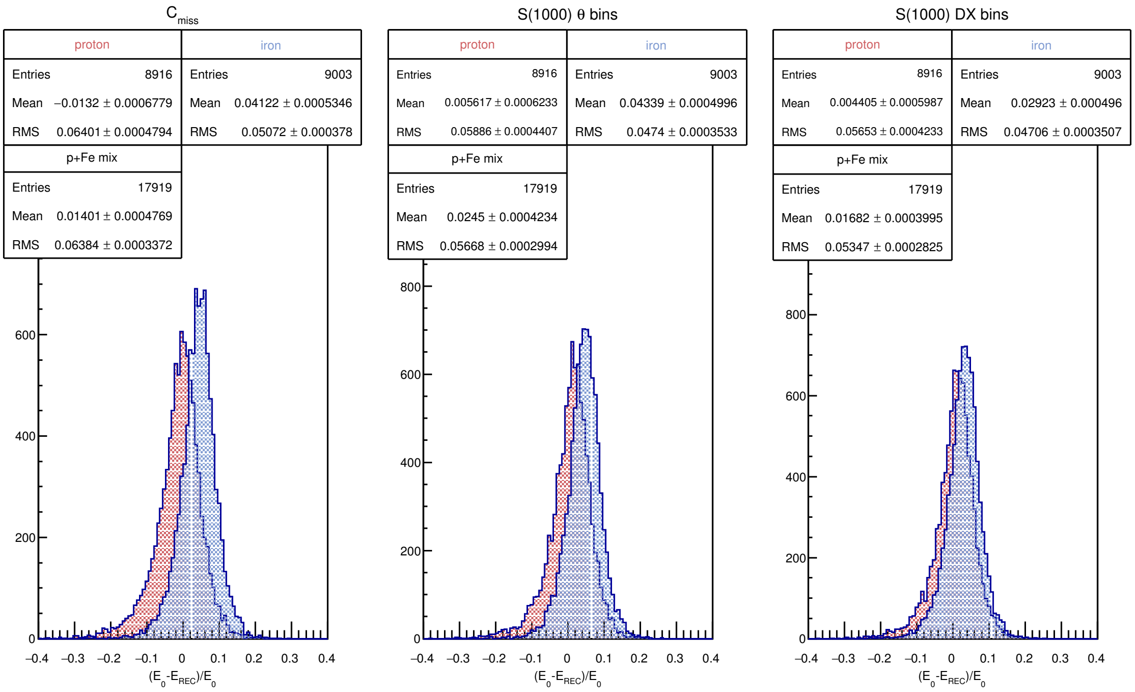

Figure 4.24: Histograms of relative reconstructed energy difference to the primary energy for three different methods used - C_{miss}, $S(1000)\ \theta$ and $S(1000)\ DX$ - for the primary energy range $10^{18.5} - 10^{19}$ eV. Only **QGSJET-II-04** model simulated showers are reconstructed. The histograms for iron-induced showers were scaled to have the same integral area as the proton-induced histograms.

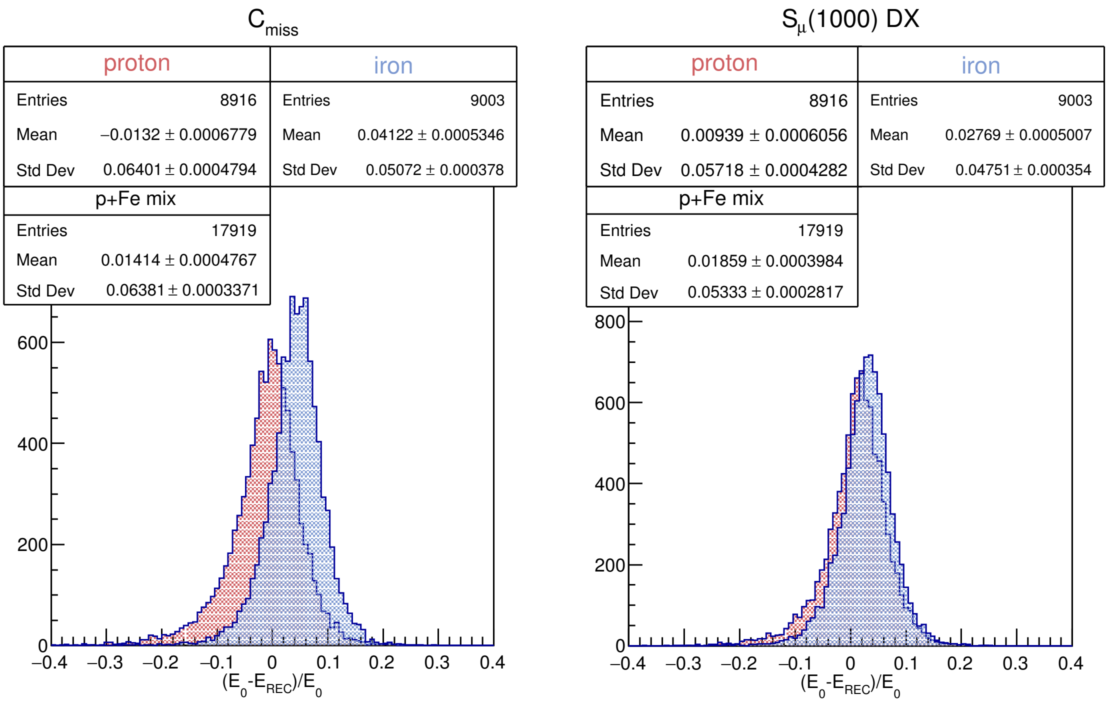

Figure 4.25: Histograms of relative reconstructed energy difference to the primary energy for two methods used - C_{miss} and $S_{\mu}(1000)\ DX$ - for the primary energy range $10^{18.5} - 10^{19}$ eV. Only **QGSJET-II-04** simulated showers are reconstructed. The histograms for iron-induced showers were scaled to have the same integral area as the proton-induced histograms.

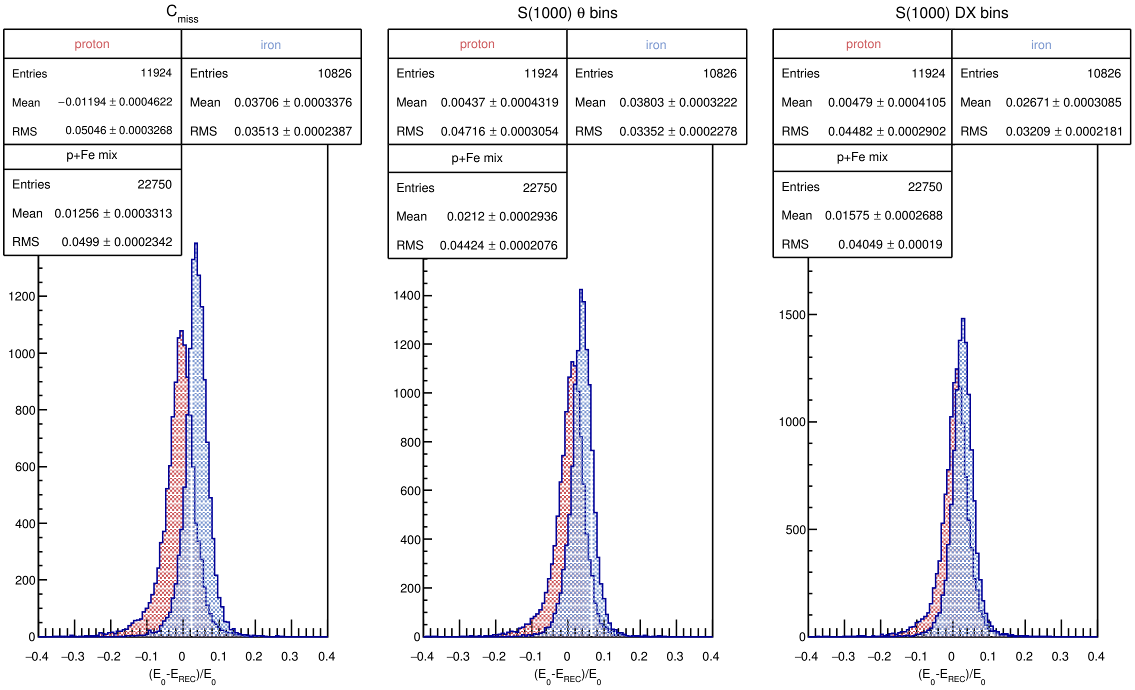

Figure 4.26: Histograms of relative reconstructed energy difference to the primary energy for three different methods used - C_{miss}, $S(1000)$ θ and $S(1000)$ DX - for the primary energy range $10^{19} - 10^{19.5}$ eV. Only **QGSJET-II-04** model simulated showers are reconstructed. The histograms for iron-induced showers were scaled to have the same integral area as the proton-induced histograms.

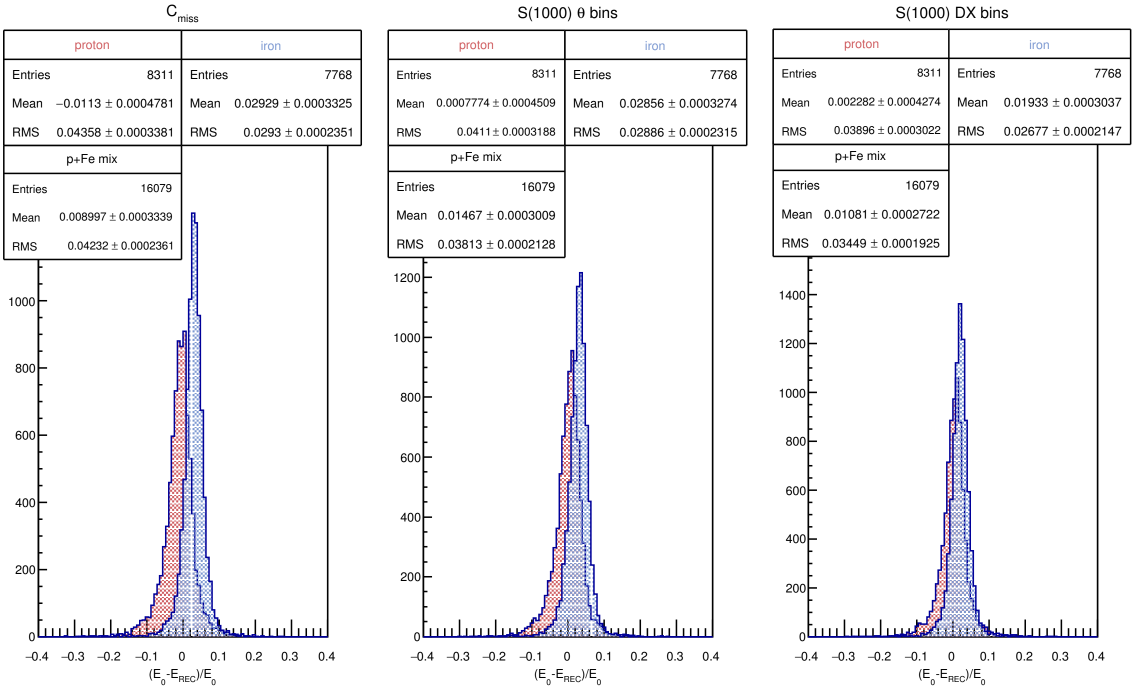

Figure 4.27: Histograms of relative reconstructed energy difference to the primary energy for three different methods used - C_{miss}, $S(1000)$ θ and $S(1000)$ DX - for the primary energy range $10^{19.5} - 10^{20}$ eV. Only **QGSJET-II-04** model simulated showers are reconstructed. The histograms for iron-induced showers were scaled to have the same integral area as the proton-induced histograms.

Bibliography

[1] Aab, A., et al. The Pierre Auger Observatory: Contributions to the 33rd International Cosmic Ray Conference (ICRC 2013). In *Proceedings, 33rd International Cosmic Ray Conference (ICRC2013): Rio de Janeiro, Brazil, July 2-9, 2013*.

[2] Aab, A., et al. The Pierre Auger Observatory: Contributions to the 35th International Cosmic Ray Conference (ICRC 2017). In *Proceedings, 35th International Cosmic Ray Conference (ICRC 2017): Bexco, Busan, Korea, July 12-20, 2017*.

[3] Aab, A., et al. The rapid atmospheric monitoring system of the Pierre Auger Observatory. *J. Instrum 7*, 09 (2012), P09001.

[4] Aab, A., et al. Depth of maximum of air-shower profiles at the Pierre Auger Observatory. I. Measurements at energies above $10^{17.8}$eV. *Phys. Rev. D90*, 12 (2014), 122005.

[5] Aab, A., et al. Searches for Anisotropies in the Arrival Directions of the Highest Energy Cosmic Rays Detected by the Pierre Auger Observatory. *Astrophys. J. 804*, 1 (2015), 15.

[6] Aab, A., et al. The Pierre Auger Cosmic Ray Observatory. *Nucl. Instrum. Meth. A798* (2015), 172–213.

[7] Aab, A., et al. The Pierre Auger Observatory Upgrade - Preliminary Design Report, 2016, available at: *https://arxiv.org/abs/1604.03637*.

[8] Aab, A., et al. Observation of a large-scale anisotropy in the arrival directions of cosmic rays above 8.10^{18} ev. *Science 357*, 6357 (2017), 1266–1270.

[9] Abraham, J., et al. Properties and performance of the prototype instrument for the Pierre Auger Observatory. *Nucl. Instrum. Meth. A523* (2004), 50–95.

[10] Abraham, J., et al. The Fluorescence Detector of the Pierre Auger Observatory. *Nucl. Instrum. Meth. A620* (2010), 227–251.

[11] Argiro, S., Barroso, S. L. C., Gonzalez, J., Nellen, L., Paul, T. C., Porter, T. A., Prado, Jr., L., Roth, M., Ulrich, R., and Veberic, D. The Offline Software Framework of the Pierre Auger Observatory. *Nucl. Instrum. Meth. A580* (2007), 1485–1496.

[12] Barbosa, H. M. J., Catalani, F., Chinellato, J. A., and Dobrigkeit, C. Determination of the calorimetric energy in extensive air showers. *Astropart. Phys. 22* (2004), 159–166.

[13] Bergmann, T., et al. One-dimensional hybrid approach to extensive air shower simulation. *Astropart. Phys. 26* (2007), 420–432.

[14] Blandford, R., and Ostriker, J. Particle acceleration by astrophysical shocks. *Astrophy. J. 221* (1978), 29–32.

[15] Engel, R., Heck, D., and Pierog, T. Extensive air showers and hadronic interactions at high energy. *Ann. Rev. Nucl. Part. Sci. 61* (2011), 467–489.

[16] Greisen, K. End to the cosmic-ray spectrum? *Phys. Rev. Lett. 16* (1966), 748–750.

[17] Grupen, C. *Astroparticle physics.* Springer Science & Business Media, 2005, ISBN 978-3-540-25312-9.

[18] Heck, D., Schatz, G., Thouw, T., Knapp, J., and Capdevielle, J. N. CORSIKA: A Monte Carlo code to simulate extensive air showers.

[19] Hersil, J., Escobar, I., Scott, D., Clark, G., and Olbert, S. Observations of Extensive Air Showers near the Maximum of Their Longitudinal Development. *Phys. Rev. Lett. 6* (1961), 22–23.

[20] Hillas, A. Cosmic rays in an evolving universe. *Can. J. Phy. 46*, 10 (1968), 623–626.

[21] Lagutin, A. A., Raikin, R. I., and Serebryakova, T. L. Air shower universality from 10^{14} to 10^{22} eV. *J. Phys. Conf. Ser. 409* (2013), 012092.

[22] Lipari, P. Universality of cosmic ray shower development. *Nuclear Physics B - Proceedings Supplements 196* (2009), 309 – 318.

[23] Mariazzi, A. G., Tueros, M. J., Rodriguez Fernandez, G., I., V., and Verzi, V. Comparison between the estimations of the invisible energy obtained in vertical and inclined showers. *GAP notes* (2018).

[24] Matthews, J. A Heitler model of extensive air showers. *Astropart. Phys. 22* (2005), 387–397.

[25] Nyklíček, M., and Trávníček, P. On the size of missing energy of cosmic ray showers. *Proceedings of the 31st ICRC Lodz 0240* (2010).

[26] Nyklíček, M., Řídký, J., and Trávníček, P. Influence of hadronic interaction models on determination of chemical composition and size of the missing energy. *GAP notes* (2008).

[27] Ostapchenko, S. Status of QGSJET. *AIP Conf. Proc. 928* (2007), 118–125.

[28] Perkins, D. *Particle astrophysics.* Oxford University Press, USA, 2003.

[29] Pierog, T. Connecting accelerator experiments and cosmic ray showers. *EPJ Web of Conferences 53* (2013), 01004.

[30] Werner, K. The hadronic interaction model epos. *Nuclear Physics B - Proceedings Supplements 175-176* (2008), 81 – 87.

[31] Zatsepin, G. T., and Kuzmin, V. A. Upper limit of the spectrum of cosmic rays. *JETP Lett. 4* (1966), 78–80.